Report No. 75
COO-2456-57
UC-20,G

Columbia University
in the City of New York

NUMERICAL SIMULATION STUDIES OF TOROIDAL PINCHES

by

Wonchull Park

1978

Work Supported by DOE Contract EY-76-S-02-2456

Plasma Laboratory

School of Engineering and Applied Science

Columbia University

New York, N.Y. 10027

DISCLAIMER

Report No. 75
COO-2456-57
UC-20,G

NUMERICAL SIMULATION STUDIES OF TOROIDAL PINCHES

by

Wonchull Park

1978

Work Supported by DOE Contract EY-76-S-02-2456

Plasma Laboratory

School of Engineering and Applied Science

Columbia University

New York, N.Y. 10027

ABSTRACT

A time dependent two-dimensional MHD calculation for pinch experiments, previously developed at Columbia[1], is improved and modified so that very long calculations (until the plasma reaches a quasi-equilibrium state) are possible. The calculation method is presented, and the simulation results of the Jutphaas screw pinch SP-1 and the Los Alamos reverse-field pinches ZT-I, ZT-S and ZT-40 are studied.

A set of single fluid resistive MHD equations are solved using standard alternate direction implicit method in an Eulerian difference scheme. Initial conditions correspond to the start of the main discharge in the experiment, with a homogeneous fully ionized plasma at rest. The equations are driven by time dependent boundary conditions : the toroidal magnetic field and the poloidal flux at the wall. The poloidal flux is indirectly extrapolated from the prescribed total toroidal plasma current. Most of other boundary values both at the wall and at the coordinate origin are obtained from the conservation laws.

The anomality of the electric resistivity is studied by comparing the experimental results with the calculated results of different resistivity coefficients. The initial setting up phase of ZT-I and ZT-S are well simulated using a semi-empirical anomalous resistivity algorithm due to R. Chodura. In the later quasi-equilibrium phase however,

the resistivity appears to be classical.

The toroidal curvature effects are automatically obtained in this two-dimensional calculation. The calculation shows a strong toroidal plasma flow with an antisymmetric toroidal velocity profile against the midplane of the torus. In the later phase, this toroidal flow is balanced and sustained by the azimuthal asymmetry of the dissipative effects due to toroidal curvature, thus resulting in a steady-state quasi-equilibrium. The physical origin and the consequences of this toroidal flow are discussed (e.g., the toroidal shift of the magnetic axis is nearly doubled due to this flow).

A simulation predicting ZT-40 behavior is presented. The basic differences of ZT-40 from smaller ZT-I and ZT-S are discussed from both physical and numerical view points. The scaling law of the dissipative MHD equations is derived. The important time scales, i.e., Alfven, field diffusion, thermal diffusion, viscous dissipation and numerical viscous dissipation time scales, are studied.

The overall good agreement between experiment and calculation presented assures that the plasma model used (i.e., single fluid dissipative MHD) gives a good representation of the physical phenomena, at least in the parameter regime of the smaller experiments SP-1, ZT-I and ZT-S.

ACKNOWLEDGEMENTS

It is a pleasure to thank my advisor Professor C. K. Chu, who kindly gave unconditional support throughout, morally as well as academically.

I would also like to thank Professor R. A. Gross and Dr. D. A. Baker for their guidance and encouragement.

I am also indebted to Dr. H. C. Lui who wrote the original version of the code and also provided considerable help during this work.

Thanks to Ahmed Aydemir, George Georgeou, Morteza Ghassemi, Cristine Kostek, Nazie Sharky and other fellow graduate students for the stimulating discussions and friendship.

I would like to thank Dana Gudan and Theodora Ziongas who typed the difficult manuscript and other staff members of the department for their help during this work.

A special thanks to my brother, Won Junn, for his moral support and encouragement.

This work is dedicated to my parents.

The present work was supported by the United States Department of Energy under contract EY-76-S-02-2456.

TABLE OF CONTENTS

		Page
Abstract		i
Acknowledgements		iii
I.	INTRODUCTION	1
II.	FORMULATION OF THE PROBLEM	8
	2.1 Derivation of the Basic Equations	9
	2.2 A Remark on the Toroidal Symmetry	14
	2.3 Transport Coefficients	16
	2.4 Initial Conditions	21
III.	NUMERICAL SOLUTION PROCEDURES	22
	3.1 Basic Numerical Procedure	22
	3.2 Boundary Conditions	26
	3.2.A Interpretation of the Basic Difference Scheme and the Boundary Conditions	27
	3.2.B Boundary Conditions at the Wall	33
	3.2.C Flux in the Hole of the Torus and the Total Toroidal Plasma Current	35
	3.2.D Boundary Conditions for the θ Direction	39
	3.2.E Treatment of the Coordinate Origin	42
	3.3 Treatment of the Low Density Region	49

IV. RESULTS 54

4.1 SP-1 Screw Pinch 56

4.2 ZT-I Reverse-Field Pinch 72

4.3 ZT-S Reverse-Field Pinch 81

4.3.A General Behavior of the Plasma 81

4.3.B Toroidal Curvature Effects 92

4.4 ZT-40 Reverse-Field Pinch 102

4.4.A Scaling of the Equations 102

4.4.B Simulation Results 106

4.4.C Confinement Characteristics 114

REFERENCES 117

APPENDIX : Computer Program Listing 120

I. INTRODUCTION

It is well known that the efficiency of a magnetic fusion reactor will largely depend on the plasma β, since fusion power density goes as β^2. Thus, much effort has been concentrated on the attainment of high-β plasma confinement. For tokamaks, which currently operate at $\beta \lesssim 1\%$, there are plans to increase the plasma β by a fast auxiliary heating (e.g., neutral beam injection, rf heating, etc.) as in the flux conserving tokamak[3] concept, or by elongation of the poloidal cross section.

Meanwhile, stable high β ($\sim$50%) plasmas have already been attained in various toroidal pinch experiments (e.g., reverse-field pinch, screw pinch, belt pinch, etc.). But the current pinch machines are generally quite small devices of short duration and thus, the obtained plasma parameters are quite low in view of the ignition temperature and the Lawson criterion. Therefore, larger pinch experiments are planned in several laboratories around the world to scale up the plasma parameters. The scaling character of the pinch discharges is one of the crucial-quastions to be investigated by these larger devices.

In this thesis, we study the plasma behavior of the toroidal pinch experiments using a two-dimensional resistive magneto-hydrodynamic (MHD) calculation. Lui and Chu[1] reported a two-dimensional MHD simulation of the initial phase of the Jutphaas SP-1 screw pinch.[4] In this, the single-fluid MHD equations with finite electrical and thermal conductivities were solved by an Eulerian finite difference scheme in a toroidally

axisymmetric geometry. The plasma was initially at rest, and it was driven by currents and fields prescribed as functions of time. The gross motions of the plasma, namely pinching, bouncing and toroidal shift, were all obtained as part of the solution. In the present study, this code has been modified, so that very long calculations beyond the initial phase are possible.[2] An initially quiet homogeneous plasma, driven by rising external currents which are then crowbarred, can be followed through many pinching and bouncing motions until a quasi-equilibrium dissipation state is reached. The plasma behavior during this process is discussed in Section (4.1). The method of the calculation is described in Chapters (II and III). (In Sections (2.1, 3.1, and 3.2.D), we follow Lui and Chu[1].)

The same code is also used to simulate the Eta-Beta reverse-field pinch at the University of Padua and ZT-I, ZT-S, and ZT-40 reverse-field pinches[5] at Los Alamos. (The Eta-Beta results have been reported in ref. (6).) The ZT-40 device which is currently being constructed, is a larger device compared to the others mentioned here. Comparing the ZT-40 results with others, the scaling behavior of the pinch discharge is studied in Section (4.4). For this, the scaling law of the MHD equations is derived in Section (4.4.A). In Section (4.4.C), we discuss some general confinement characteristics of large pinch experiments.

A strong toroidal flow is seen in the calculation. This flow is sustained while the poloidal flow is damped until it becomes

a diffusion velocity. In other words, the quasi-equilibrium state reached is a steady state rather than a static quasi-equilibrium state. This and other toroidal curvature effects are discussed in Section (4.3.B).

The question of the anomality of the electric resistivity is also studied. For this, the observed field profiles are compared using two separate simulation results, one using the classical resistivity and the other using an anomalous resistivity algorithm (the Chodura algorithm described in Section (2.3)). In the setting-up phase of the discharge, the anomalous algorithm gives somewhat better results than the classical resistivity does. But the difference of the two results is not very significant and both results compare with the experiment quite well. In the later dissipation phase however, the anomalous resistivity algorithm is found not valid and the experimental resistivity seems to be quite close to the classical one. These are discussed in Sections (4.2 and 4.3.A).

We now briefly describe the toroidal reverse-field pinch. The reverse-field pinch (RFP) relies on wall and magnetic shear stabilization for its stability. The reversal of the toroidal magnetic field at the wall is necessary to have nonzero magnetic shear everywhere, when a vacuum region or a low current region exists outside the pinch. Due to shear stabilization, RFP operates with the safety factor $q < 1$.[7] Thus, stable high β plasmas can be produced with an arbitrary aspect ratio device. (cf. The β-values of the tokamaks are limited by the two conditions, poloidal beta $\beta_p \lesssim$ aspect ratio $\frac{R}{a}$, and $q = \frac{aB_t}{RB_p} > \sim 1$.) Due to

the large toroidal current allowed, it may be also possible to heat the plasma to ignition by Joule heating alone.[8]

Figure 1 shows the basic geometry of the torus and the coordinate systems. The highly conducting copper shell is slotted poloidally and toroidally to permit field penetration. Inside, there is a dielectric discharge tube usually made of quartz or alumina. The imposed external toroidal (I_ϕ) and poloidal (I_θ) currents drive the plasma implosion. Figure 2(a) shows time traces of the driving boundary conditions of RFP in the calculation, i.e., the total toroidal plasma current I_{zp}[†] and the toroidal field at the wall, B_{zw}. These functions are directly related to the external currents (cf. Sections 3.2.B and 3.2.C). The plasma current I_{zp} is not strictly a boundary condition of the calculation, but rather it is used as a constraint for an actual boundary value, volt-seconds around the torus (cf. Section 3.2.B). Figure 2(b) shows typical toroidal (B_z) and poloidal field (B_θ) profiles. The direction of B_z is reversed at the wall.

There are two different methods of producing the RFP configuration, i.e., one by a fast field programming; the other from self reversal. The self reversal[9] occurs due to a helical instability which relaxes the discharge to a minimum energy state as can be explained by Taylor's theory in ref. (10). Thus, to study the self-reversal mode, a three-dimensional calculation[9] is necessary. On the other hand, the driven reversal mode is an axisymmetric process and thus, will be studied in the present thesis.

---

† Subscript z represents ϕ direction, not Z direction.

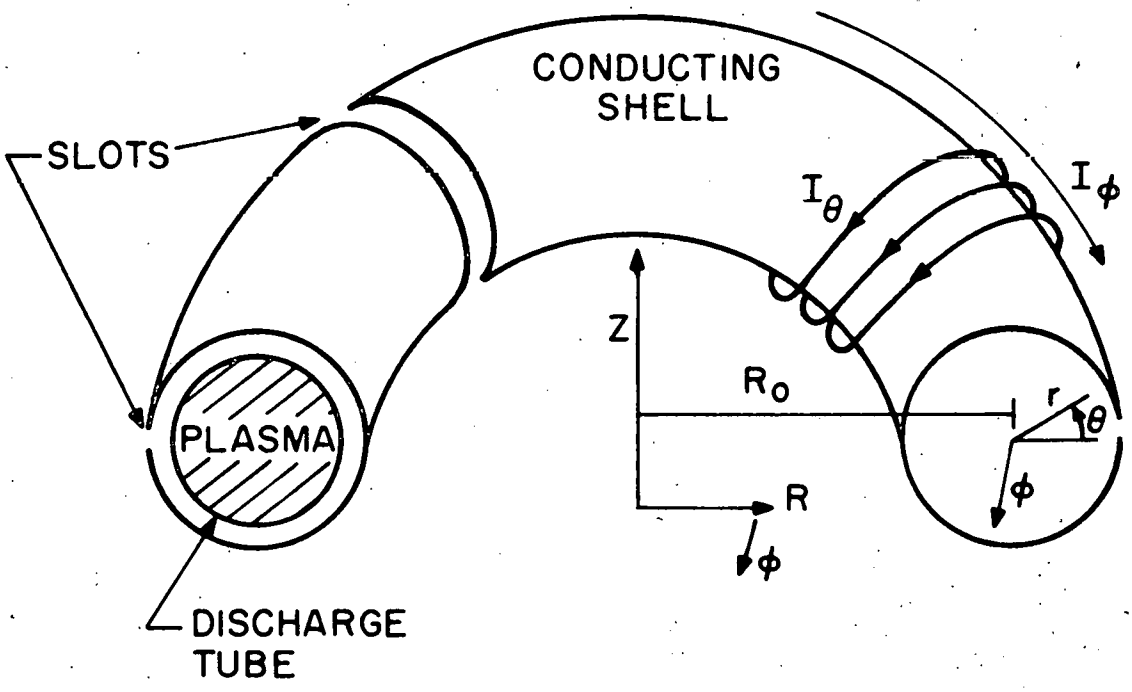

FIG. 1. BASIC GEOMETRY OF A TOROIDAL PINCH AND COORDINATE SYSTEMS

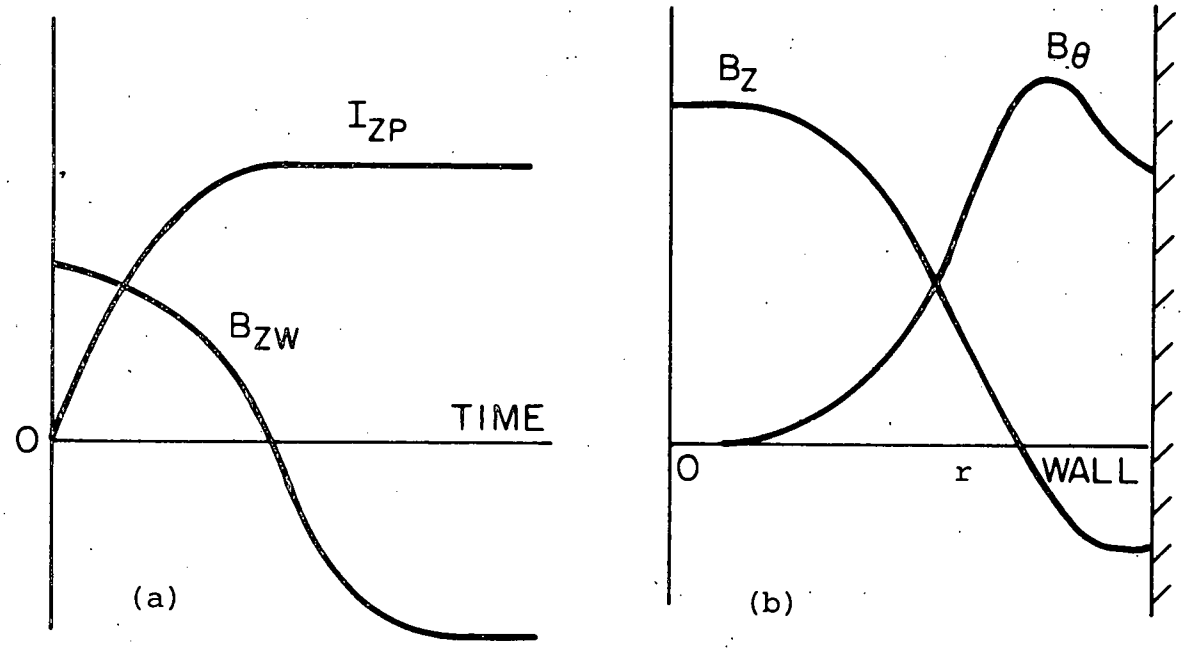

FIG. 2. TYPICAL REVERSE-FIELD PINCH CONDITIONS: (a) TIME TRACES OF THE TOROIDAL PLASMA CURRENT I_{ZP} AND THE TOROIDAL MAGNETIC FIELD AT THE WALL, B_{zw}; (b) PROFILES OF THE TOROIDAL FIELD B_z AND THE POLOIDAL FIELD B_θ.

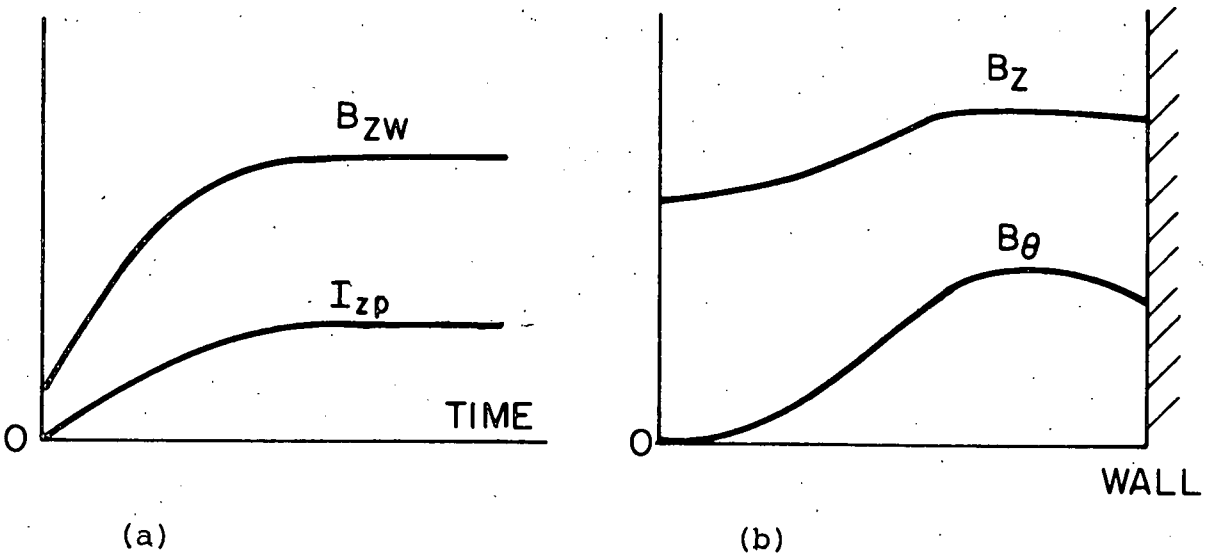

FIG. 2'. TYPICAL SCREW PINCH CONDITIONS.

The screw pinch is similar to RFP in geometry. But instead of the magnetic shear, screw pinch relies on the stabilizing effect of $q > \sim 1$, and on force-free currents.[4] Due to force-free currents, some reduction of q-value is possible.[4] Figure 2'(a) shows the driving boundary conditions of screw pinch in the calculation, and should be compared to Figure 2(a) of the RFP case. Typical field profiles are shown in Figure 2'(b). Unlike in the RFP case, the toroidal field contributes to plasma confinement. But this contribution will be only comparable to the poloidal field contribution (i.e., $\beta_p \sim 1$), even when $B_z >> B_\theta$, especially in a large experiment, as explained in Section (4.4.C).

II. FORMULATION OF THE PROBLEM

The calculation will follow plasma behavior starting from its initial state at rest, through many pinching and bouncing motions until it reaches a quasi-equilibrium dissipation state (where the plasma oscillation has been damped away and thus, diffusion mechanisms determine the radial plasma velocity). The equations to be solved are derived in the following section. We adopt the single fluid resistive magnetohydrodynamic (MHD) model of the plasma. The usual criteria[11] for the applicability of the MHD equations are well satisfied in the smaller experiments, SP-1, ZT-I, and ZT-S, due to high density and low temperature in the discharges. In fact, the calculation results agree well with the experimental measurements as will be shown in Chapter IV. For the larger ZT-40 experiment, however, the mean free path will become comparable to the torus dimension and much larger than the ion gyroradius due to higher temperature, and thus, the applicability of the MHD equations is questionable. Therefore, the present model of the plasma should be regarded as a crude approximation in the ZT-40 case. (e.g., The neoclassical effect might become important.)

Toroidal symmetry is assumed. The implication and the validity of this assumption are discussed in Section (2.2). Finite electrical and thermal conductivities are included but the viscosity is neglected. These transport coefficients are explained in Section (2.3).

According to the geometry of the boundary (Figure 1), toroidal polar coordinates (r, θ, ϕ) are used throughout, rather than cylindrical coordinates (R, Z, ϕ). The distance R from the major axis, $R = R_o + r\cos\theta$, is often used in the equation for brevity. The units are Gaussian unless otherwise specified.

2.1 Derivation of the Basic Equations

The differential equations of single fluid magnetohydrodynamics with finite electrical and thermal conductivities are

$$\frac{\partial \rho}{\partial t} + \nabla\cdot(\rho \underline{u}) = 0 , \tag{1a}$$

$$\frac{\partial \rho \underline{u}}{\partial t} + \nabla\cdot(\rho \underline{u}\underline{u}) = -\nabla p + \underline{j} \times \underline{B}/c , \tag{1b}$$

$$\rho C_v\left(\frac{\partial T}{\partial t} + \underline{u}\cdot\nabla T\right) = -p\nabla\cdot\underline{u} + j^2/\sigma + \nabla\cdot(K\nabla T) , \tag{1c}$$

$$\frac{1}{c}\frac{\partial \underline{B}}{\partial t} = -\text{curl } \underline{E} , \tag{1d}$$

$$\underline{j} = \frac{c}{4\pi}\text{ curl } \underline{B} , \tag{1e}$$

$$\text{div } \underline{B} = 0 , \tag{1f}$$

$$\begin{aligned}\underline{E} &= \underline{j}/\sigma - \underline{u}_e \times \underline{B}/c \\ &= \underline{j}/\sigma - \underline{u} \times \underline{B}/c + \frac{\underline{j}}{ne} \times \underline{B}/c ,\end{aligned} \tag{1g}$$

where σ and K are electric and thermal conductivities, C_v is the specific heat at constant volume, n is the electron number density ($n = \rho/M_{atom}$, for a hydrogen or deuterium filling gas),

and $\underline{u}_e = \underline{u} - \frac{\underline{j}}{ne}$ is the electron fluid velocity. ($\underline{u}_e$ will be used in the equations for brevity instead of using $(\underline{u} - \frac{\underline{j}}{ne})$.) The Hall term is included in the Ohm's law (1g), because the drift velocity, $\underline{V}_d = \underline{j}/ne$, is often of the same order of magnitude as the fluid velocity $\underline{u}$. (In other words, the condition[11] $\frac{L\omega_{pe}^2}{\omega_{ce}} \frac{V_o}{c^2} >> 1$ for neglecting the Hall term is not satisfied.)

We now derive the equations to be solved in (r, θ, ϕ) coordinates, assuming toroidal axisymmetry $(\frac{\partial}{\partial \phi} = 0)$. Since div $\underline{B} = 0$, we define as usual a poloidal flux function ψ as

$$\psi_{(r,\theta)} = \frac{1}{2\pi} \int_{F(r,\theta)} \underline{B} \cdot ds \qquad (2)$$

where F represents any open surface bounded by a large circle around the torus at (r, θ). Differentiating each side of equation (2), and using axisymmetry, we obtain the usual representation for $\underline{B}$,

$$\underline{B} = - \frac{\hat{\phi}}{R} \times \nabla\psi + B_\phi \hat{\phi} \quad .$$

The toroidal field B_ϕ is more conveniently represented by introducing a variable $\chi = RB_\phi$. Then each component of $\underline{B}$ is represented by ψ, χ, and their derivatives, as

$$B_r = \frac{1}{Rr} \frac{\partial\psi}{\partial\theta}, \quad B_\theta = - \frac{1}{R} \frac{\partial\psi}{\partial r}, \quad B_\phi = \frac{\chi}{R} \; . \qquad (3)$$

The current density components are also so expressed from Ampere's Law (1e),

$$j_r = \frac{c}{4\pi Rr}\frac{\partial \chi}{\partial \theta}, \quad j_\theta = -\frac{c}{4\pi R}\frac{\partial \chi}{\partial r},$$

$$j_\phi = -\frac{c}{4\pi}\{\frac{1}{r}\frac{\partial}{\partial r}(\frac{r}{R}\frac{\partial \psi}{\partial r}) + \frac{1}{r}\frac{\partial}{\partial \theta}(\frac{1}{Rr}\frac{\partial \psi}{\partial \theta})\}. \tag{4}$$

Integrating the induction equation (1d) over the surface $F(r, \theta)$, we obtain

$$-\frac{1}{cR}\frac{\partial \psi}{\partial t} = E_\phi . \tag{5}$$

Substituting equations (3, 4, and 5) into Ohm's Law (1g), we obtain the differential equation for ψ,

$$\frac{\partial \psi}{\partial t} + u_{er}\frac{\partial \psi}{\partial r} + u_{e\theta}\frac{\partial \psi}{r\partial \theta}$$
$$= \frac{c^2}{4\pi\sigma}\{\frac{R}{r}\frac{\partial}{\partial r}(\frac{r}{R}\frac{\partial \psi}{\partial r}) + \frac{R}{r}\frac{\partial}{\partial \theta}(\frac{1}{R}\frac{\partial \psi}{r\partial \theta})\}. \tag{6a}$$

Substituting equations (3 and 4) first into Ohm's Law (1g) and then into the induction equation (1d), we obtain the equation for χ

$$\frac{\partial \chi}{\partial t} = \frac{c^2}{4\pi}\{\frac{R}{r}\frac{\partial}{\partial r}(\frac{r}{\sigma R}\frac{\partial \chi}{\partial r}) + \frac{R}{r}\frac{\partial}{\partial \theta}(\frac{1}{\sigma Rr}\frac{\partial \chi}{\partial \theta})\}$$

$$-\frac{R}{r}\frac{\partial}{\partial r}(\frac{r}{R}u_{er}\chi) - \frac{R}{r}\frac{\partial}{\partial \theta}(\frac{1}{R}u_{e\theta}\chi)$$

$$+\frac{R}{r}\frac{\partial}{\partial r}(rB_r u_{e\phi}) + \frac{R}{r}\frac{\partial}{\partial \theta}(B_\theta u_{e\phi}) . \tag{6b}$$

The energy equation (1c) gives the equation for temperature T which is of the same form in these coordinates,

$$\rho C_v\left(\frac{\partial T}{\partial t} + u_r \frac{\partial T}{\partial r} + u_\theta \frac{\partial T}{r\partial\theta}\right) =$$

$$\frac{j_r^2 + j_\theta^2 + j_\phi^2}{\sigma} + \frac{1}{Rr}\frac{\partial}{\partial r}\left(KRr \frac{\partial T}{\partial r}\right)$$

$$+ \frac{1}{Rr}\frac{\partial}{\partial\theta}\left(KR \frac{\partial T}{r\partial\theta}\right)$$

$$-(\gamma-1)\rho C_v T\left\{\frac{1}{Rr}\frac{\partial}{\partial r}(Rr\, u_r) + \frac{1}{Rr}\frac{\partial}{\partial\theta}(Ru_\theta)\right\}, \qquad (6c)$$

where the ratio of specific heats γ is 5/3 for three degrees of freedom for each particle. Equations (6a, 6b, and 6c), which govern the time evolution of ψ, χ and T form a group of three parabolic equations. On the other hand, the mass and momentum equations, (1a) and (1b), form an essentially hyperbolic system* of four equations. These are in (r, θ, ϕ) coordinates

$$\frac{\partial}{\partial t}\rho + \frac{1}{r}\frac{\partial}{\partial r}(r\rho u_r) + \frac{\partial}{r\partial\theta}(\rho u_\theta)$$

$$= -\frac{\rho(u_r\cos\theta - u_\theta\sin\theta)}{R}, \qquad (7a)$$

$$\frac{\partial}{\partial t}(\rho u_r) + \frac{1}{r}\frac{\partial}{\partial r} r(\rho u_r^2 + (\gamma-1)\rho C_v T) + \frac{1}{r}\frac{\partial}{\partial\theta}(\rho u_r u_\theta)$$

$$= -\frac{\rho u_r}{R}(u_r\cos\theta - u_\theta\sin\theta) + \frac{\rho u_\theta^2}{r} + \frac{\rho u_\phi^2\sin\theta}{R}$$

$$+ \frac{1}{c}(j_\theta B_\phi - j_\phi B_\theta), \qquad (7b)$$

---

* Although in actuality, these 4 equations together with the 3 parabolic equations (6) form a parabolic system of 7 equations since they are coupled together, we will refer to these 4 equations as a hyperbolic system for convenience.

$$\frac{\partial}{\partial t}(\rho u_\theta) + \frac{1}{r}\frac{\partial}{\partial r}(\rho r u_r u_\theta) + \frac{1}{r}\frac{\partial}{\partial \theta}(\rho u_\theta^2 - (\gamma-1)\rho C_v T)$$

$$= -\frac{\rho u_\theta}{R}(u_r\cos\theta - u_\theta\sin\theta) - \frac{\rho u_r u_\theta}{r} - \frac{\rho u_\phi^2}{R}\sin\theta$$

$$+ \frac{1}{c}(j_\phi B_r - j_r B_\phi) \quad , \tag{7c}$$

$$\frac{\partial}{\partial t}(\rho u_\phi) + \frac{1}{r}\frac{\partial}{\partial r}(\rho r u_r u_\phi) + \frac{1}{r}\frac{\partial}{\partial \theta}(\rho u_\theta u_\phi)$$

$$= -\frac{2\rho u_\phi}{R}(u_r\cos\theta - u_\theta\sin_\theta) + \frac{1}{c}(j_r B_\theta - j_\theta B_r) \quad . \tag{7d}$$

For convenience in later explanation, we represent these four hyperbolic equations as a vector equation,

$$\frac{\partial \underline{W}}{\partial t} + \frac{1}{r}\frac{\partial}{\partial r}(rA(\underline{W},T)\cdot\underline{W}) + \frac{\partial}{r\partial\theta}(B(\underline{W},T).\underline{W})$$

$$= \underline{S}(\underline{W}, T, r, \theta) + \underline{F}(\underline{j}, \underline{B}), \tag{8}$$

where $\underline{W} = (\rho, \rho u_r, \rho u_\theta, \rho u_\phi)$, A and B are 4×4 matrices,

$$A = \begin{pmatrix} 0, & 1, & 0, & 0 \\ (\gamma-1)C_v T, & u_r, & 0, & 0 \\ 0, & 0, & u_r, & 0 \\ 0, & 0, & 0, & u_r \end{pmatrix}, \quad B = \begin{pmatrix} 0, & 0, & 1, & 0 \\ 0, & u_\theta, & 0, & 0 \\ (\gamma-1)C_v T, & 0, & u_\theta, & 0 \\ 0, & 0, & 0, & u_\theta \end{pmatrix},$$

and $\underline{S}$ contains all the undifferentiated terms involving $\underline{W}$, T, and the coordinate variables and represents the curvature effects, while $\underline{F}$ represents $\underline{j} \times \underline{B}/c$ term.

2.2 A Remark on the Toroidal Axisymmetry

Toroidal axisymmetry is a basic assumption in our study. If the initial conditions and the driving boundary conditions are all axisymmeric, the plasma will develop in an axisymmetric way, unless axially asymmetric instabilities occur in which case our calculation is no longer applicable. While most of the conditions are rather obviously axisymmetric, the fact that the electric field which penetrates through the slots also gives axisymmetric effect on the plasma, would require some explanation, since this $\underline{E}$ field itself is much asymmetric in fact.

In general, the $\underline{E}$ field can be represented uniquely as a superposition of two fields,[13]

$$\underline{E} = \underline{E}_B + \underline{E}_\sigma ,$$

where $\underline{E}_B$ is a divergence free field generated by curl $\underline{E}_B = -\frac{\partial \underline{B}}{c\partial t}$, while $\underline{E}_\sigma$ is a curl free field generated by div $\underline{E}_\sigma = 4\pi\sigma$. In our case, it is easy to see that $\underline{E}_B$ is axisymmetric while $\underline{E}_\sigma$ is axially asymmetric. Thus, at the conducting wall (inside surfase of the shell), $E_{B\phi}$ is constant around the torus. $E_{\sigma\phi}$ is also constant as long as one stays away from the slot, since $E_{\sigma\phi} = -E_{B\phi}$ at the wall to satisfy the boundary condition $E_\phi = 0$ at a conducting surface. However at the slot, $E_{\sigma\phi}$ becomes very large representing large Poynting's vector into the torus. This asymmetric $\underline{E}_\sigma$ field however, will have little effect on the plasma behavior, since the plsma will react immediately to shield out the curl free $\underline{E}_\sigma$ field by charge separation on the plasma surface.

More precisely, $\underline{E}_\sigma$ generated by σ on both conducting shell surface and the plasma surface will be such that $E_{\sigma\phi} = -E_{B\phi}$ on the conducting shell surface(both inside and outside) away from the slot, $\underline{E}_\sigma = 0$ inside the plasma, $E_{\sigma\phi} = 0$ on the plasma surface and $\int_0^{\Delta x} E_{\sigma\phi} \cdot dx = \frac{E_{B\phi} 2\pi R}{N}$ at the slot(Δx is the width of the slot, N the number of slots). It is easy to verify that these conditions together with the fact that the total charge in the plasma and the total charge in each shell segment are all zero, determine a unique solution of σ. We note that the charge density $\sigma(\underline{r},t)$ specified in this argument, together with the solution of the problem posed in Section(2.1), gives a solution of the actual problem in the MHD limit.

In short, the $\underline{E}$ field inside the plasma will remain axisymmetric although the $\underline{E}$ field outside the plasma is highly asymmetric. This fact has been explained concerning the poloidal slots. The effect of the toroidal slots can also be explained in a similar way. These are also the reason why we can use later, two seemingly contradictory boundary conditions, $B_n = 0$ and E_ϕ, $E_\theta \neq 0$ on the conducting surface. In fact, the experimental measurements in nearly all of the axisymmetric toroidal experiments, show close toroidal symmetry of the plasma behavior.

2.3 Transport Coefficients

The classical transport coefficients[14] which are derived from binary encounter theory sometimes do not satisfy the experimental measurements. Although other reasons may well be important,[15] this is generally attributed to turbulence created by plasma instabilities. Thus, some simulation studies on toroidal pinches reported the transport to be significantly anomalous while other studies on different toroidal pinches reported the transport to be classical. One anomalous case was reported by Krall and Liewer[16] who used an electric resistivity algorithm where the effects of various instabilities are taken into account self-consistently, using the known properties of the instabilities. The results thus obtained agreed with the theta pinch experiment at the University of Texas. A more simple semi-empirical resistivity algorithm has been also reported to describe satisfactorily the behavior of the plasma in the Garching theta pinch (by Chodura[17]) and ZT-1 reverse field pinch (by Sgro and Nielson[18]), when it is used in a hybrid model (Vlasov ions, fluid electrons) of the plasma in one dimensional calculations.

On the other hand, the Culham group reported that the HBTX-1 reverse-field pinch had been successfully simulated using the classical transport coefficients.[19] Another study had been done by the University of Padua group who reported that "No clear indication about the classical or anomalous

nature of the resistivity appears from the simulated gross plasma behavior of Eta-Beta reverse-field pinch discharge."[20]

In the present study, we test both the classical resistivity formula and the anaomalous resistivity algorithm of Chodura[17], comparing the obtained results with the experiments. In the Chodura anomalous resistivity algorithm, the resistivity is found as follows:

$$\nu = c\omega_{pi}[1 - \exp(-|V_d|/fV_s)],$$

$$\eta = \text{Max}(\nu M_e / ne^2, \eta_{classical}), \qquad (9)$$

where the ion acoustic speed $Vs = (\gamma kT_e/M_i)^{1/2}$, the drift velocity $V_d = j/ne$, and the coefficients $c = 0.5$ and $f = 5.0$. These same numerical coefficients are used in the present study. This algorithm gives a classical resistivity when the ratio of the electron drift velocity to the ion acoustic speed is small, but an empirically enhanced value will be switched on when the ratio becomes large. The density dependence of this formula is also important especially in the low density region outside the main plasma column, since the classical formula does not have much dependence on density. Here, we note that the resistivity η is used as a scalar. Some efforts were made initially, to use this resistivity coefficient in a tensor form as used by Sgro and Nielson[18]. But test runs indicate that the anisotropy of the resistivity is not important enough in our simulation to warrant the necessary complications and loss in numerical stability.

It is shown in Section (4.2) and (4.3) that for the initial setting up phase of the ZT-I and ZT-S experiments, the Chodura anomalous algorithm gives somewhat better results than the pure classical formula. But the difference is not very significant and both results agree with the experiment quite well so that a conclusion similar to that of the Padua group stated above is drawn. It is noted that the Eta-Beta experiment is in a similar parameter range as ZT-I and ZT-S experiments. In the later dissipation phase however, the Chodura resistivity algorithm is found not valid and the resistivity seems to be quite close to the classical one.

As for the thermal conductivity, if the classical formula is used, the results did not compare with the experiment. This is because the classical formula gives no conduction across the wall, as explained in the following, while the experiment shows significant heat loss. In the tenuous plasma region outside the pinched main plasma column (cf. Section 3.3), the plasma density is negligible while the magnetic field and temperature are substantial. Thus, $\omega\tau \to \infty$, where ω and τ are the cyclotron frequency and the collision time, respectively. When $\omega\tau \to \infty$, the perpendicular conductivity[14] becomes $K^{\perp} \sim K_i^{\perp} \to \frac{2nk^2 T_i \tau_i}{m_i (\omega\tau)_i^2}$, where the subscript i represents the ion species. Since this value will be negligible near the wall and the magnetic field is parallel to the wall, there will be zero net energy loss

from the torus system in the calculation. On the other hand, in the experiments, the energy loss due to the radiation and conduction is generally significant. In some discharges (e.g., some of the Eta-Beta discharges)[22], the radial loss was found negligible, even though the total energy loss was significant. Therefore, it seems that in general, some anomalous conduction loss is present together with the radiation loss.

In the present study, we simply set the thermal conductivity coefficient at a constant $K = 2 \times 10^6$ erg/cm · sec·°K (which corresponds to the classical parallel conductivity at ~4 eV), which was found satisfactory in our previous simulation of the Eta-Beta reverse-field pinch. This value is again found acceptable for the simulation of ZT-I, ZT-S and SP-1, all of which are in a similar parameter range as Eta-Beta. In our calculation where the radiation loss is neglected, this would imply that the net conduction loss in the calculation is on the same order of magnitude as the net energy loss in the experiment through both conduction and radiation.

The other transport mechanism, i.e., the viscosity, is neglected in the present calculation. The classical viscosity, is mainly due to the ion species and the parallel and perpendicular coefficents are on the same order of magnitude. The kinematic viscosity coefficient[21] is roughly

$$\nu \simeq \nu_i \sim \frac{kT_i\tau_i}{M_i} .$$

For the smaller machines, i.e., SP-1, ZT-I, and ZT-S, the viscous

dissipation time scale $\tau_\nu = \frac{r_o^2}{\nu}$ is on the order of 1 ms. (It will be shown in Section (3.1) that the numerical viscosity is also on this order.) This is much longer than the time of interest in our calculation since the Alfven time scale for these smaller machines is $\sim$ 1 μs, and the field and heat diffusion times are both $\sim$10 μs. (cf. Section (4.1)). This justifies the assumption of no viscosity in the calculation. On the other hand, in a larger ZT-40 experiment, the viscous dissipation time becomes $\sim$10μs due to higher temperature, assuming the classical viscosity. Thus, the viscosity might be important in this case. A further discussion on this subject is made in Section (4.4.B).

2.4 Initial Conditions

Although our code can start from any initial condition, the initial conditions for the present simulation are very simple. We start the calculation from an ionized plasma at rest which corresponds to the beginning of the main discharge in the experiment. We assume initial full ionization. A given toroidal bias field $B_{\phi bias}$ is present without any current. Therefore the initial conditions are

ρ = Const., ρU_r, ρU_θ $\rho U_\phi = 0$

T = Const. (typically $1 \sim 10$ eV depending on the pre-ionization.)

$\psi = 0$, $\chi = RB_{\phi bias}$.

III. NUMERICAL SOLUTION PROCEDURE

3.1 Basic Numerical Procedure

We use an Eulerian finite difference scheme to solve numerically the seven nonlinear equations (6 and 7) formulated in the previous chapter. The standard alternating direction implicit scheme[12] (implicit in r or θ direction, alternatively) is used for both parabolic (6) and hyperbolic equations (7). The solution procedure is explained in the following.

We first calculate the predicted value $\underline{W}^* = (\rho, \rho U_r, \rho U_\theta, \rho U_\phi)^*$ for the coefficients of the nonlinear terms from W^n of the old time step by an explicit scheme (as usual, n denotes the time step, and i, j denote the indices in the r and θ direction respectively, i.e., $F^n_{i,j} = F(i\Delta n, j\Delta\theta, n\Delta t)$),

$$\underline{W}^*_{i,j} = \underline{W}^n_{i,j} - \Delta t(H_r (A^n \cdot \underline{W}^n)_{i,j} + H_\theta (B^n \cdot \underline{W}^n)_{i,j}) \quad (10)$$
$$+ \Delta t(\underline{S}^n_{i,j} + \underline{F}^n_{i,j})$$

where, for any vector $\underline{V}$,

$$H_r \underline{V}_{i,j} \equiv (r_{i+1} \underline{V}_{i+1,j} - r_{i-1} \underline{V}_{i-1,j})/r_i 2\Delta r,$$

$$H_\theta \underline{V}_{i,j} \equiv (\underline{V}_{i,j+1} - \underline{V}_{i,j-1})/r_i \Delta 2\theta \ .$$

This $\underline{W}^*$ is then used in the coefficients, e.g., as

$U^*_{er} = U^*_r - (\frac{j_r}{ne})^n$, to calculate the new time step

values for the three variables, ψ^{n+1}, χ^{n+1} and T^{n+1}, using an alternate direction implicit scheme.

Finally, the new time step value $\underline{W}^{n+1}$ is calculated by solving the hyperbolic equations (6) with an alternate direction implicit scheme. Here $\underline{W}^*$ is used for the nonlinear coefficients and $\underline{S}$ is approximated by $\frac{1}{2}(\underline{S}^n + \underline{S}^*)$, $\underline{F}$ by $\frac{1}{2}(\underline{F}^n + \underline{F}^{n+1})$. The difference equation for $\underline{W}$, at the r direction implicit time step for example, is as follows:

$$\underline{W}_{i,j}^{n+1} + \Delta t\, H_r\, (A^*_{i,j}\, \underline{W}_{i,j}^{n+1})$$

$$= \underline{W}_{i,j}^{n} - \Delta t H_\theta (B^n_{i,j}\, W^n_{i,j})$$

$$+ \frac{1}{2}(\underline{S}^* + \underline{S}^n) + \frac{1}{2}(\underline{F}^n + \underline{F}^{n+1}). \qquad (11)$$

This difference scheme, together with the boundary conditions explained later in this chapter, results in a 4 x 4 block tridiagonal matrix equation $P\ \underline{x} = \underline{f}$, where P and $\underline{f}$ are given. Likewise in the solution procedure for ψ, χ and T, we encounter a similar tridiagonal matrix equation. These matrix equations are efficiently solved by Crout reduction[23].

Of course, if we iterate back and forth between the parabolic and the hyperbolic equations, the results will be more accurate than the results from the present method. But this would require much more computer time.

To enhance numerical stability, a Lapidus type numerical viscosity term[12,24] is added in the right side of the equation (11). This viscosity term is

$$\kappa\{\frac{\Delta t}{\Delta r}\,\delta_r(|\delta_r U_r^n\,|\delta_r \underline{W}^n)_{i,j} + \frac{\Delta t}{r_i \Delta\theta}\,\delta_\theta(|\delta_\theta U_\theta^n|\delta_\theta \underline{W}^n)_{i,j}\} \tag{11+}$$

where

$$\delta_r \underline{V}_{i,j} \equiv \underline{V}_{i+\frac{1}{2},j} - \underline{V}_{i-\frac{1}{2},j}\ ,$$

$$\delta_\theta \underline{V}_{i,j} \equiv \underline{V}_{i,j+\frac{1}{2}} - \underline{V}_{i,j-\frac{1}{2}}\ ,$$

and the coefficient of the viscosity term κ is typically 0.1. For the velocity of $10^5 \sim 10^6$ cm/sec and $\Delta r, r\Delta\theta \sim 1$ cm, we estimate the effective viscous dissipation time $\tau_\nu = \frac{r_o^2}{\nu}$ of this dissipation term to be 100 ~1000 μs. Since, this time scale is considerably longer than the time scale of the calculation (cf. Chapter IV), this artificial viscosity term can be justified.

We note here that using the predictor value $\underline{W}^*$ as given in equation (10) sometimes causes a numerical instability in the simulation of a very violent process. In such a case, we use a slightly less accurate procedure which gives better numerical stability, that is, we simply find $\underline{W}^*$ without the predicting terms in equation (10) but, adding a dissipation

term, i.e.,

$$\underline{W}^{*} = (1 - \theta)\underline{W}^{n}_{i,j} + \frac{1}{4}\theta(\underline{W}^{n}_{i+1,j} + \underline{W}^{n}_{i-1,j} + \underline{W}^{n}_{i,j+1} + \underline{W}^{n}_{i,j-1}), \quad (10')$$

where the dissipation constant $\theta = 0.1$.

Due to the complex nonlinearity of the equations, a rigorous overall error analysis for the solution of the difference scheme described in this section would be exceedingly difficult, if not impossible. Therefore, we took the usual approach of comparing results of the code obtained with different grid sizes and time steps. If the solutions obtained under these conditions are converging to a solution, it is assumed that the solution obtained is correct. This is because the truncation errors are at least first order both in the grid size and in the time step. In this way (e.g., by noticing that the results do not change significantly when the grid and time step sizes are reduced to a half), it is also checked that the effective dissipation time due to the overall numerical dissipation is much longer than the calculation time scale which is in the order of 10 μs.

3.2 Boundary Conditions

For the boundary conditions of the system of seven differential equations (6) and (7), we first consider the dissipation-free case, where the dissipation coefficients are all zero. The boundary conditions for these hyperbolic equations can be determined by examining the characteristics[25]. Since there is no plasma flow across the wall and also since we require that no vacuum region appears near the wall (cf. Section (3.3)), a boundary condtion $U_r = 0$ is necessary. This condition $U_r = 0$ and the fact that the magnetic fields are parallel to the wall, allow only one characteristic (a fast (magnetosonic) wave) to point into the domain. Therefore, $U_r = 0$ is a sufficient boundary condition for this case. (If $U_r < 0$, all six boundary values except the one for the density ρ would be necessary.)

On the other hand, for the present dissipative magnetohydrodynamic equations with finite electric and thermal dissipation coefficients, the system become parabolic and additional boundary conditions for the variables ψ, χ and T are necessary. For these variables, either a Dirichlet boundary condition (e.g., T = Const.) or a Neumann boundary condition (e.g., $\frac{\partial T}{\partial r} = 0$) for each variables, is sufficient both for the differential equations and for the difference equations. The boundary conditions used are explained in detail in Section (3.2.B).

Furthermore, for the variables $\underline{W} = (\rho, \rho U_r, \rho U_\theta, \rho U_\phi)$, the difference scheme may need additional extraneous boundary conditions, and careless imposing of these conditions may cause various difficulties, e.g., numerical boundary layers,

numerical instability, etc. (cf. Ref. (26)). In the following section, these extraneous boundary conditions for $\underline{W}$ are derived from the constraint that there is no mass and momentum flow across the wall. For this procedure, we should first define the mass and momentum flow between computational grids, consistantly with the difference scheme used. This is also shown in the following section.

The boundary condtions for the θ direction are given in Section (3.2.D). Finally the treatment in the coordinate origin $r = 0$ is discussed in Section (3.2.E). This procedure is necessary because the origin $r = 0$ is a boundary point for the coordinates (r,θ,ϕ) even though it is an interior point of the plasma.

3.2.A. Interpretation of the Basic Difference Scheme and the Boundary Conditions

We first explain the definition of the mass flow between computational grids, using a one dimensional analogy of the mass conservation equation, that is,

$$\rho^{n+1} - \rho^{n} + \frac{\Delta t}{2\Delta x}(\rho U^{n+1}_{i+1} - \rho U^{n+1}_{i-1}) = 0 \qquad (12)$$

Fig. 3 shows the computational mesh scheme in one dimensional analogy. (The two dimensional case is shown in Fig. 4 on page ( ).) All the variables ρ and U are defined at the integral points I's. Naturally, the mass inside the unit grid I is defined as $\rho_i \Delta x$.

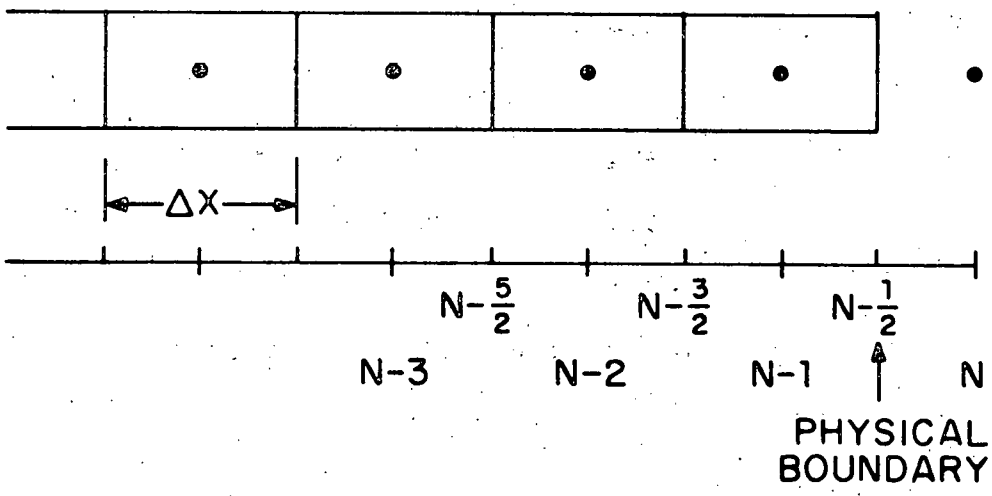

FIG. 3, COMPUTATIONAL MESH SCHEME IN ONE DIMENSIONAL ANALOGY.

If we calculate the mass change in the grid N_1 through N_2 using equation (12),

$$\Delta M = \Delta t \sum_{i=N_1}^{N_2} \frac{1}{2}(\rho U_{i-1} - \rho U_{i+1})$$

$$= \Delta t \left(\frac{\rho U_{N_1+1}+\rho U_{N_1}}{2} - \frac{\rho U_{N_2}+\rho U_{N_2+1}}{2}\right)$$

$$= \Delta t\left((\rho U)_{N_1+\frac{1}{2}} - (\rho U)_{N_2+\frac{1}{2}}\right) \quad . \tag{13}$$

Thus, the mass flux density ρU through the point $N_{2+\frac{1}{2}}$ can be defined as

$$(\rho U)_{N_2+\frac{1}{2}} = \frac{\rho U_{N_2} + \rho U_{N_2+1}}{2} ,$$

and the symmetry of this equation shows that the difference scheme (12) exactly conserves mass if the boundary conditions are accordingly defined. If we set the position of the actual physical boundary at the point $N-\frac{1}{2}$ (Fig. 3), the zero mass flow condition at the wall, i.e., $\rho U_{N-\frac{1}{2}} = \frac{\rho U_{N-1}+\rho U_N}{2} = 0$ gives the boundary condition

$$(\rho U)_N = -(\rho U)_{N-1} \tag{14a}$$

Such a specification would conserve total mass exactly.

From a similar reasoning for the momentum equation, the zero momentum flow condition determines another boundary condition,

$$(\rho UU)_N = -(\rho UU)_{N-1} \qquad (14b)$$

Although setting the boundary conditions as $\rho_N = -\rho_{N-1}$ and $U_N = U_{N-1}$ would satisfy the above two conditions, the condition $\rho_N = -\rho_{N-1}$ can not be used due to the ∇P term in the momemtum equation. (The boundary condition for the ∇P term will be explained later in this section.) Therefore, we can either use the boundary conditions (14a) and (14b) incorporating them directly into the solution procedure, or we can substract at each time step, the artificial flow passing through the physical boundary point $N-\frac{1}{2}$, that is $\Delta t \rho U_{N-\frac{1}{2}} = \Delta t \frac{\rho U_{N-1}}{2}$, if U_N is set at zero for example in the mass equation. These two methods yield nearly identical results.

In an analogous way to the above, we can easily find the boundary conditions for the difference equation (11) in our two dimensional case. (The mesh scheme is shown in Fig. 4.) For example, the mass flux density through $r_{i+\frac{1}{2}}$ in r direction is defined as

$$\frac{(r\rho Ur)_i + (r\rho Ur)_{i+1}}{r_i + r_{i+1}} \qquad (15)$$

From this equation and the similar equations for the ρU_r, ρU_θ and ρU_ϕ flux densities, we find the boundary conditions,

$$(r\rho U_r)_N = -(r\rho U_r)_{N-1},$$

$$(r\rho U_r U_r)_N = -(r\rho U_r U_r)_{N-1},$$

$$(r\rho U_r U_\theta)_N = -(r\rho U_r U_\theta)_{N-1},$$

$$(r\rho U_r U_\phi)_N = -(r\rho U_r U_\phi)_{N-1}, \qquad (16)$$

where N denotes the boundary index (i_{max} in Fig. 4) for the r direction, and the zero ϕ momentum flow condition across the wall is used for the fourth equation, for example.

The necessity of these 'correct' boundary conditions can be seen, in a one dimensional analogy (Fig. 3), from a case where the boundary value $(\rho U)_N$ is given incorrectly as $(\rho U)_N = 0$ which seems to represent zero mass flow, therefore often used. Then, because of the artificial mass flow through the wall, i.e., $(\rho U)_{N-\frac{1}{2}} = \frac{1}{2}(\rho U)_{N-1}$, twice the mass in the cell (N-1) will be swept in at each inward pinching of the plasma. (Here $(\rho U)_{N-1} \simeq (\rho U)_{N-2}$ is used.) This error is quite severe in a polar mesh scheme (Fig. 4) for a circular cross section torus. For example, with 16 grid points in the r direction, this error will cause an artificial increase of $\sim$15% of the

total plasma mass at the end of the first pinching. This large error is due to the fact that this error is of zeroth order in Δr. We note that the boundary conditions (16) do not take into account the toroidal curvature. But this error is of first order in Δr with very small coefficients. This method of treatment of mass and momentum flow will also be used for the treatment of the low density region described in Section (3.3).

For the hyperbolic equations (7), the boundary condition for ∇P term, $\nabla(\gamma-1)C_v\rho T$, still remains to be determined. This will be determined as before, from the meaning of the term. From a similar reasoning as in the mass flow case, the pressure at the wall is represented by

$$(\rho T)_{N-\frac{1}{2}} = \frac{(\rho T)_N + (\rho T)_{N-1}}{2} .$$

But unlike in the previous situation, there is no constraint which can be used to determine the boundary value exactly. This time we can simply set the boundary condition as $(\rho T)_N = (\rho T)_{N-1}$, allowing an error of the first order in Δr. Obviously, a small change of pressure at the wall would have little effect on the system as a whole.

Using similar arguments, the necessary boundary conditions of the fluid velocities which appear in the parabolic equations (6), can be determined as

$$\begin{aligned} (U_r, U_\theta, U_\phi)_N &= (U_r, U_\theta, U_\phi)_{N-1}, \\ (U_{er}, U_{e\theta}, U_{e\phi})_N &= (U_{er}, U_{e\theta}, U_{e\phi})_{N-1} . \end{aligned} \tag{17}$$

3.2.B. Boundary Conditions at the Wall

Many of the boundary conditions at the wall for the basic equations (6 and 7) are already determined in the previous section. The only remaining boundary conditions to be determined are the ones for ψ , χ and T for the parabolic equations (6).

For the temperature equation, the boundary value of the temperature T_w, is set at a constant which is typically 1∿10 ev depending on preionization. The condition $T_w = T_{w-1}$, can also be used if an adiabatic wall is assumed.

The wall values of ψ and χ are both pure functions of time. Let I_θ be the total external poloidal current passing through the hole of the torus (cf. Fig. 1). Then, from Ampere's law,

$$\chi_w(t) = 2I_\theta(t)/c \quad . \qquad (18)$$

Since the function $I_\theta(t)$ is readily measurable and programmable in the experiment, the boundary value $\chi_w(t)$ is well determined by this equation.

Due to the assumption of perfect conductivity for the outer shell, ($B_n = 0$), ψ is a constant at the wall at a given time. This boundary value ψ_w is proportional to the total magnetic flux through the hole of the torus (or to the volt-seconds around the torus). The flux in the hole is the algebraic sum of the primary transformer flux and the flux induced by the

plasma current and the current on the outer shell. Therefore in general, $\psi_w(t)$ is a complicated function of time. For example, it will depend on the plasma motion, imploding or expanding, and the plasma position. Hence, it is very difficult to predict or program $\psi_w(t)$ in the experiment. On the other hand, the total toroidal plasm current $I_{\phi p}(t)$ (which is a sufficient boundary condition for an infinite aspect ratio case, but cannot be used directly as a boundary condition in our two dimensional case of a finite aspect ratio torus), is readily measurable and programmable in experiment. Therefore, for the simulation of given experiments, we use $\psi_w(t)$ as a boundary condition in such a way that the resulting total plasma current $I_{\phi p}(t)$ matches the experimental measurements. The value of $\psi_w(t)$ is adjusted at each time step to give this result. This is done by extrapolating the ratio of the increaments of ψ_w and $I_{\phi p}$ at the previous time step to the new time step values.

The reason for the previously stated fact that $I_{\phi p}(t)$ is a simple function of time without much dependence on the plasma motion or position, and also that it is easily predictable and programmable, will be found in the next section where the relationship between $\psi_w(t)$ and $I_{\phi p}(t)$ is explained.

3.2.C. Flux in the Hole and the Total Toroidal Plasma Current

In this section, we study the relation between flux in the hole of the torus and total plasma current to explane further the necessity of adopting the latter as an effective boundary condition. It is noted here that all the equations derived in this section except equation(22) are not actually used in our calculation since the circuit equation is not incorporated. However in cases where the incorporation of the circuit equation become necessary,this could be easily done using the equations in this section.

The magnetic flux in the hole of the torus, $F_w = 2\pi\psi_w$, can be expressed as a linear function of the external toroidal circuit current $I_{\phi ex}$ and the total toroidal plasma current $I_{\phi p}$, with constant coefficients M and L which are determined by the physical geometry of the system alone,* independent of plasma motion or position, i.e.,

$$F_w = MI_{\phi ex} + LI_{\phi p} , \qquad (19)$$

with constant coefficients M and L.

---

* B_θ and B_r outside the torus (div $\underline{B}$ = 0 and curl $\underline{B}$ = 0) at a given time, are determined by the unique solution of a problem posed by given values of $I_{\phi ex}$ and $I_{\phi p}$ and the boundary condition $B_n = 0$ on the outer surface of the shell. This solution is in turn, a superposition of the two solutions, one posed by a given value of $I_{\phi ex}$, $I_{\phi p} = 0$ and $B_n = 0$ on the shell, and the other by $I_{\phi ex}=0$, a given value of $I_{\phi p}$ and $B_n=0$ on the shell. These two solutions are each linear in $I_{\phi ex}$ and $I_{\phi p}$, respectively. Therefore, equation(19) results, with constant coefficients M and L. The linearity of the magnetic medium outside the torus is assumed, in this proof.

For a sufficiently well conducting plasma (more quantitatively) $R \ll \omega L/c$ where ω is the characteristic frequency of the system, R the effective total toroidal resistivity of the plasma and c the light speed), the left side of equation (19), i.e., the flux F_w will be negligible compared to the terms on the right side, during the time before the crowbar time $t_{cb} \sim 1/\omega$. (The procedure after the crowbar time will be explained later in this section.) This can be readily seen by noting that the flux F_w is†

$$F_w \sim \int_0^t cR\, I_{\phi p}\, dt, \quad \text{where } t < t_{cb}.$$

Therefore, we obtain equation (19),

$$I_{\phi p} \simeq -\frac{M}{L} I_{\phi ex} \quad . \tag{20}$$

Applying similar reasoning to the external circuit, we find that the external current $I_{\phi ex}$ can be evaluated by introducing simple equivalent circuit equations whose effective inductance is a constant L_{eff} given by

$$L_{eff} = L_{ex} - \frac{M^2}{L} \quad , \tag{21}$$

where L_{ex} is the self-inductance of the external primary loop circuit.

---

† Here, it is also assumed that the gap between the conducting wall and the surface of the plasma column is small compared to the major radius of the torus.

The external current $I_{\phi ex}$ found in this way, determines the plasma current $I_{\phi p}$ by equation (20). Therefore, the plasma current $I_{\phi p}$ has little dependence on the plasma parameters such as its motion or position, and is easily programmable in the experiment. Of course, the actual measurement of the plasma current $I_{\phi p}$ shows some residual oscillations which represent mainly the coupling effect to the plasma implosion or expansion phase due to finite conductivity of the plasma.

We note here that even though the two terms on the right side of equation (19), i.e., $I_{\phi ex}$ and $I_{\phi p}$ term, are programmable functions, the sum of these two functions, i.e., F_w $(=2\pi\psi_w)$ is not. This is not a contradiction, because F_w is represented as a sum of two big quantities with opposite signs, which becomes zero in the case of a perfectly conducting plasma.

We also note that using equation (19) (which is not an approximation but an exact equation), the circuit equations can be easily incorporated into the problem and solved simultaneously with the plasma equations, even in the present two dimensional case. Although this procedure would somewhat improve the accuracy of the solution, the difference would not be important in view of our rather crude modeling of the plasma.

Until now, we have been concerned with the boundary condition ψ_w before the crowbar time. After the crowbar time, the method of following the plasma current by adjusting ψ_w

is also used in the case of the power crowbar, with $I_{\phi p}(t)$ = constant. Or, if the experiment is crowbarred directly on the torus shell without power crowbar, as in some of ZT-S discharges, $\psi_w(t)$ is given by

$$\Delta\psi_w = \mathcal{L}\,\Delta I_{\phi p} \quad , \tag{22}$$

after the crowbar, where $\mathcal{L}$ is a constant representing the flux in between the outer shell and the discharge tube wall, which is approximately proportional to the plasma current.

3.2.D. Boundary Condtions for the θ Direction and Computational Mesh Scheme

In general, the boundary condition for the θ direction will be simply a periodic boundary condition from the fact that $f(\theta + 2\pi) = f(\theta)$ for any variable f. However, to save computer time, we used the symmetry condition against the horizontal mid-plane of the torus. Therefore, only those toroidally symmetric instabilities which are also symmetric against the mid-plane, if any, will appear in our calculation.

It is easy to see that the following symmetry conditions against the mid-plane satisfy equations (6) and (7).

Even symmetry: ψ, χ, T

$$B_\theta, \; B_\phi, \; j_\theta, \; j_\phi, \; \rho, \; U_r, \tag{24}$$

Odd symmetry: B_r, j_r, U_θ, U_ϕ .

Fig. 4 shows the computational mesh scheme used. We use polar meshes with constant Δr and $\Delta\theta$, which cover the upper half of the torus cross section with additional $\Delta\theta$ at each side (i.e., $j = 1$ and $j = j_{max}$). In this mesh scheme, the symmetry condition (24) determines the boundary conditions for the θ direction as

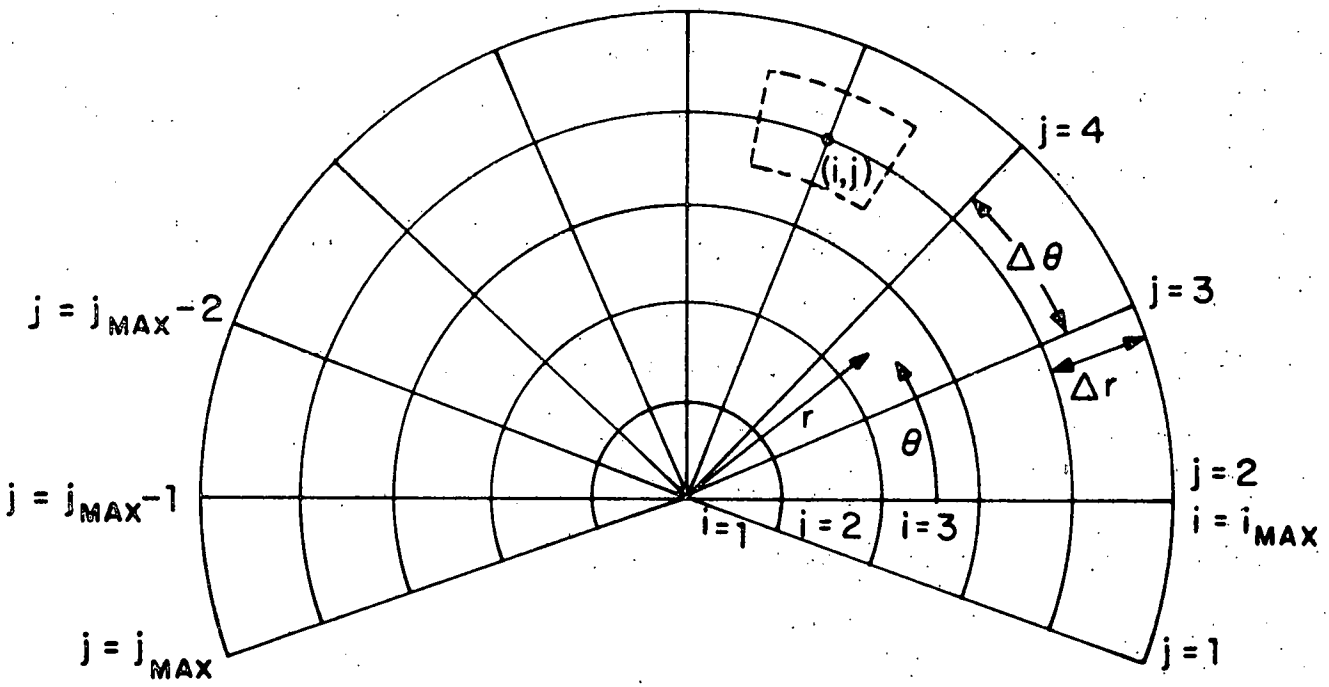

FIG. 4. SCHEMATIC DIAGRAM OF THE COMPUTATIONAL MESHES

$$\left.\begin{aligned} f_{i,1} &= \pm f_{i,3} \\ f_{i,j_{max}} &= \pm f_{i,j_{max-2}} \end{aligned}\right\} \quad \begin{aligned} &+ \text{ for the variables of even symmetry,} \\ &- \text{ for the variables of odd symmetry.} \end{aligned} \tag{25}$$

3.2.E. Treatment of the Coordinate Origin

Although the coordinate origin r = 0 is an interior point of the plasma, it is a boundary point of the coordinate system (r,θ,ϕ). Therefore, appropriate treatment of the origin is necessary. We will describe two separate methods for the treatment of the coordinate origin. The first method is simple and easy to use but good only for a relatively gentle process (e.g., a low pinch ratio discharge). The other method is rather complicated to use but found to be satisfactory in general.

The first method exploits the fact that the value of $\underline{W} = (\rho, \rho U_r, \rho U_\theta, \rho U_\phi)$ at the origin does not appear in the solution procedure, if we adopt the following difference scheme of the r derivation, i.e.,

$$\frac{1}{r}\frac{\partial rf}{\partial r} \rightarrow \frac{1}{r_i}\frac{(rf)_{i+1} - (rf)_{i-1}}{2\Delta r}, \qquad (26)$$

where f is any function of $\underline{W}$. All the terms which require boundary values of $\underline{W}$ in the equations (6) and (7) can be naturally represented in this way.

Among the remaining boundary values for the variables T, ψ, χ, the boundary value T_o^{n+1} of the variable T at the next time step $t = (n+1)\Delta t$, can be given simply as the average value of the old time step value $T^n_{i=2,j}$ of the grid points at $r = \Delta r$ (see Fig. 4), i.e.,

$$T_o^{n+1} = \frac{1}{N}\sum_{j=1}^{N} T^n_{i=2,j} \qquad (27)$$

where $N = \frac{2\pi}{\Delta\theta}$, and the values at $j > j_{max}$ are found from the symmetry condition (25).

The boundary value χ_o^{n+1} is found by applying Faraday's law on the center grid (the region $r < \Delta r$), i.e.,

$$\frac{(\Delta\chi_o)^n}{\Delta t} = \frac{R_o(\Delta B_\phi)_o}{\Delta t} = \frac{R_o c}{\pi(\Delta r)^2} \sum_{j=1}^{N} (E_\theta)^n_{i=2,j} \Delta r \, \Delta\theta ,$$

$$(E_\theta = \frac{j_\theta}{\sigma} + \frac{1}{c}(U_\phi B_r - U_r B_\phi)), \qquad (28)$$

$$\chi_o^{n+1} = \chi_o^n + (\Delta\chi_o)^n .$$

The boundary value ψ_o^{n+1} is determined from $(E_\phi^n)_o$ which is set at the average value of $(E_\phi^n)_{i=1,j}$ at $r = \Delta r$, i.e.,

$$(E_\phi)^n_o = \frac{1}{N} \sum_{j=1}^{N} (E_\phi)^n_{i=1,j},$$

$$-\frac{1}{cR_o} \frac{(\Delta\psi_o)^n}{\Delta t} = (E_\phi)^n_o , \qquad (29)$$

$$\psi_o^{n+1} = \psi_o^n + (\Delta\psi_o)^n .$$

This simple method just described, is found satisfactory when the plasma behavior is rather gentle. But when the plasma behavior is more violent (e.g., for high pinch ratio discharge),

the $\underline{W}$ values tend to oscillate near the origin and the calculation tends to break down.

This instability is probably due to the fact that the difference scheme (26) does not conserve mass and momentum near the origin. For example, the mass flow $\frac{(r\rho U_r)_{i=2}}{2}$ through the circle $r = \frac{1}{2}\Delta r$ is lost, since the value $\rho_{i=1}$ at the origin does not appear in the equation. (cf. Section 3.2.A). Although the resulting error in the total is rather small due to small size of the cells near the origin, this error can result in a severe numerical strain in these small cells. Therefore, the following more elaborate treatment of the origin, which conserves mass and momentum near the origin, is adopted, and it is found satisfactory for any cases treated thus far.

Instead of the difference scheme (26), we use the following scheme for the r derivatives, i.e.,

$$\frac{1}{r}\frac{\partial rf}{\partial r} = \frac{f}{r} + \frac{\partial f}{\partial r} \rightarrow \frac{\frac{1}{2}f_i + \frac{1}{4}(f_{i+1}+f_{i-1})}{r_i} + \frac{f_{i+1}-f_{i-1}}{2\Delta r} \quad (30)$$

In cylindrical coordinates (r, θ), using a similar argument as in Section (3.2.A), we find that the total mass change in the grid (i,j) due to the U_r term $\frac{1}{r}\frac{\partial}{\partial r}(r\rho U_r)$ is

$$
\begin{aligned}
(\Delta M)_{ij} &= \Delta\rho\Delta r r\Delta\theta \\
&= -\left(r_i\Delta\theta + \frac{\Delta r\Delta\theta}{2}\right)\left(\frac{\rho U r_{i+1} + \rho U r_i}{2}\right)\Delta t \\
&\quad + \left(r_i\Delta\theta - \frac{\Delta r\Delta\theta}{2}\right)\left(\frac{\rho U r_{i+1} + \rho U r_{i-1}}{2}\right)\Delta t \\
&= -r_{i+\frac{1}{2}}\,\Delta\theta\,(\rho U_r)_{i+\frac{1}{2}}\,\Delta t \\
&\quad + r_{i-\frac{1}{2}}\,\Delta\theta\,(\rho U_r)_{i-\frac{1}{2}}\,\Delta t \qquad (31)
\end{aligned}
$$

Therefore, the difference scheme (30) conserves mass. The mass flux density through a point $i+\frac{1}{2}$ is defined as*

$$\frac{(\rho U_r)_i + (\rho U_r)_{i+1}}{2} .$$

The definition of the moemntum flux density can also be found in a similar way (e.g., for the θ component, as $\frac{(\rho U_\theta U_r)_i + (\rho U_\theta U_r)_{i+1}}{2}$). Using these definitions, we determine the boundary value $\underline{W}_o$ at the origin (i=1) such that total mass and momentum are conserved.

For the value ρ_o, we apply the mass conservation equation

$$\frac{d}{dt}\int\rho dV = \int\rho\underline{U}\cdot d\underline{s}$$

on the region $r \leq r/2$, and find

---

* The difference between this and definition (15) in Section (3.2.A), is due to the different r direction difference schemes used, and results in a minor change in the boundary conditions at the wall. (The boundary conditions for the present scheme are $(\underline{W}U_r)_N = -(\underline{W}U_r)_{N-1}$, compared to the condition (16), i.e., $(r\underline{W}U_r)_N = -(r\underline{W}U_r)_{N-1}$, for the previous difference scheme (11).) But near the origin, these two defintions give quite different results.

$$\frac{\Delta\rho}{\Delta t} = \frac{-4}{N\Delta r} \sum_{j=1}^{N} (\rho U_r)_{i=\frac{3}{2}} S_j,$$

where $(\rho U_r)_{i=\frac{3}{2}} = ((\rho U_r)_{i=1} + (\rho U_r)_{i=2})/2$, and $S_j = 1 + \frac{\Delta r}{2R_o} \cos\theta_j$ appearing due to the toroidal curvature.

For the momentum values at the origin, the momentum equation

$$\frac{\partial}{\partial t}\int \rho \underline{U} dv = -\int (\rho \underline{U}(\underline{U} \cdot d\underline{s}) + p \cdot d\underline{s}) + \frac{1}{c}\int (j \times B) dv$$

is appled in an infinitesimal sector (since $\underline{U}$ is a vector), $r \leq \frac{\Delta r}{2}$ and $\phi_c \leq \phi \leq \phi_c + d\phi$. This is calculated first in (R,Z,ϕ) coordinates (cf. Fig. 1) which are uniquely defined at the origin, unlike (r,θ,ϕ) coordinates. From the symmetry condition (24), we readily find that U_Z and U_ϕ are zero at the origin. The nonzero R component ρU_R is found as

$$\frac{\Delta(\rho U_R)_o}{\Delta t} = -\frac{4}{N\Delta r} \sum_{j=1}^{N} ((\rho U_R U_r)_{i=\frac{3}{2},j} S_j + P_{i=\frac{3}{2},j} \cos\theta_j) + \frac{1}{c}(\underline{j}_o \times \underline{B}_o)_R, \qquad (33)$$

where

$$(\rho U_R U_r)_{i=\frac{3}{2},j} = (\rho U_r U_r \cos\theta - \rho U_\theta U_r \sin\theta)_{i=\frac{3}{2},j},$$

$$\left.\begin{aligned} (\rho U_r U_r)_{i=\frac{3}{2},j} &= \tfrac{1}{2}\{(\rho U_r U_r)_{i=1,j} + (\rho U_r U_r)_{i=2,j}\}, \\ (\rho U_\theta U_r)_{i=\frac{3}{2},j} &= \tfrac{1}{2}\{(\rho U_\theta U_r)_{i=1,j} + (\rho U_\theta U_r)_{i=2,j}\} \end{aligned}\right\},$$

$$P_{i=\frac{3}{2},j} = \tfrac{1}{2}(\gamma-1)((\rho T)_{i=2,j} + (\rho T)_{i=1,j}),$$

and the values $\underline{j}_o$ and $\underline{B}_o$ at the origin will be found later in this section. Then, the values $(\rho U_r)_{i=1,j}$ and $(\rho U_\theta)_{i=1,j}$ at the origin are found from the value $(\rho U_R)_{i=1}$ given above. Since in general for a vector $\underline{V} = V_R\hat{R} + V_Z\hat{Z} + V_\phi\hat{\phi}$,

$$(V_r)_{i=1,j} = (V_R)_{i=1}\cos\theta_j + (V_Z)_{i=1}\sin\theta_j \quad ,$$

$$(V_\theta)_{i=1,j} = -(V_R)_{i=1}\sin\theta_j + (V_Z)_{i=1}\cos\theta_j \quad ,$$

we find

$$(\rho U_r)_{i=1,j} = (\rho U_R)_{i=1}\cos\theta_j \quad , \tag{34}$$

$$(\rho U_\theta)_{i=1,j} = -(\rho U_R)_{i=1}\sin\theta_j \quad .$$

For the temperature T_o at the origin, we simply average $T_{i=2,j}$ as the previous method (27) instead of using the energy conservation. This is for simplicity, because the temperature equation is not written in a conservative form so that incorporating the exact energy conservation would be complicated. Also, the value T_o will not much affect the overall stability, due to the large conduction term in the temperature equation.

The boundary value χ_o is found exactly the same as in the previous method (Eq. 28). The value ψ_o is also found in a similar way as in the previous method (Eq. 29), except this time the value $(E_\phi)_o^n$ is found directly from $E_{\phi o} = \frac{j_{\phi o}}{\sigma_o} + \frac{1}{c}$ $(U_{r_o}B_{\theta o} - U_{\theta o}B_{r_o})$ without the averaging step.

The boundary values $\underline{j}_o$ and $\underline{B}_o$ are found using Maxwell's equations in (R,Z,ϕ) coordinates and then transforming them into (r,θ,ϕ) coordinates in the same way as the procedure for the value $\rho\underline{U}_o$. The values in (R,Z,ϕ) coordinates are

$$
\begin{aligned}
j_{R_o} &= 0, \\
j_{Z_o} &= -\frac{c}{2\pi R_o N\Delta r} \sum_{j=1}^{N} \chi_{i=2,j} \cos\theta_j, \\
j_{\phi o} &= \frac{c}{2\pi N\Delta r} \sum_{j=1}^{N} (B_\theta)_{i=2,j}, \qquad (35) \\
B_{Ro} &= 0 \\
B_{Z_o} &= -\frac{2}{R_o N\Delta r} \sum_{j=1}^{N} \psi_{i=2,j} \cos\theta_j, \\
B_{\phi o} &= \frac{\chi_o}{R_o} \quad .
\end{aligned}
$$

3.3 Treatment of the Low Density Region

When the plasma pinches inward, the density near the wall drops quickly resulting in a very low density plasma region (or maybe a vacuum) outside the main pinched plasma column. Treatment of this low density region has been one of the major difficulties since the early work of Hain et al.[28]

It is debatable whether we should treat this region as a true vacuum or as a very low density plasma. Even if the mathematical model (i.e., the dissipative MHD model, in the present case) indicate this region to be a vacuum, the actual situation in the experiment may be quite different, e.g., due to turbulent diffusion, emission from the wall, etc. Aside from this fact, even mathematically, the answer is not clear. If a Lagrangian difference scheme is used, the plasma boundary will part from the wall and create a vacuum region. But this may not represent a correct picture even if a smooth exact solution exists with density $\rho \to 0$ in the outer region, because the conductivity σ can be still finite. Moreover, the exact solution of the differential equation may possess singularities in it,[27] which are removed by the finite spacing of the Lagrangian scheme.

Often, there is some advantage in assuming the outer region to be a vacuum, because the numerical calculation of the low density plasma possesses difficulties which will be discussed later. Although it is very difficult to incorporate

the vacuum region in our two dimensional calculation due to the complexity of the vacuum-plasma boundary, it is easily done in one dimensional ($\frac{\partial}{\partial \phi} = 0$, $\frac{\partial}{\partial \theta} = 0$) calculation with a Lagrangian scheme or even a Eulerian scheme. Therefore, we tested this idea using a one dimensional Eulerian code and found that the comparison between the calculation and the experimental results was not satisfactory. This large discrepancy is not surprising because the partial shielding of the applied fields by the low density region plasma is totally neglected. This effect is more important in our case of a circular cross section torus due to the large cross sectional area of the low density region.

To solve the problem incorporating the low density region plasma, it is necessary to devise a method to go around the numerical difficulties due to a high Alfven speed. Since the plasma density is very low and the magnetic field is strong in the low density region, the Courant condtion for stability requires prohibitively small time step for an explicit difference scheme. One thus improves this situation by using an implicit scheme as Hain et al.,[28] or by substituting an artifical signal speed for the speed of light as Boris[29]. These methods will extend the solvable range of the density ρ, but of course, there is a limit for this range because of nonlinear instabilities or inaccuracy of the solution, etc. Therefore, it seems that one must also use a procedure which keeps the density from falling below a fixed floor value, rather than simulate the real low density in this region.

Hain et al.[28] assumed the low density plasma to be created continuously at the wall to maintain the plasma density above a floor value. For some experimental parameters, however, this is not enough. Therefore the injection of plasma at individual cells when the density falls below a floor value may be necessary as in Lui and Chu.[1] Although these procedures can be thought of as analogies of the ionization process, these methods produce largely artificial effects such as artificial increase of the mass, momentum and energy. These artificial effects become severe when the calculation is run for a long time as in our calculation. Lindemuth[30] assumes the wall to be a gate which opens when the plasma pinches inward, remains open to let the plasma flow out when the plasma expands outward, and then closes when the total mass of the plasma returns to the original value. This procedure would somewhat improve the situation in the direction of the mass conservation. But for example, at the end of the first pinching, the artificial mass increase will be the same as the previous method. To conserve the total mass, some codes prevent the mass flow by setting the fluid velocity to zero when the density drops below a floor value. But in this method, the plasma in the low density region will see the whole electric field such that the current flow ($\underline{j} = \sigma \underline{E}$ with $\underline{U} = 0$) will be artificially high, especially when the crowbar is not yet applied. In spite of this error, we found this method useful for its good stability character, but only in limited cases when a small region of low density plasma is created until the crowbar time.

The method we use is modified but similar to the ones used by Hain et al.[28] and Lui and Chu[1], with a floor value of $\sim 5\%$. To correct the artificial increase of the mass and momentum, we adopt the following procedure. The main idea of this procedure is that we picture the low density region as a very tenuous plasma of finite conductivity, and also that the flow of the plasma mass and momentum from the low density region into the main plasma column is negligible due to the negligible density of the outer region.

1) Define the low density region-main plasma column boundary. Most of the time, this boundary is well defined and easy to find, because there is a sharp density increase at this boundary.

2) Subtract the mass and momentum flow into the main plasma column from the low density region, at each time step. For this procedure, we use the definition of the mass and momentum flow given in Section (3.2.A). We will explain this step using a one-dimensional analogy (Figure 3 on page). When the flow is inward to the main plasma column, the artificial increase of the mass and momentum at the first cell (cell M) in the main plasma column, is subtracted, i.e.,

$$\rho_M^{new} = \rho_M + \frac{\Delta t}{2\Delta x} \left((\rho u)_{M+1} + (\rho u)_M \right),$$

$$(\rho u)_M^{new} = (\rho u)_M + \frac{\Delta t}{2\Delta x} \left((\rho u u)_{M+1} + (\rho u u)_M \right) \qquad (36)$$

when the flow is inward (i.e., $(\rho u)_{M+1} + (\rho u)_M < 0$). Here, the point $M + \frac{1}{2}$ corresponds to the low density - main plasma boundary.

When the flow is outward to the low density region (i.e., $(\rho u)_{M+1} + (\rho u)_M > 0$), a detailed adjustment can be made to ensure the conservation of the total mass. But this procedure can be usually omitted, because the difference resulting from this procedure is small, due to the fact that the plasma outflow from the main plasma column usually dominates the flow in the low density region. Nevertheless, if a certain situation demands, this procedure can be derived in an analogous way as the inward flow case, except that this time, the boundary cell (cell L) in the low density region which makes contact with the main plasma column, should be treated as a cell inside the main plasma, thereby inducing an outward movement of the low density - main plasma boundary.

We note that no correction is made to the flow of energy, because the thermal energy is the least accurate variable in our calculation (cf. Section (2.3)).

IV. RESULTS OF THE SIMULATION

In this chapter, we present the calculated results of SP-1 screw pinch and ZT-I, ZT-S and ZT-40 reverse-field pinch experiments. (For the description of the experiments, see chapter I.) The calculated results are compared to the experimental values when they are available.

Typical operating parameters in various reverse field pinches are compared in table 1. The starred items have been simulated with the present code. The four devices on the upper columns, including ZT-S, are currently operating experiments. They are similarly on a quite low parameter range. The next three larger devices, including ZT-40, are either on a planning or construction stage. The scaling character of the pinch discharges is the crucial question to be investigated by these larger devices. Each of these devices is envisioned as an intermediate step for the next even larger experiment which would reach $n\tau \sim 10^{14}$ sec $\cdot$ cm^{-3} range. The old ZETA parameters and the ZT-I which was the previous version of ZT-S, and also the SP-1 screw pinch parameters are shown on the last columns for comparison.

Since the three experiments, SP-1, ZT-I and ZT-S are on a similar parameter range, discussions made for one experiment would similarly apply to the others, most of the time. Therefore, according to the availability of the

TABLE 1

Typical Operating Parameters in Various Reverse-Field Pinches

	Minor Rad.	Major Rad.	Filling Gas	Lifetime	Temperature	Location
HBTX-I	6.5cm	100cm	$\sim 2\times10^{15}cm^{-3}D_2$	$\sim$15μs	$\sim$50ev	Culham
* ETA-BETA	5	40	$\sim 10^{15}H_2$	$\sim$15	$\sim$10	Padua
ETL-TPE-1	5	40	$\sim 2\times10^{15}$	$\sim$20	$\sim$20	Tokyo
* ZT-S	7.7	40	$\sim 2\times10^{15}D_2$	$\sim$30	$\sim$20	LASL
HBTX-II	60	180	$\sim 10^{14}$	$\sim$10,000	$\sim$300	Culham
ETA-BETA-II	24					Padua
* ZT-40	20	114	$\sim 2\times10^{15}$	$\sim$200	$\sim$200	LASL
ZETA	50	150	$\sim 10^{14}$	$\sim$10,000	$\sim$200	Harwell
* ZT-I	5.2	38	$\sim 2\times10^{15}D_2$	$\sim$15	$\sim$10	LASL
* SP-1 Screw Pinch	6	36	$\sim 2\times10^{15}H_2$	$\sim$10	$\sim$20	Jutphaas

experimental data, a different emphasis is given on the discussion of each experiment. The gross motion of the plasma and its approach to the quasi-equilibrium dissipation state are discussed in detail for the SP-1 simulation (Section 4.1). The comparison between the given anomalous resistivity algorithm and the classical resistivity is emphasized in the discussion of the ZT-I results (Section 4.2). This comparison is extended to a much longer time through the dissipation phase for the ZT-S experiment (Section 4.3.A). The effects of toroidal curvature, i.e., toroidal shift, toroidal plasma flow, etc., are discussed at length in Section (4.3.B).

For the larger ZT-40 experiment, the effects due to a bigger machine size are studied. For this, we first study the scaling law of the dissipative magnetohydrodynamic equations (Section 4.4.A). Finally, in the last section, we discuss some confinement characteristics of large pinch machines.

4.1 SP-1 Screw Pinch

The SP-1 toroidal screw pinch[31] at Jutphaas has a major radius of 36cm and a minor radius of 6cm. We will present the simulation results of a discharge with $n_0 = 4 \times 10^{-9}$ gm/cm^3 hydrogen filling gas, initial temperature of 1 ev and a toroidal bias field of +100G. Figure 5 shows the time traces of the toroidal magnetic field applied at the wall and the total toroidal plasma current. Although,

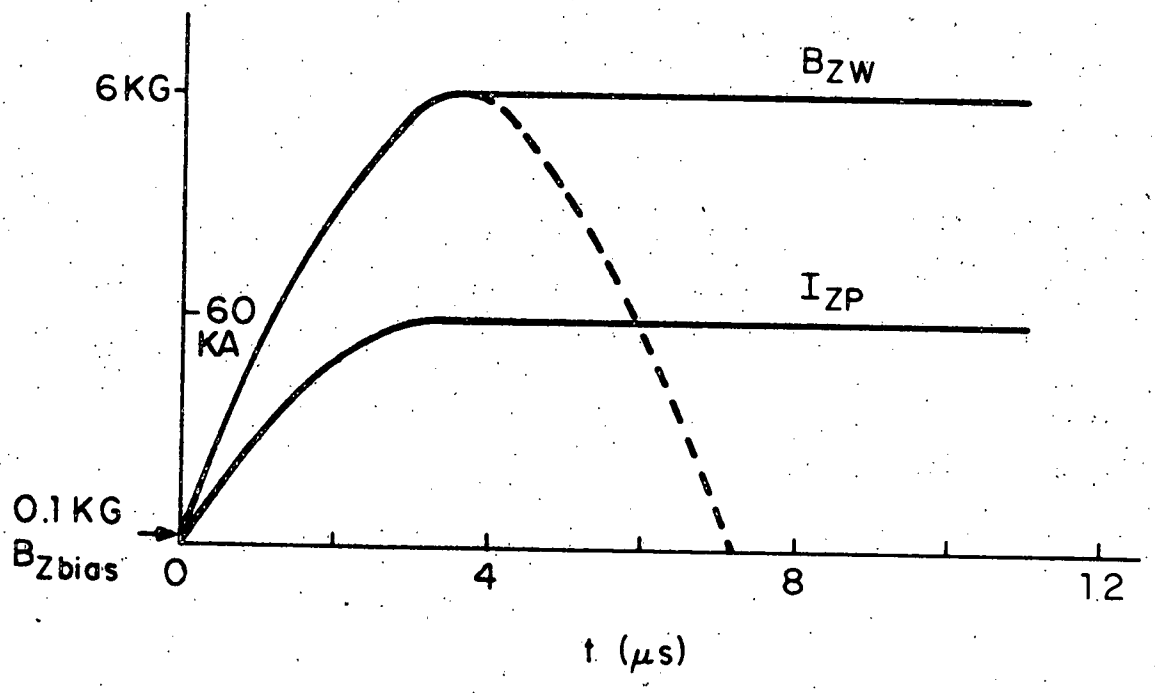

FIG. 5. TIME TRACES OF THE TOROIDAL MAGNETIC FIELD B_{zw} AT THE WALL AND THE TOTAL TOROIDAL PLASMA CURRENT I_{zp}. THE DASHED LINE INDICATES THAT THE DISCHARGE IS NOT CROWBARRED IN THE EXPERIMENT.

in the experiment, the discharge is allowed to ring as indicated by the dashed experimental curve, we effectively crowbarred the discharge at 3.6μs in our simulation to study the transition toward a quasi-equilibrium dissipation state. The following results are obtained using the classical resistivity formula. The Chodura anomalous resistivity formula described in Section (2.3) gives essentially the same results until the crowbar time. A detailed comparison between the classical resistivity and the anomalous algorithm is made in the following two sections on ZT-I and ZT-S results.

Figure 6 shows the toroidal field at the center of the poloidal plane as a function of time. The toroidal field at the wall is also shown for a comparison. The solid curve represents the calculated results and the dashed curve the experimental results which is measured only until the crowbar time (3.6μs). This figure shows at once the pinching and bouncing motions of the plasma being damped due to the dissipation mechanisms and reaching a quiet phase which will be shown later to be a quasi-equilibrium dissipation state. Therefore, the present simulation is successful in that we could follow the plasma behavior through the pinching and bouncing motions all the way to the quasi-equilibrium state. The previous simulation of this same discharge could follow the plasma behavior until about 2.5μs, but it broke down due to a numerical instability. A careful treatment of the boundary conditions is found to be mainly responsible for

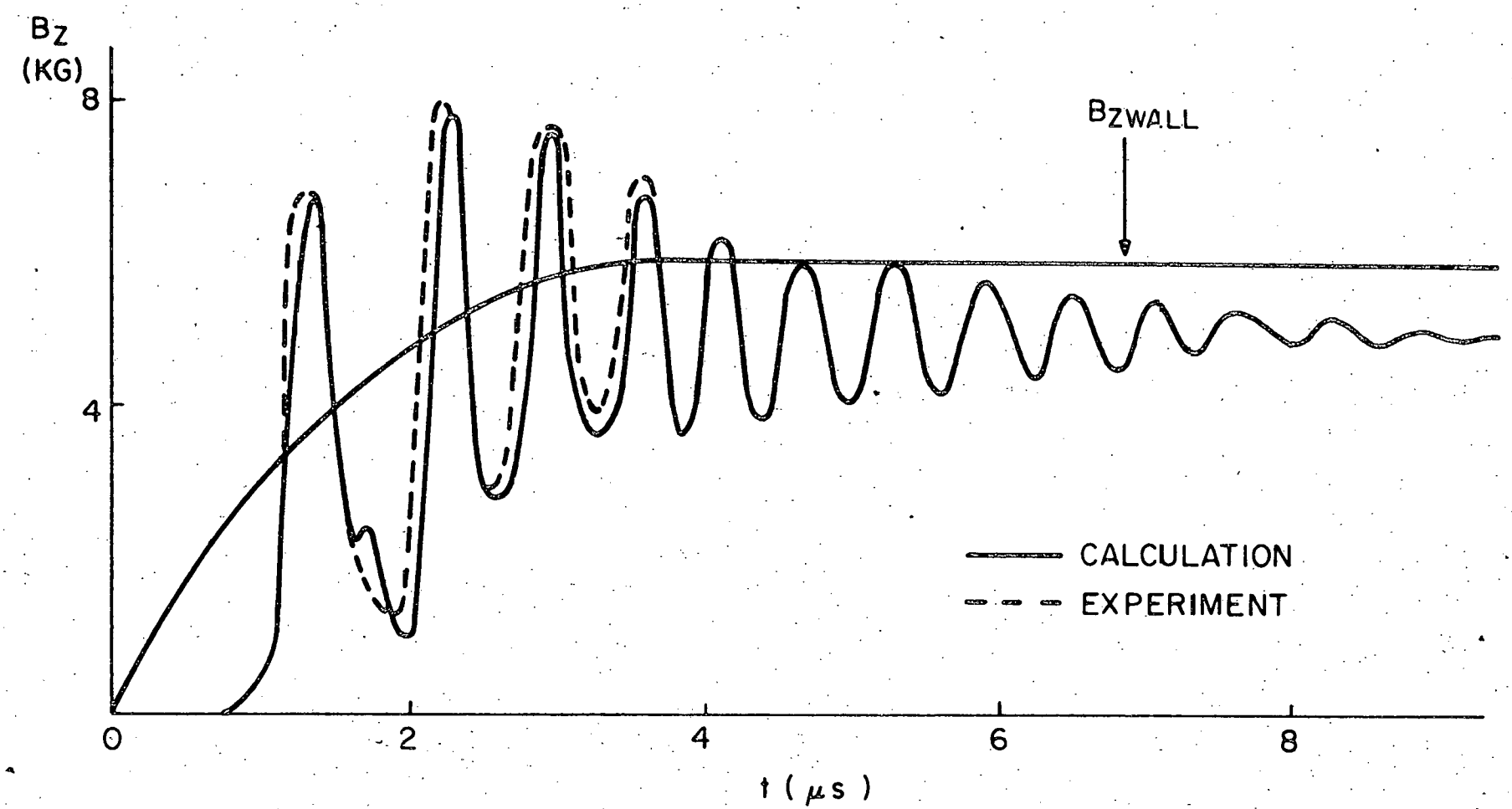

FIG. 6. TIME TRACE OF THE TOROIDAL FIELD AT THE MINOR AXIS.

THE TOROIDAL FIELD AT THE WALL IS ALSO SHOWN.

this successful simulation. The very close agreement between the calculation and the experiment shown in Figure 6 is somewhat optimistic. As we will see later in this chapter, all the simulation results show good agreement with the experiment, but not in general as close as this result.

In Figure 7, the profiles of the density and temperature on the horizontal diameter ($Z = 0$) of the poloidal plane are shown at various instants of time during the initial two bounces. The density profile at 1.8μs corresponds to the maximum outward expansion after the first pinching, and it shows that the main plasma column stays well away from the wall. Both the density and the temperature are higher on the inside of the torus since the magnetic field and the current density are stronger inside. A toroidal shift of ∿1cm is seen at 2.2μs. Since the pinching time is much shorter than the heat diffusion time (which will be discussed later), the compressional heating is clearly seen.

After several more successively smaller bounces, the density profile reaches a nearly stationary state as shown in the next figure. Figure 8 shows the density and temperature profiles at 6, 7, and 8μs. The bouncing motion is largely damped away and the toroidal shift motion of the plasma column seems to be the dominant movement. This toroidal shift motion is found to be oscillatory as shown in the next figure.

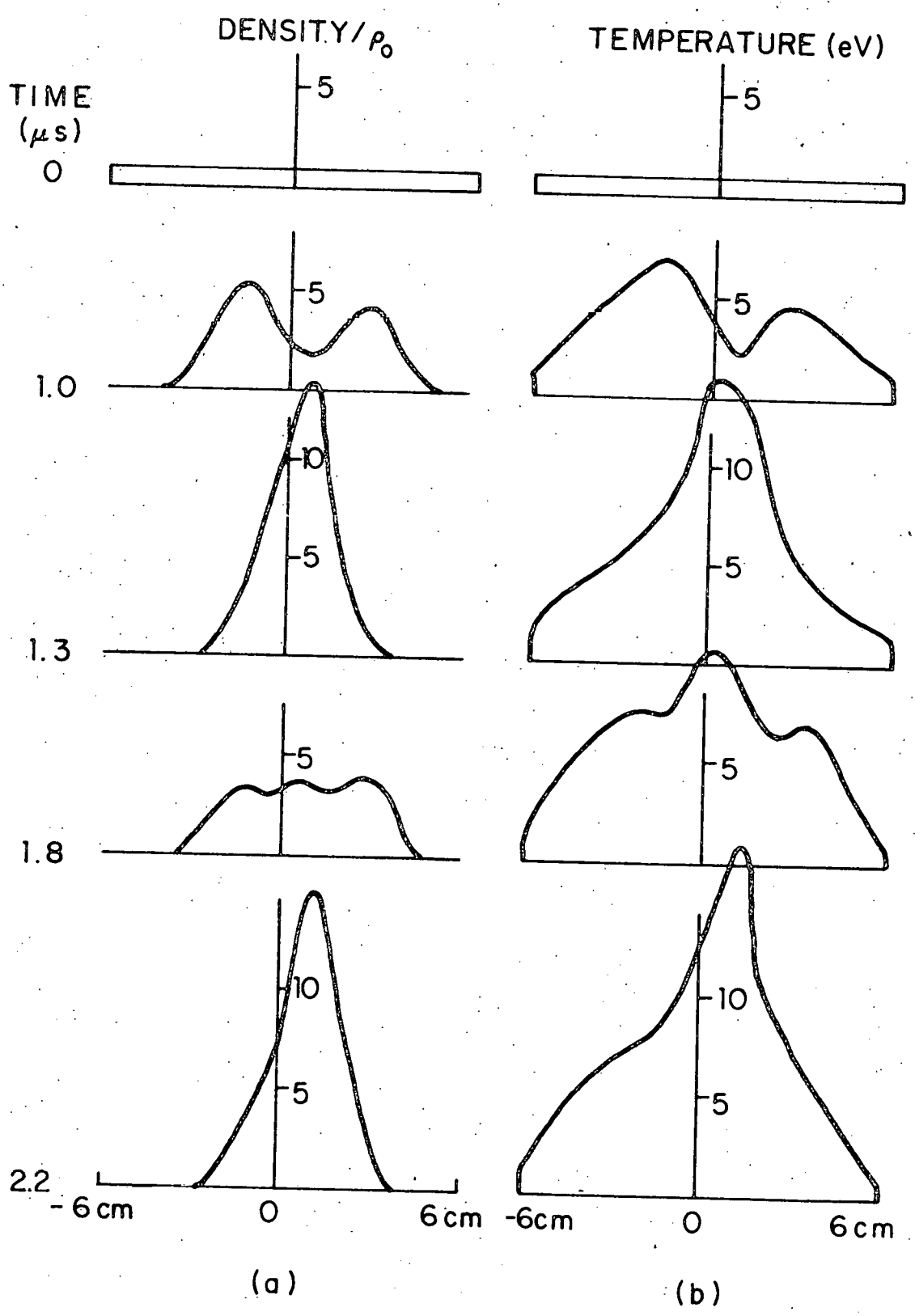

FIG. 7. PROFILES OF THE DENSITY AND THE TEMPERATURE ON THE HORIZONTAL DIAMETER OF THE POLOIDAL PLANE.

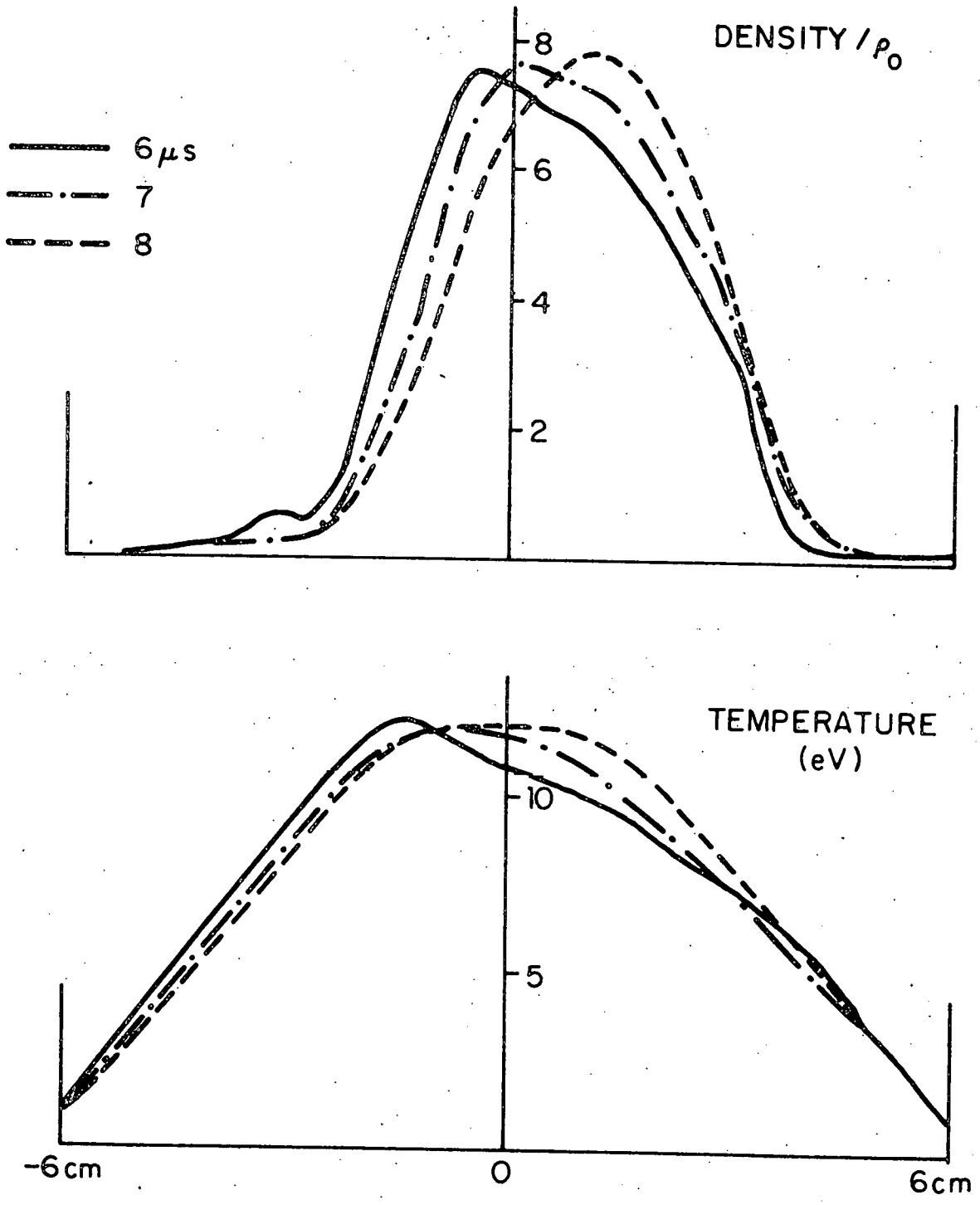

FIG. 8. DENSITY AND TEMPERATURE PROFILES AT 6, 7 and 8 μs.

In Figure 9, the dotted curve represents the time trace of the magnetic axis, and the two semi-broken curves represent the time traces of the positions of the two density peaks. The major axis is on the lower side. The traces of the density peaks show the pinching and bouncing motions of the plasma. This bouncing motion is mostly damped away at about 5μs and the density peak subsequently follows closely the trace of the magnetic axis. The motion of the toroidal shift shows a damped oscillation with a period of ∿5μs and a dissipation time of ∿10μs. The equilibrium position of this toroidal shift is ∿1.2cm which compares with the experimental measurement of ∿1.5cm.

The time scales of these oscillations and the damping process can be understood from the basic time scales (cf. Section (4.4.A)) of this diffuse pinch discharge. The Alfven time scale $\tau_A = r^o\sqrt{4\pi\rho^o}/B^o$ (the superscript ^{o} denotes a representative value of the variable) remains at ∿1μs throughout the discharge. The field diffusion time $\tau_B = \frac{4\pi r^{o\,2}}{c^2\eta^o}$ is initially ∿5μs then increases to ∿20μs after the initial phase. The heat diffusion time $\tau_H = \frac{C_v\rho^o r^{o2}}{K^o}$ is ∿30μs throughout the discharge. The bouncing motions in Figure 9 are on the Alfven time scale as expected. The toroidal shift oscillation, which will be also on the Alfven time scale, is several fold slower than the bouncing motion. One of the main reasons for this would be that the half

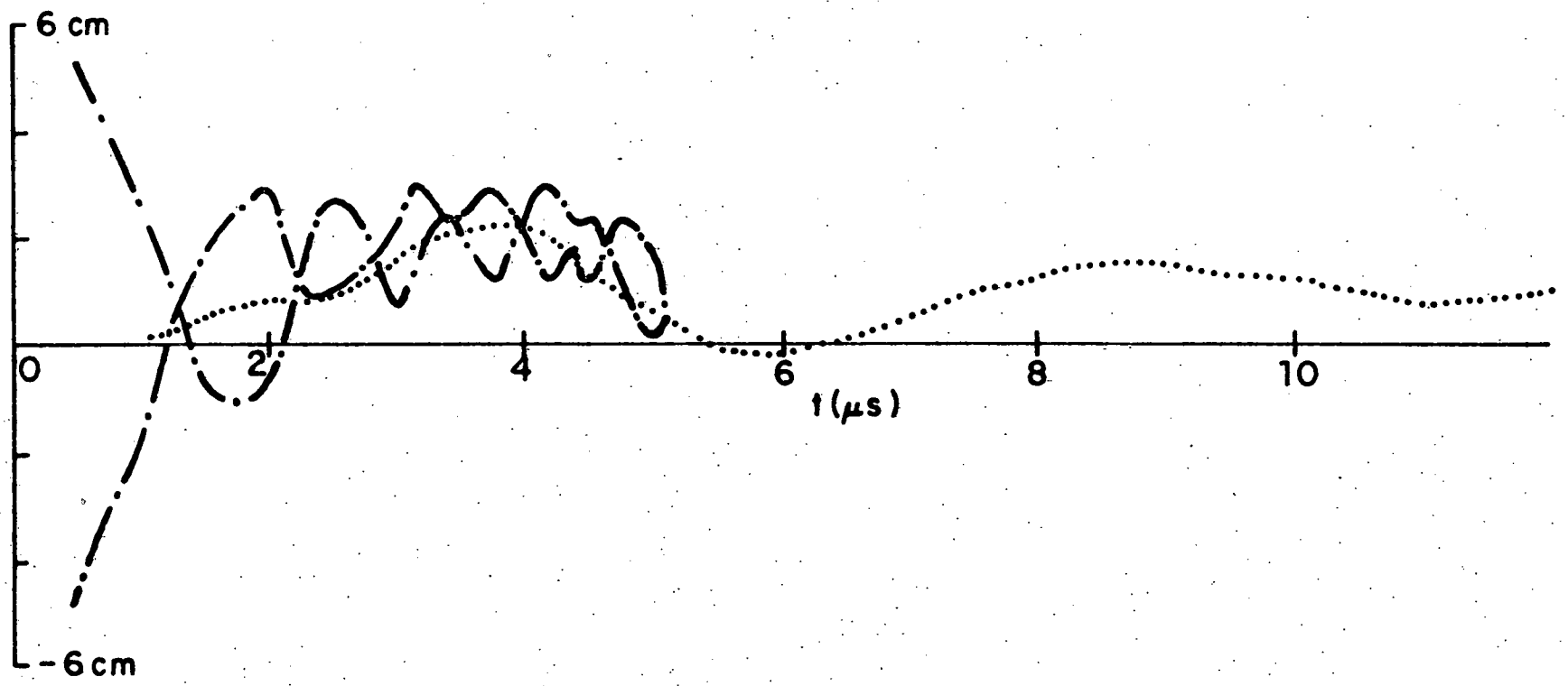

FIG. 9. TIME TRACES OF THE MAGNETIC AXIS (.....) AND THE TWO DENSITY PEAKS (— · —— · ——).

period of the toroidal shift oscillation corresponds to the time during which the overcompression of the magnetic field travels from one wall to the other, while the bouncing motions occur between the center and the wall.

The damping time scale of the bouncing motion in Figure 9 is $\sim$5μs, since a heavy field diffusion occurs during the initial pinching when the field diffusion time τ_B is short. On the other hand, the damping time of the toroidal shift oscillation is somewhat longer with a damping time scale of $\sim$10μs which is on the field diffusion time scale of the post implosion phase. Therefore, the damping time scale of the plasma oscillation is on the field diffusion time τ_B, as expected. One can ask, however, whether the heat diffusion time τ_H, if $\tau_H << \tau_B$, would determine the damping time scale. We tested this question by simulating discharges with parameters such that $\tau_H << \tau_B$, and found that τ_H does not determine the damping time scale, even when $\tau_H << \tau_B$. This fact can be easily understood by considering the limiting case where $\tau_H \to 0$ (i.e., the thermal conductivity $K \to \infty$). The temperature T becomes constant in this case, but the mechanical oscillation will still remain due to the density compression (i.e., $\nabla p = kT\nabla n$). In general, if the viscosity is included, the damping time will be determined by the smaller between τ_B and the viscous dissipation time $\tau_\nu = \frac{r_o^2}{\nu}$ where ν is the kinematic viscosity coefficient. Assuming the viscosity is classical (the

viscosity coefficient[21] $\nu \simeq \nu_i \sim \frac{kT_i\tau_i}{M_i}$, where the subscript i represents the ion species and τ the collison time), the viscous dissipation time τ_ν becomes $\sim$1 ms. This long time scale compared to other time scales τ_A, τ_B, and τ_H justifies the neglection of the viscosity in the calculation. The numerical viscosity in the calculation also results in an effective dissipation time of 100$\sim$1000μs (as discussed in Section 3.1), which is much longer than other time scales.

Figure 10 shows the radial velocity profiles on the horizontal diameter of the poloidal plane at various instants of time. The major axis is on the left and the plus sign of the velocity indicates outward (toward right) direction. At 1μs, we see imploding velocities of $\sim 5\times10^6$ cm/sec which is of the same magnitude as Alfven velocity. At 5μs, we see only small imploding velocities imbedded in a larger velocity of an inward toroidal shift. At 10μs, the fluid velocities dropped by orders of magnitude from the velocities of the imploding stage. These velocities still represent a small remaining oscillation of the toroidal shift (cf. Figure 9), and they are still somewhat larger than the diffusion velocity $v_D \sim \frac{c^2 n}{B^2}\nabla p$ which is $\sim 5\times10^4$ cm/sec. Nevertheless, for most practical purposes, this plasma state could be thought of as a quasi-equilibrium dissipation state. In other words, the remaining small toroidal shift oscillation will have little influence on the subsequent plasma evolution since the kinetic energy associated

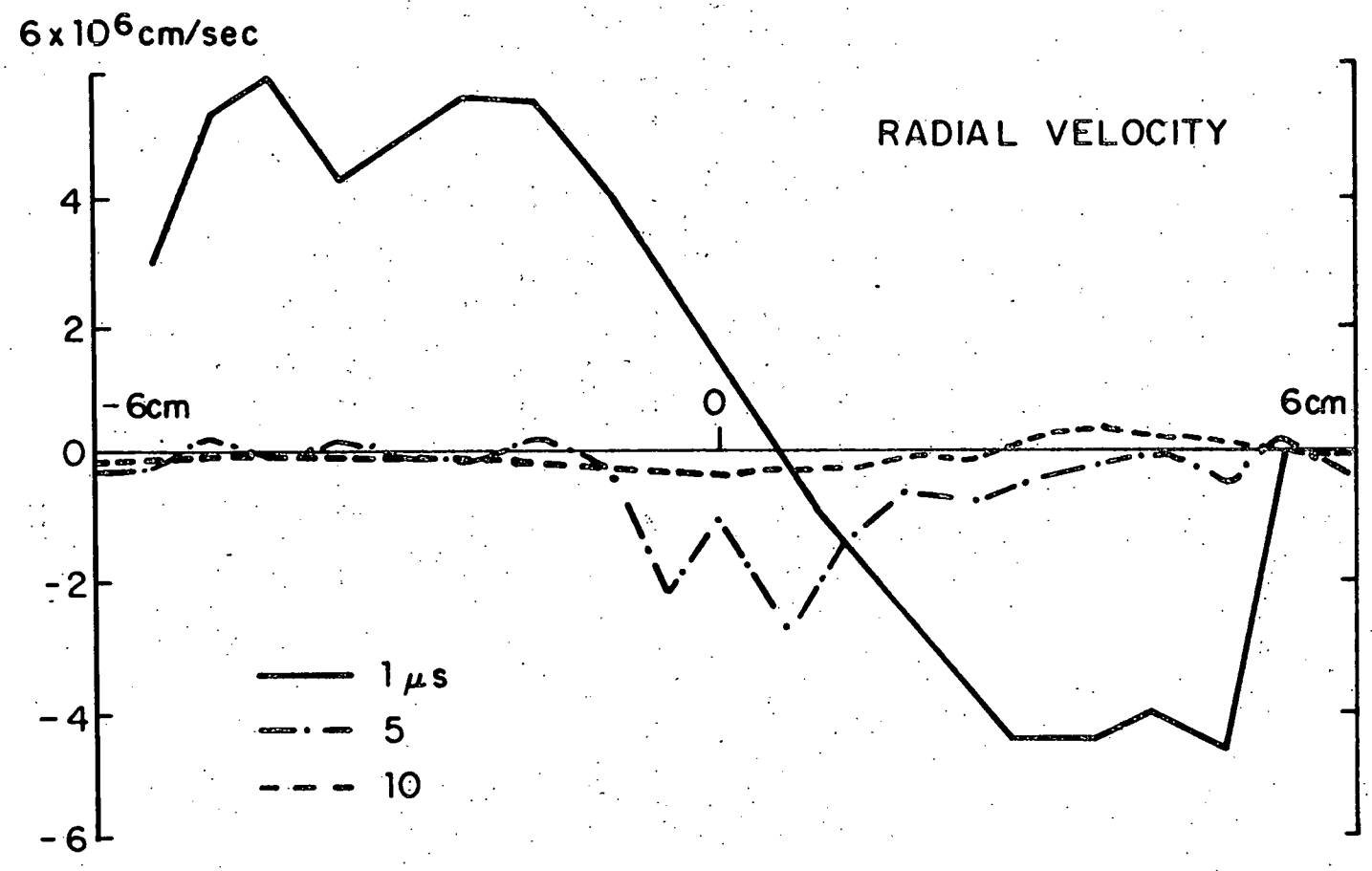

FIG. 10. RADIAL VELOSITY PROFILES ON THE SYMMETRY PLANE.

with this oscillation is many orders of magnitude smaller than both the magnetic field energy and thermal energy. The plasma evolution thereafter will be determined mainly by the dissipation mechanisms.

From the discussions on Figures (9 and 10), we can see that in a class of discharges as the present one, there will be three phases of the plasma state, namely, the initial phase where the radial pinching and bouncing motion is dominant, the second phase where the toroidal drifting motion is dominant and the final quasi-equilibrium dissipation phase. We note here that a strong toroidal flow is still remaining in the final phase. The magnitude of this velocity is comparable to the Alfven velocity. Therefore, the final plasma state is actually a steady quasi-equilibrium state rather than a static quasi-equilibrium state. The effect of the toroidal plasma flow will be discussed in detail in Section (4.3.B) where the toroidal curvature effects are explained.

Figure 11 shows the calculated toroidal (B_Z) and poloidal (B_θ)* field profiles on the horizontal diameter (Z=0) during the initial two bounces. Since the bouncing

---

* Although the poloidal field actually contains a small B_r component due to the toroidal curvature, we will frequently let $B_\theta\hat{\theta}$ represent the poloidal field for convenience, when the meaning is apparent from the context.

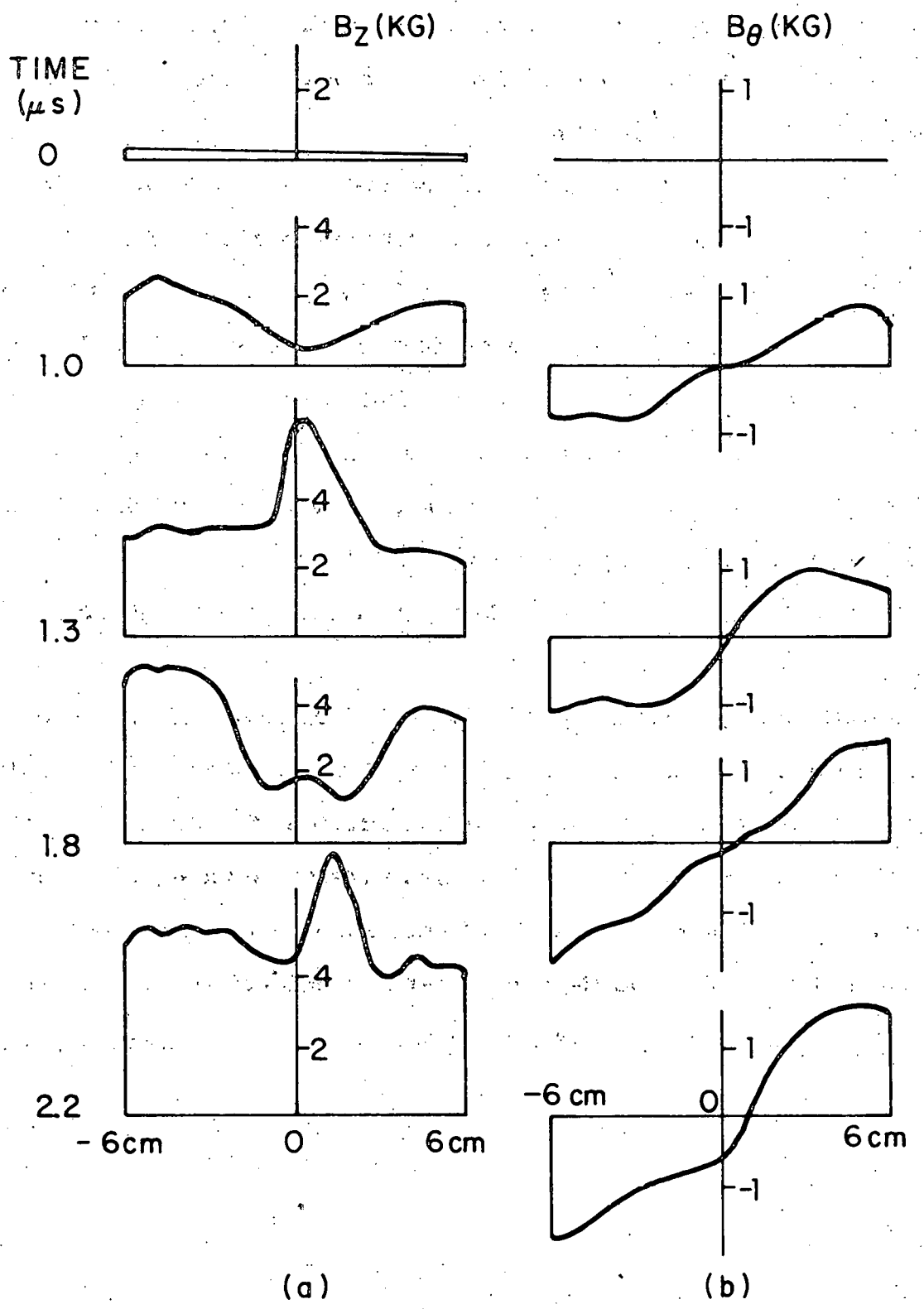

FIG.11. TOROIDAL(a) AND POLOIDAL(b) FIELD PROFILES DURING THE INITIAL PHASE.

time scale is much shorter than the field diffusion time, we see a clear convection of the fields according to the pinching and expansion.

Figure 12 shows the field profiles at much later instants (6, 8, and 10μs). At 10μs, most of the toroidal field has been convected and diffused in. The toroidal current also largely penetrated into the center and its profile became flat as readily seen from the almost straight B_θ profile. The toroidal field and the poloidal field each balance a pressure of $\sim\frac{(2kG)^2}{4\pi}$. (The field curvature accounts a half of the total B_θ magnetic pressure.) Therefore, the plasma beta $\beta = \frac{8\pi p_o}{B_o^2}$ is ~40% at 10μs with similar contributions from toroidal and poloidal fields. This fact that the toroidal field, even when it is much stronger than the poloidal field, contributes only similar amount of plasma pressure confinement as the poloidal field does, seems to be a general characteristic for the ohmically heated pinch experiments. The reason for this will be explained in Section (4.4.C) where we discuss confinement characteristics of the pinch experiments.

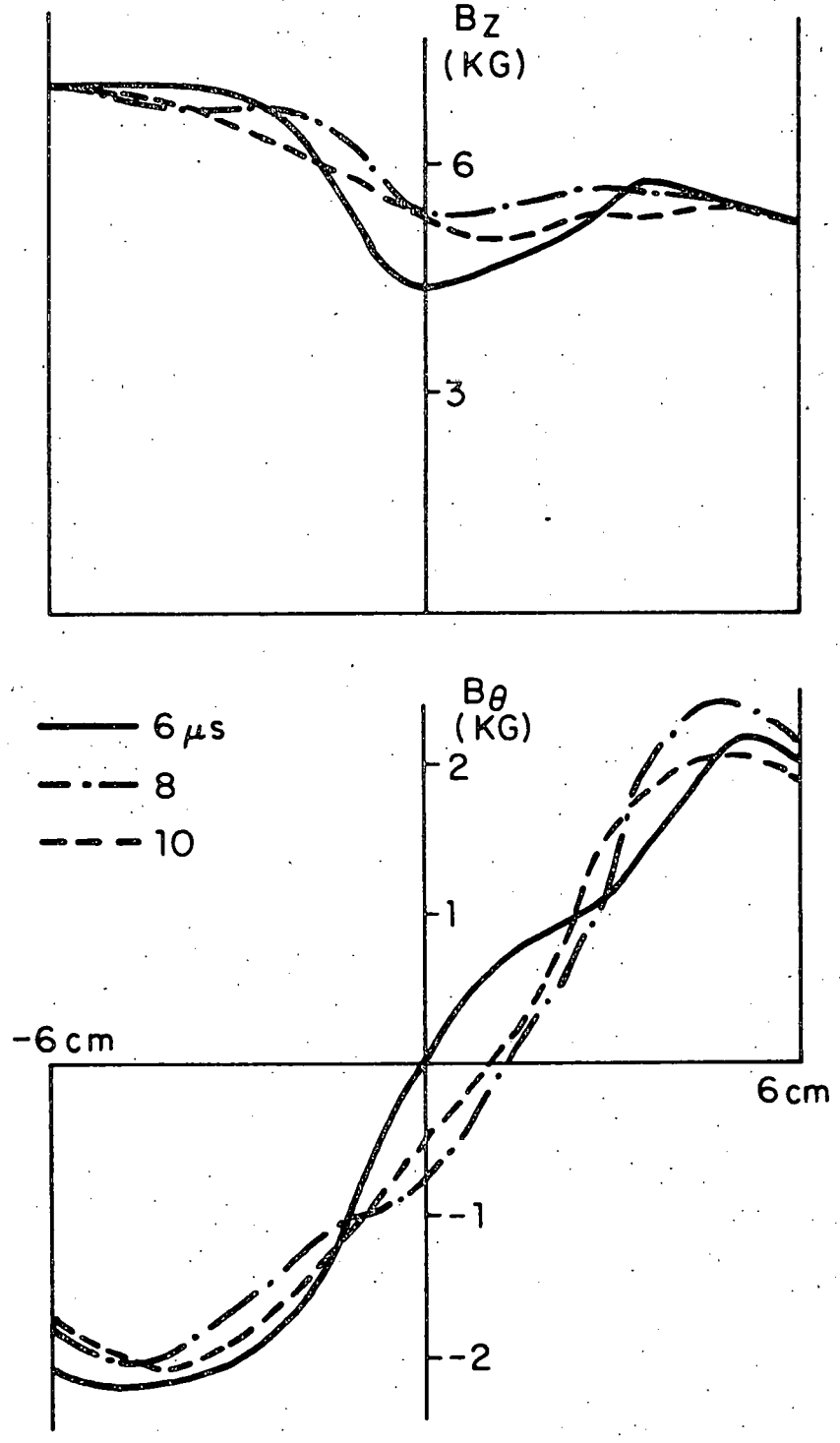

FIG. 12. TOROIDAL AND POLOIDAL FIELD PROFILES AT 6, 8 AND 10 μs.

4.2 ZT-I Reverse-Field Pinch

The ZT-I toroidal reverse-field Z pinch (which has been converted to a modestly larger ZT-S experiment) in Los Alamos had a major radius of 38.2cm and a minor radius of 5.2cm. We will present a simulation result of a discharge with $n = 8.2 \times 10^{-9} gm/cm^3$ denterium filling gas and initial temperature of 1 ev. Figure 13 shows two driving boundary conditions for this discharge, namely, the toroidal magnetic field at the wall and the total toroidal plasma current, as functions of time. The initial bias field is 1.6kG and the circuits are crowbarred at $t = 2.4\mu s$. It is noted that in ZT-I and ZT-S experiments, the magnetic fields are measured on the vertical radius ($\theta = \frac{\pi}{2}$) of the poloidal plane. Thus, whenever we compare the field profiles with the experiment, it is on the vertical radius.

In Figure 14, we present the toroidal and poloidal field profiles on the vertical radius ($\theta = \frac{\pi}{2}$) at 1.2, 2.0, and 2.8μs. The upper figure (a) shows the results from two different calculations, namely, one using the pure classical resistivity (the dashed curves) and the other using the Chodura anomalous resistivity algorithm (cf. Section (2.3)). The lower figure shows the experimental results and these results agree well with the calculated results. Although the results obtained using the anomalous resistivity show somewhat better agreement with the experiment than the classical resistivity results do, the difference is not definitive enough to conclude that the classical resistivity is invalid.

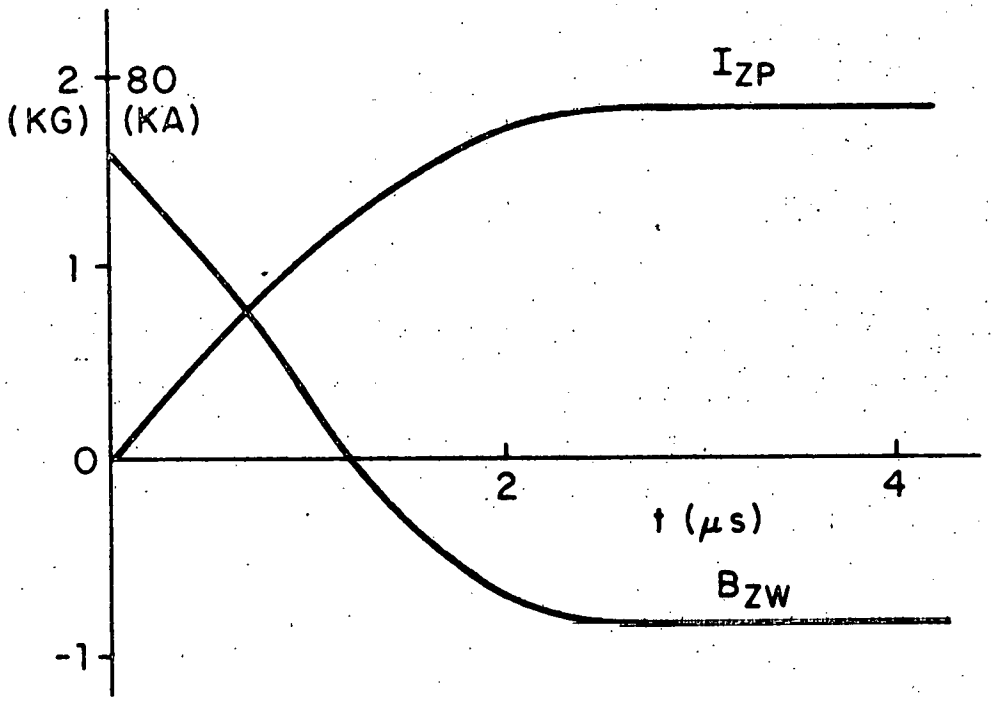

FIG. 13. TIME TRACES OF THE TOROIDAL MAGNETIC FIELD AT THE WALL AND THE TOTAL TOROIDAL PLASMA CURRENT IN A ZT-I DISCHARGE.

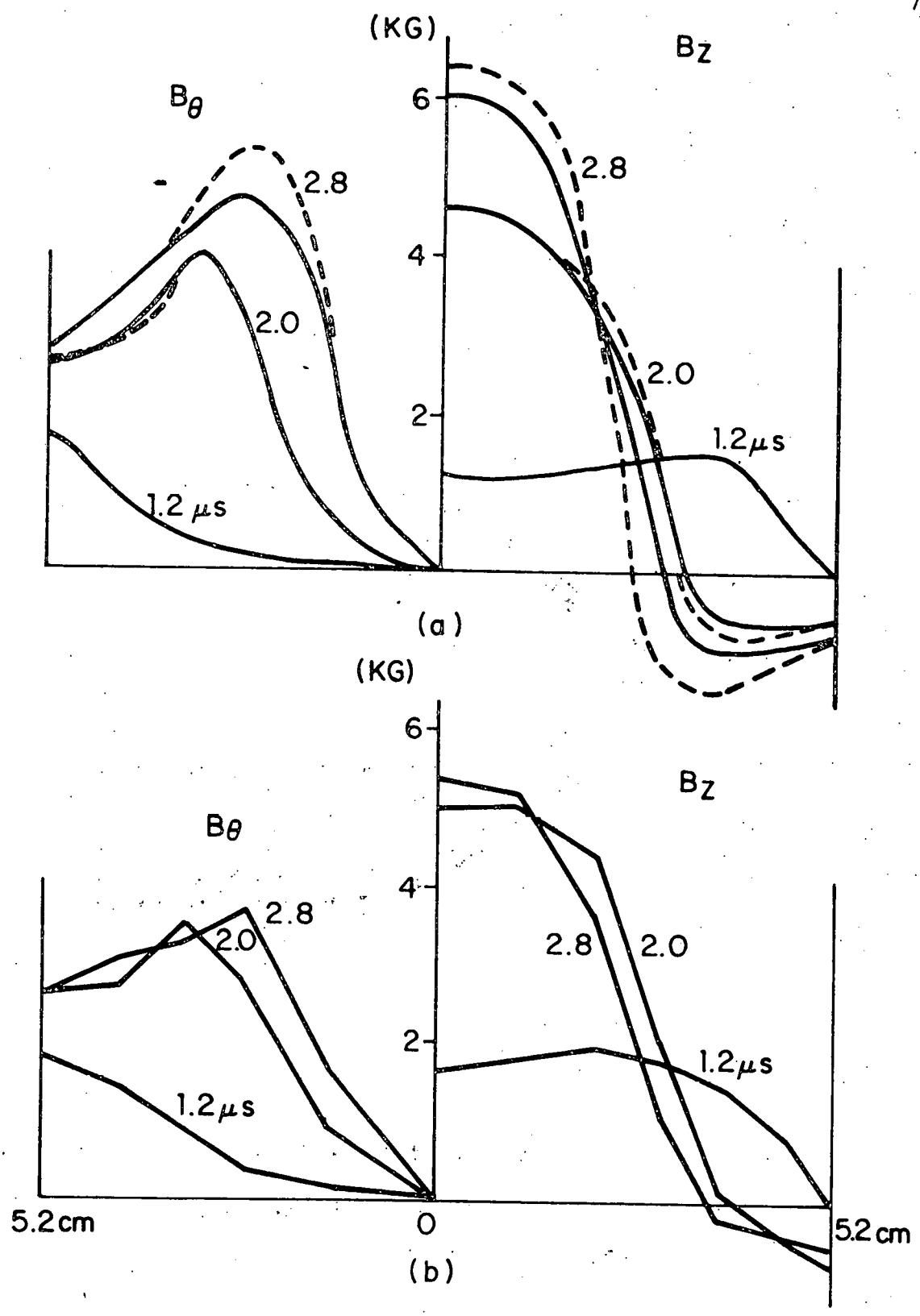

FIG.14. TOROIDAL AND POLOIDAL FIELD PROFILES: (a) CALCULATION RESULTS WITH CLASSICAL RESISTIVITY (------), AND WITH THE ANOMALOUS RESISTIVITY (————); (b) EXPERIMENTAL RESULTS.

We also compared these calculation results with the simulation results of the same discharge due to Sgro and Nielson[18] who used a one-dimensional hybrid (fluid electrons and Vlasov ions) code. The results of the two simulations using anomalous resistivity agreed with each other quite well. However, the results of the hybrid simulation using the pure classical resistivity show a marked difference, as shown in Figure 15. This figure shows the field profiles at 1.2μs and the profiles do not compare with the experiment. These field profiles with very thin current sheath seem to be due to near zero thermal conductivity used in the hybrid simulation. If there is no thermal conduction, the initial current flow on the plasma skin will result in a local overheating of the skin. This high temperature skin will in turn results in a very

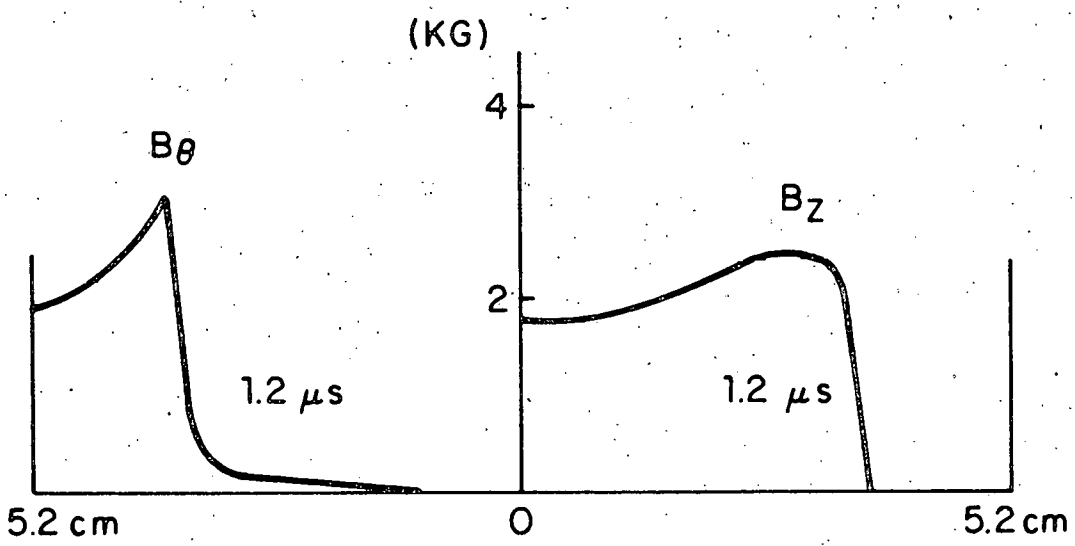

FIG. 15. POLOIDAL AND TOROIDAL FIELD PROFILES FROM THE HYBRID CALCULATION USING CLASSICAL RESISTIVITY

thin current sheath, since the classical resistivity decreases at $\propto T^{-3/2}$. On the other hand, for the anomalous resistivity, the temperature dependence is much weaker and, moreover, there is additional dependence on the current density and the plasma density. ($\eta_a \propto \frac{j}{T^{1/2} n^{3/2}}$, in the high temperature limit.) Therefore, the current sheath will spread, even when there is no thermal conduction as in the hybrid simulation case. This explains the similar results obtained from the two simulations both using the same anomalous resistivity. Other reasons for the similarity of the two simulation results should be also mentioned, that is, the ion reflection from the magnetic piston which can be seen in the hybrid code and not in our fluid code, is small due to the high bias field, and also the toroidal curvature effect which is naturally taken into account in our two dimensional code gives small difference in the overall shape of the magnetic fields due to the large aspect ratio of ZT-I. (Nevertheless, this toroidal curvature effect gives rise to some important phenomena as explained in Section (4.3.B).) As a conclusion for this paragraph, we note that the calculation results with the Chodura anomalous resistivity are relatively insensitive to the thermal conductivity used, while the results with the classical resistivity are more sensitively dependent on the thermal conductivity.

Figure 16 shows the profiles of the plasma density, toroidal current density and the ratio of the anomalous resistivity to the classical resistivity η_a/η_{cl} on the vertical radius ($\theta = \frac{\pi}{2}$) at 1.6, 2.0 and 2.8μs. Values of η_a/η_{cl} are

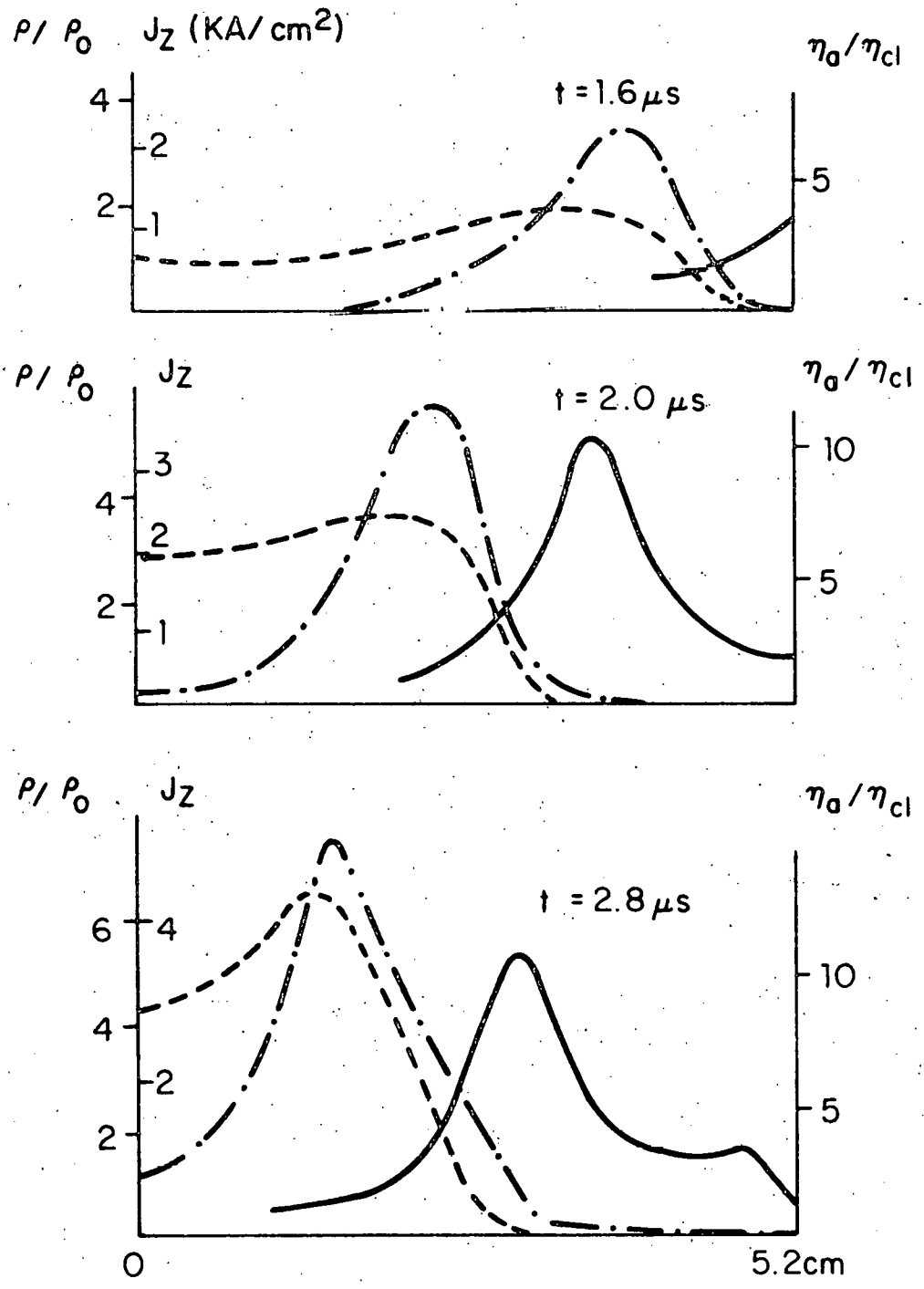

FIG.16. PROFILES OF THE PLASMA DENSITY(-------), TOROIDAL CURRENT DENSITY(— · — · —) AND THE RATIO OF THE ANOMALOUS RESISTIVITY TO CLASSICAL ONE(————)

shown only where the anomalous resistivity is turned on (i.e., $\eta_a > \eta_{cl}$). Inside the main plasma column, the resistivity remains essentially classical. The anomalous resistivity affects mainly on the outside low density region. This effect on the low density region would not much influence the overall plasma behavior, since the current in this region is already weak. This is because the pressure gradient is small in this region and therefore, the fluid velocity approximately cancels out the electric field (i.e., $\frac{u \times B}{c} \sim -E$). Thus, we note that the fluid velocity in the calculation should be given correctly in the low density region especially when the classical resistivity is used (cf. Section (3.3)).

The discussion on Figure 16 explains the fact that the field profiles, one obtained using the anomalous resistivity and the other using the classical resistivity, were quite close (Figure 14). Also, the temperature profiles which would be strongly affected by the resistivity coefficient are quite close for the two cases as shown in Figure 17. The solid curves are obtained using the anomalous resistivity and the dashed curves using the classical one.

All the above discussions are true only in the initial setting up phase of the discharge, of which the time scale is much shorter than the dissipation time scales. Quite different results are obtained in the later dissipation phase when the dissipation process becomes more important. This later phase will be discussed in Section (4.3.A). It will be shown that the anomalous resistivity is not valid for this

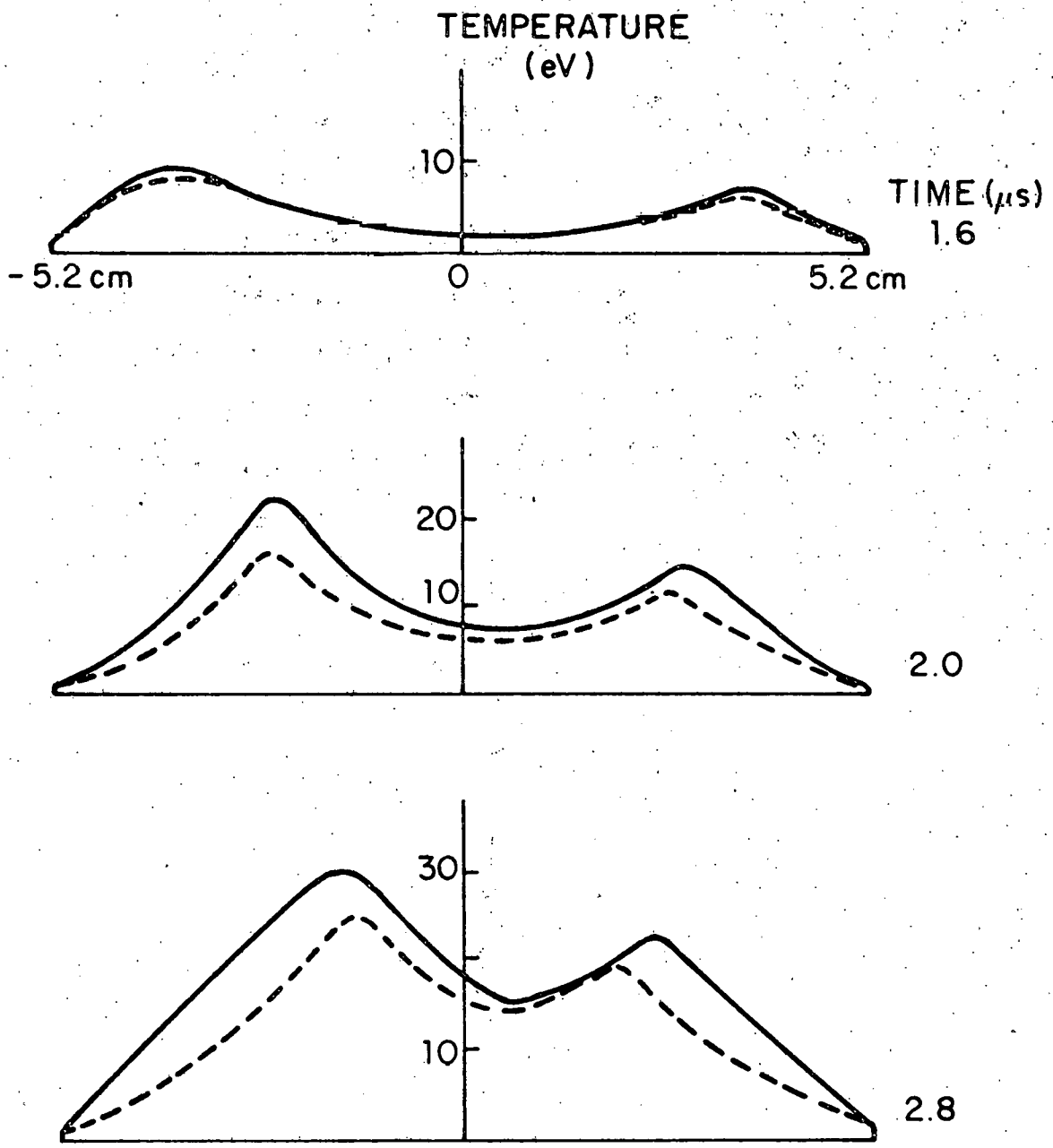

FIG.17. TEMPERATURE PROFILES AT 1.6, 2.0 AND 2.8 μs. SOLID CURVES ARE OBTAINED USING THE ANOMALOUS RESISTIVITY AND DASHED CURVES THE CLASSICAL ONE.

phase and instead, the classical resistivity gives better comparison with the experiment.

The results discussed in this section are consistent with the simulation results of HBTX-1 reverse-field pinch by the Culham group and also with that of Eta-Beta reverse-field pinch by the University of Padua group. The Culham group reported that 'Both the setting up and the decay phase of HBTX-1 can be simulated numerically using classical coefficients.' The Padua group reported[20] that 'No clear indication about the classical or anomalous nature of the resistivity appears from the simulated gross plasma behavior of Eta-Beta experiment.'

4.3 ZT-S Reverse-Field Pinch

4.3.A. General Behavior of the Plasma

ZT-S reverse-field pinch [5] is an enlarged version of the previous ZT-I experiment. The minor radius has increased modestly from 5.2cm to 7.7cm while the major radius remained about the same. One of the main purposes of this larger size is to study the scaling behavior of reverse-field pinches. This would also give more information for the design of the larger ZT-40 experiment.

Figure 18 shows the two field boundary conditions of the discharge we simulate. The toroidal plasma current rises to 55kA in 1.6μs, and the initial toroidal bias field of 0.5kG is reversed at 3.6μs. Initially, $\rho_o = 2.2 \times 10^{-9}$ gm·cm^{-3} deuterium filling gas with $T_o = 2$ev is present.

In Figure 19, the density profiles on the poloidal plane are shown at various instants of time. The initial pinching reaches its maximum at 2.1μs, and then the plasma expands until 2.6μs. Several successively smaller pinching and bouncing motions follow until a relatively quiet phase is reached at 4.6μs (cf. discussions on Figure 21). The plasma stays well away from the wall in the calculation throughout the discharge.

Figure 20 shows the calculated toroidal and poloidal field profiles (shown in solid lines) on the vertical radius ($\theta = \frac{\pi}{2}$) of the poloidal plane, compared with the experimental values (shown in dashed lines), at 2.6 and 4.6μs. Chodura anomalous resistivity is used for the results shown. These results do not change significantly when classical resistivity is used instead, in this initial setting-up phase, as discussed

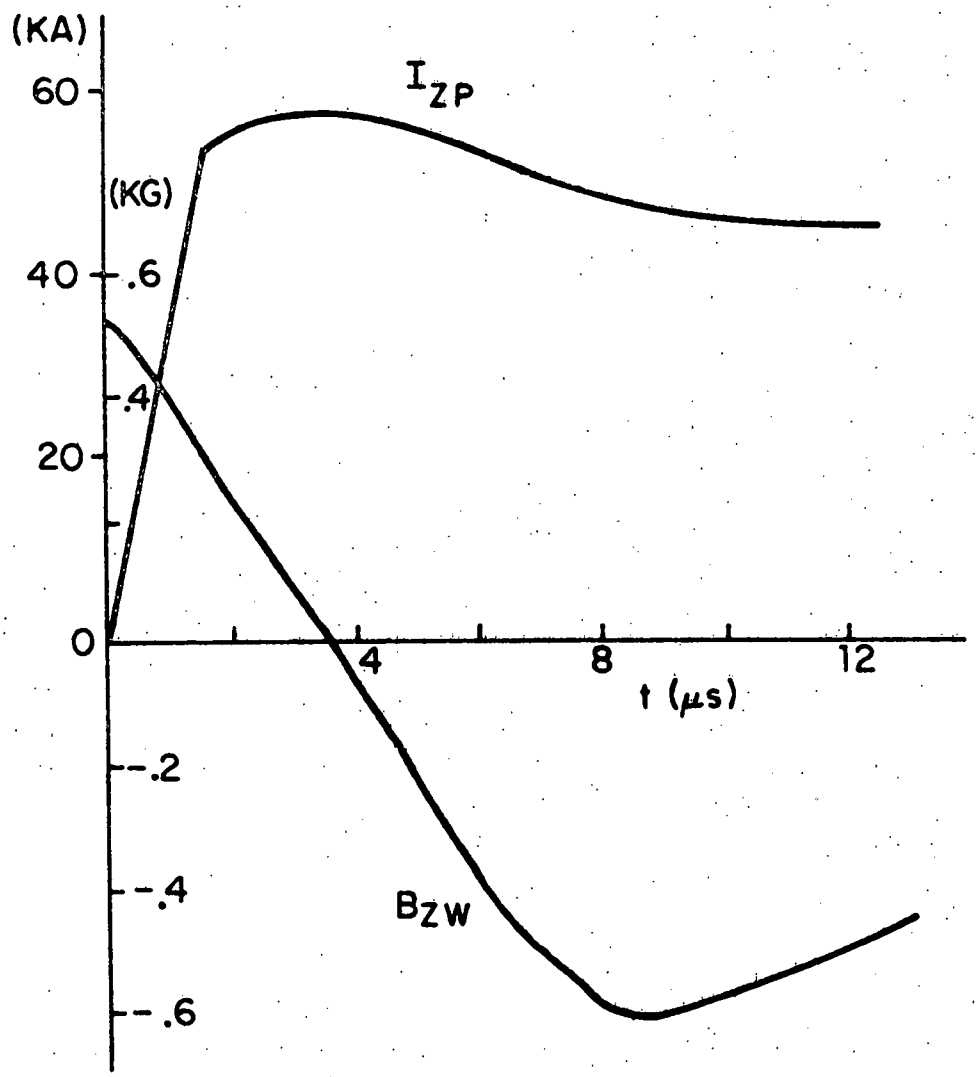

FIG.18. TIME TRACES OF THE TOTAL TOROIDAL PLASMA CURRENT I_{zp} AND THE TOROIDAL FIELD AT THE WALL, B_{zw}.

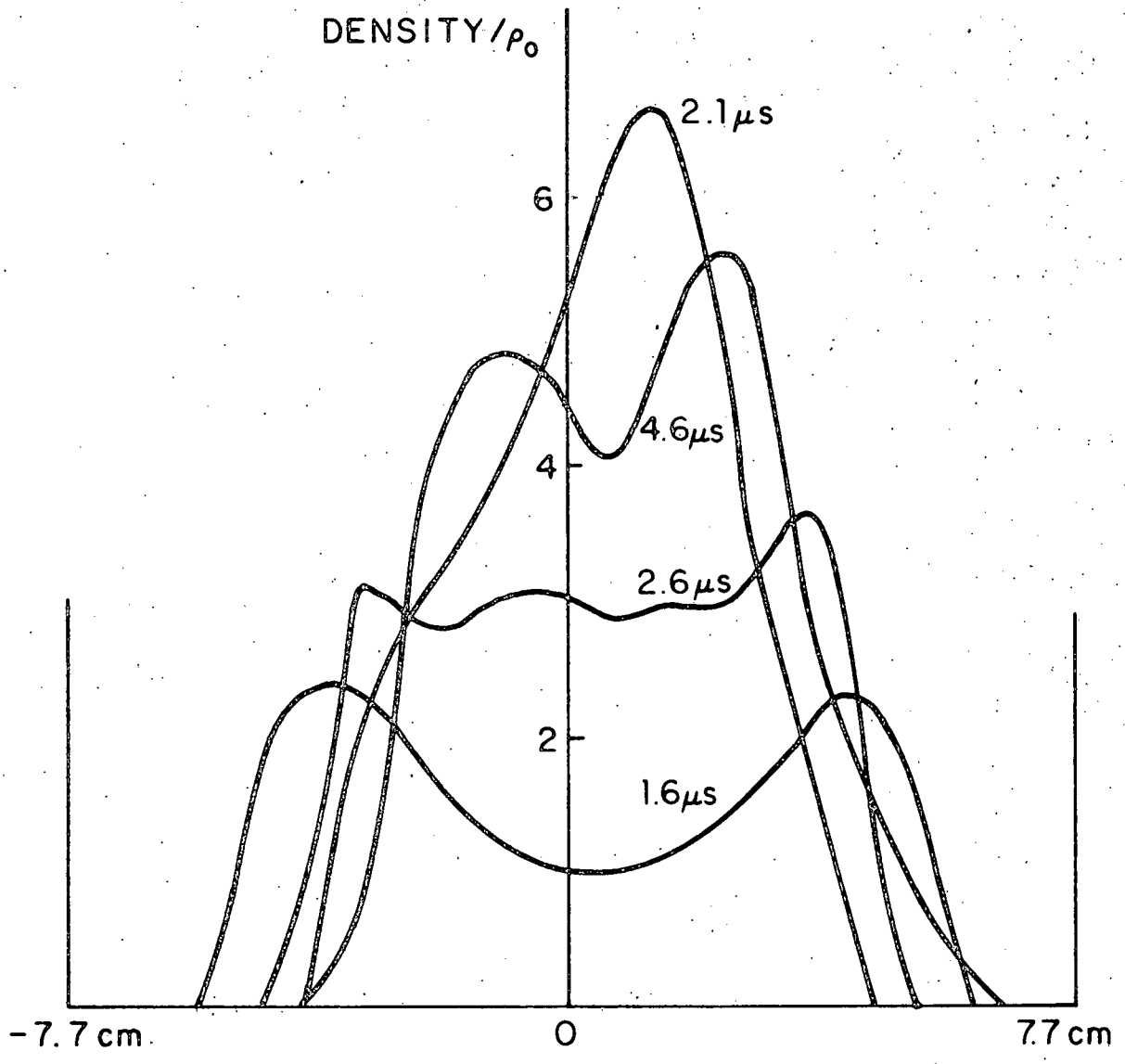

FIG. 19. DENSITY PROFILES NORMALIZED TO THE INITIAL DENSITY

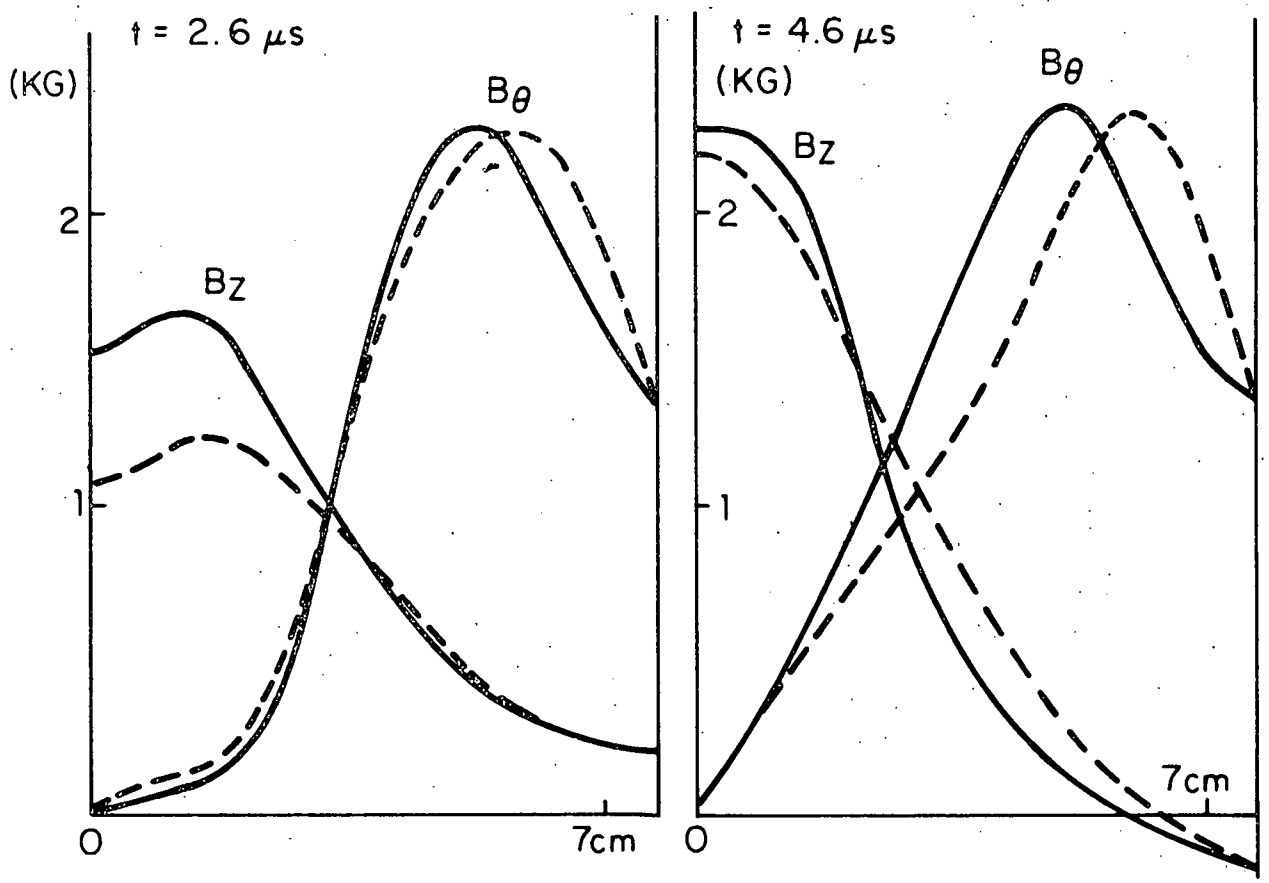

FIG. 20. TOROIDAL AND POLOIDAL FIELD PROFILES ON THE VERTICAL RADIUS ($\theta=\pi/2$) of THE POLOIDAL PLANE ARE COMPARED BETWEEN THE CALCULATION(————) AND EXPERIMENT(---------) AT 2.6 AND 4.6 μs.

in the case of the ZT-I experiment (Section 4.2). The agreement shown in Figure 20 is quite satisfactory. The large difference between the two toroidal field values at the center (r = 0) at 2.6μs is due to a small time lag of the calculation, which can be seen in the next figure.

In Figure 21, the toroidal field at the minor axis is shown as a function of time. The points represent the experimental values. The second and third points correspond to 2.6μs and 4.6μs depicted in the previous Figure 20. The observed point at 2.6μs shows that the large discrepancy between two field values at the center is due to a small time lag of the calculation. This figure also shows that a quiet phase is reached at about 5μs, as discussed before for Figure 19. This quiet phase actually corresponds to the second phase of the pinch when the toroidal drifting motion is dominant, as explained in Section (4.1) for SP-1 screw pinch. This can be readily seen from Figure 24 in the next section, which shows the time trace of the toroidal shift of the same discharge, and this figure also shows that the toroidal drifting oscillation is much smaller in this reverse-field pinch case than in the previous SP-1 screw pinch discharge. The good agreement shown in Figure 21 in the later quiet phase, i.e., 6.6 and 8.6μs, is found misleading, since the field profiles as a whole do not compare each other between calculation and experiment, as will be seen in Figure 23. Also, we will see that the anomalous resistivity and the pure classical resistivity give quite different results at this later time. This is because the

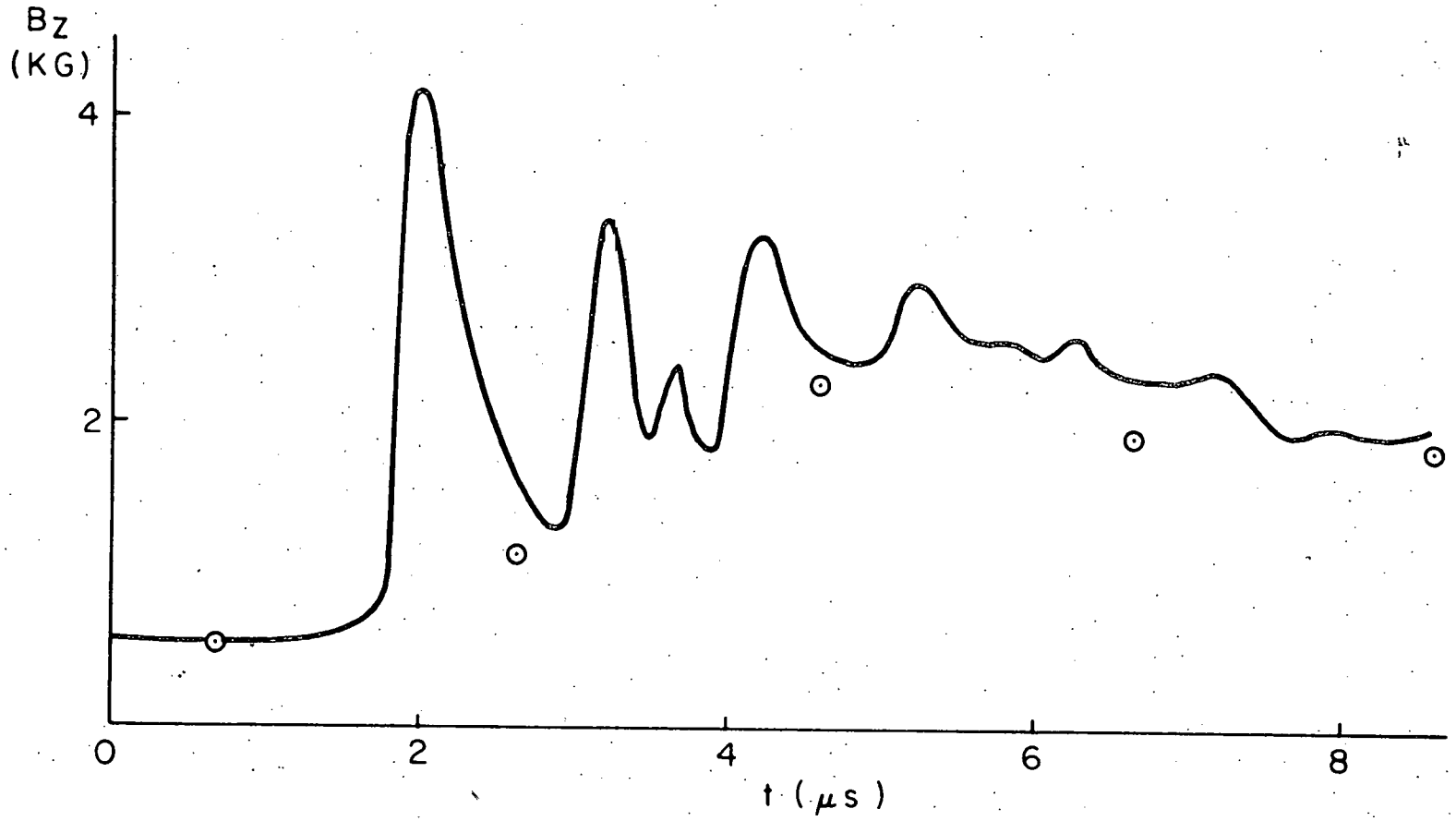

FIG. 21. TIME TRACE OF THE CALCULATED TOROIDAL FIELD AT THE MINOR AXIS. THE POINTS REPRESENT THE EXPERIMENTAL VALUES.

elapsed time is by now comparable to the field diffusion time of ∿10μs, and more importantly, because the anomalous resistivity is turned on throughout the plasma by 6μs, as shown in Figure 22. This figure shows the profiles of the plasma density, toroidal current density and the ratio of the anomalous resistivity to the classical resistivity, and should be compared to Figure 16 of the ZT-I case. The anomalous resistivity is turned on throughout since the current and temperature are high throughout the plasma.

Figure 23 compares the toroidal and poloidal field profiles between the experiment and the two separate calculations each using different resistivity coefficient. The broken lines represent the experimental values and the semi-broken lines the calculation results using the anomalous resistivity coefficient. The semi-broken lines indicate much more compressed plasma profiles than the observed results indicate. This over-compression is probably due to the large loss of trapped toroidal flux in the calculation. The trapped flux in this calculation appears to be less than half of the observed. (Recall that the cross section is circular.) This strongly suggests that the real resistivity is much less than the anomalous resistivity used. Therefore, another calculation was made where the anomalous resistivity was replaced by pure classical resistivity after 5μs and the thermal conductivity coefficient was also reduced by a factor of 10 at the same time. The solid lines in Figure 23 represent this result, and they show much better agreement with the experiment. The trapped flux in this

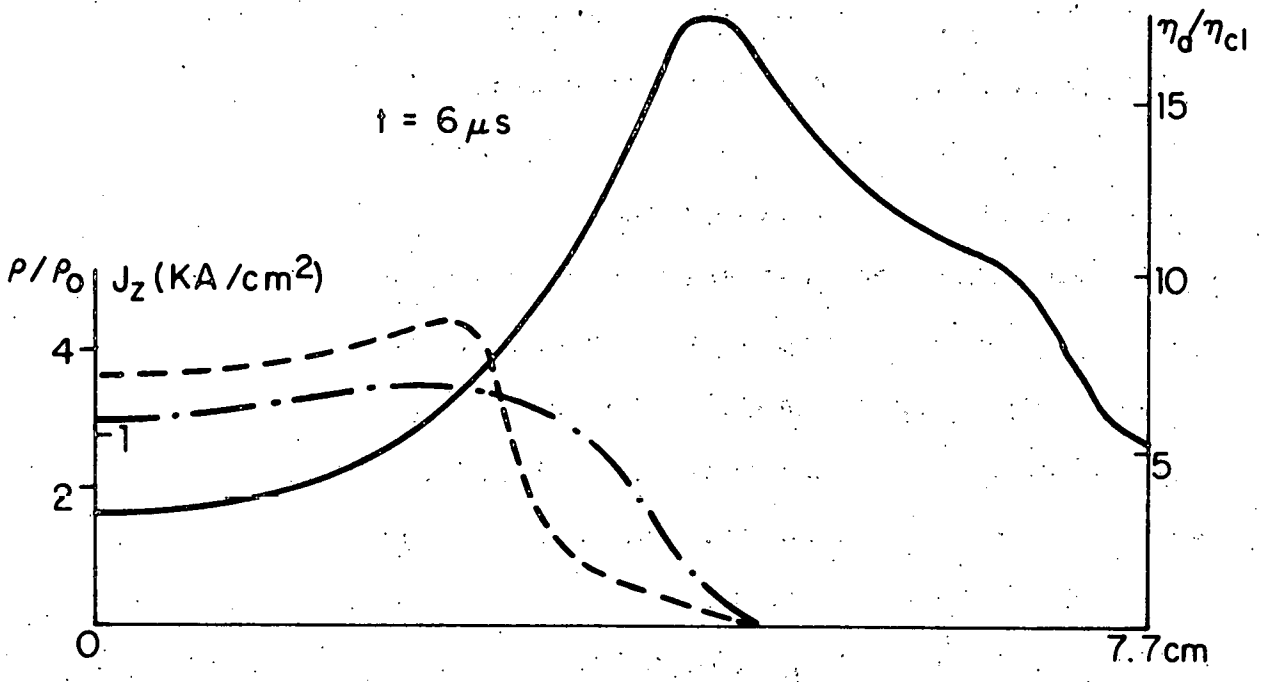

FIG. 22. PROFILES OF THE PLASMA DENSITY (---------), TOROIDAL CURRENT DENSITY (— · — · —) AND THE RATIO OF THE ANOMALOUS RESISTIVITY TO THE CLASSICAL ONE (————————) AT 6 μs.

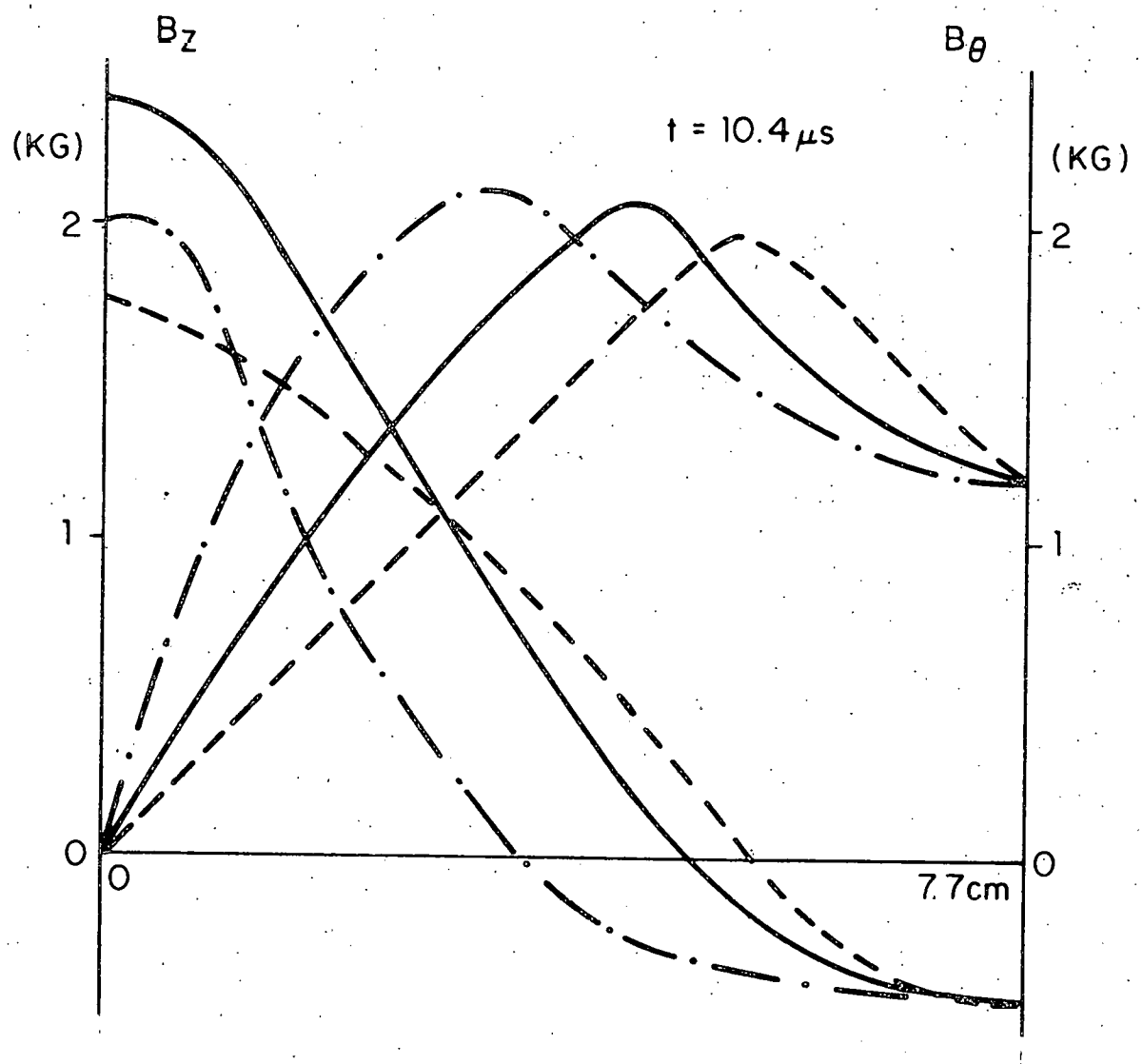

FIG.23. TOROIDAL AND POLOIDAL FIELD PROFILES AT 10.4 μs ARE COMPARED BETWEEN THE EXPERIMENT(--------) AND TWO SEPARATE CALCULATION RESULTS, ONE OBTAINED USING THE ANOMALOUS RESISTIVITY THROUGHOUT(— · — ·—) AND THE OTHER BY TURNING IT OFF AT 5 μs(————————).

calculation is about the same as the observed one. If the thermal conductivity is kept the same instead of reducing 10-fold, the plasma collapses a little more but the trapped flux remains about the same.

From these discussions, we conclude that, for the simulation of the later, quiet phase, the Chodura anomalous resistivity algorithm is invalid, and the real resistivity seems to be quite close to the classical one. This is consistent with a concept of the anomalous resistivity being the effect of the plasma instabilities generated in the initial violent phase. (See also the related discussions at the end of Section (4.2).) Whether this will be still true for the higher temperature and higher current density regime is an important question which should be investigated, for example, by ZT-40 experiment.

Now the scaling behavior of ZT-S is briefly discussed. Since diffusion times $\propto a^2/D$ (a = plasma radius, D = diffusion coefficient) and the stable period in a reverse-field pinch discharge is found to be limited by field diffusion,[32] one expects that a ZT-S discharge would have at least twice longer stable time compared to a similar ZT-I discharge. This was confirmed in the experiment, which measured a stable time of $\sim$30μs in ZT-S compared to $\sim$15μs in ZT-I. It is also reported that a significant current penetration into the center of the plasma occurs at $\sim$5μs in ZT-S compared to $\sim$2μs in ZT-I. This was also seen in the calculation. Here, we just refer to

Figure 14 on page and Figure 20 on page . From the poloidal field profiles of ZT-I in Figure 14, we see that the toroidal current largely penetrated to the center at 2μs. On the other hand, Figure 20 shows negligible current penetration to the center at 2.6μs in ZT-S. A significant current penetration occurs at ~4μs and the field profiles at 4.6μs becomes as shown. A more detailed discussion on the scaling behavior is made in Section (4.4) where the larger ZT-40 experiment is studied.

4.3.B. Toroidal Curvature Effects

In this section, we study the toroidal curvature effects, using simulation results of the same discharge studied in the previous section. These toroidal effects are automatically incorporated in our two space dimensional code. In Figure 24, the calculated toroidal shift of the magnetic axis is shown as a function of time. This shows an outward toroidal shift of $\sim$1cm. (The minor radius of the torus is 7.7cm.) From this figure and Figure 21 on page , we can see that the three stages of the discharge, i.e., the bouncing, toroidal drift and diffusion phase occur as in the case of SP-1 screw pinch. The time scales of these three phases can be similarly explained as for the SP-1 case in Section (4.1). However, the toroidal drift oscillation appears to be much smaller compared to the SP-1 case in Figure 9.

Although this toroidal effect does not much influence the overall plasma profiles, it nevertheless, gives rise to many important phenomena such as the toroidal plasma flow which will be discussed later. Some diagnostic interpretations are also influenced by the toroidal effect, as shown in the next figure. Figure 25 shows two calculated current density profiles at 6.5μs. The solid line represents the current density on the vertical diameter ($\theta = \frac{\pi}{2}$) of the poloidal plane, while the dashed line on the horizontal diameter. We note that the vertical profile appears almost flat in the main plasma region, while the horizontal profile is still hollow, revealing that the whole two-dimensional current density profile is actually

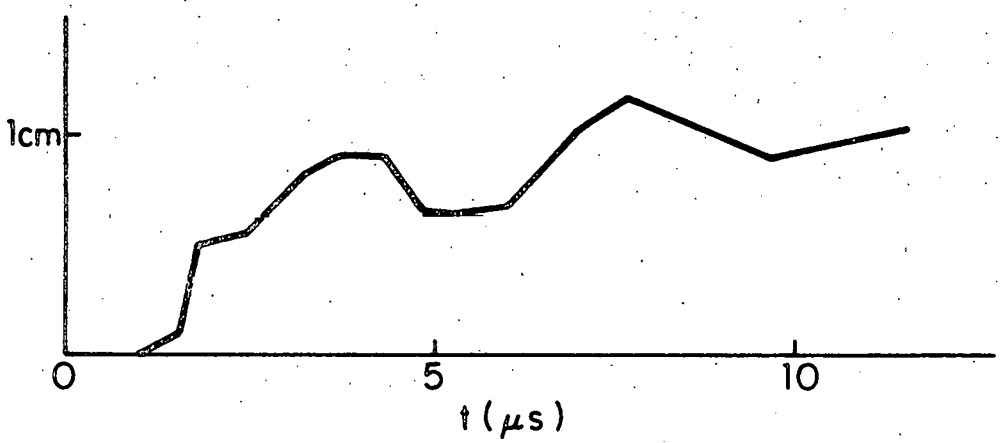

FIG.24. TIME TRACE OF THE TOROIDAL SHIFT OF THE MAGNETIC AXIS.

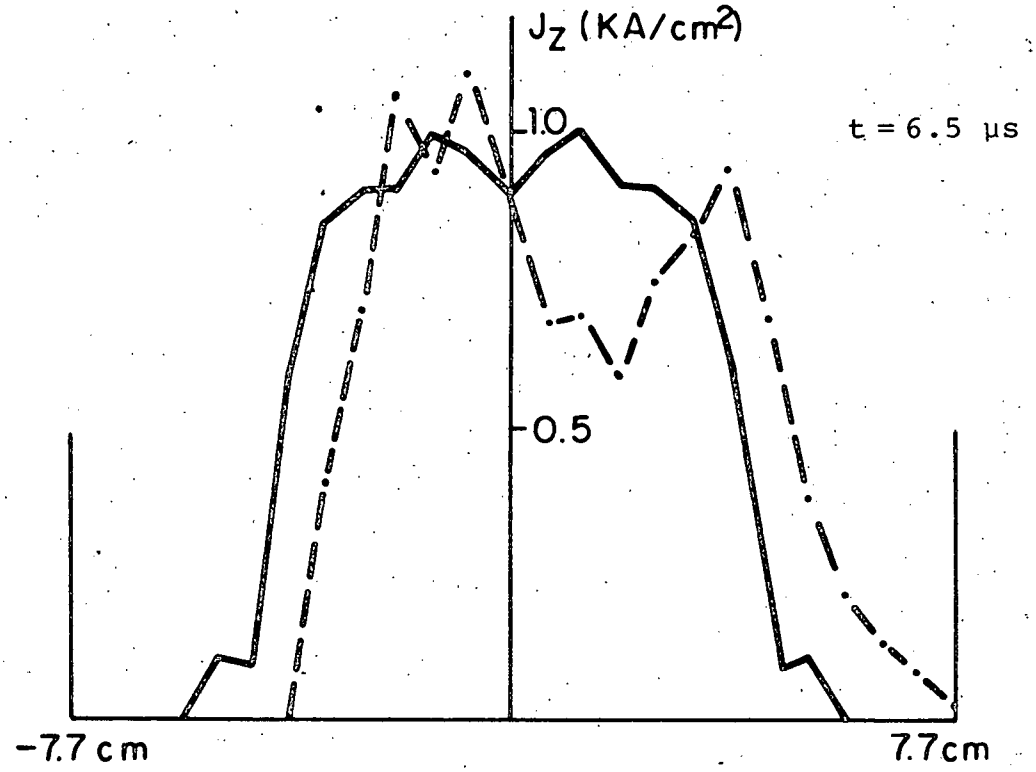

FIG. 25. CALCULATED TOROIDAL CURRENT DENSITY PROFILES AT 6.5 μs. THE SOLID LINE REPRESENTS THE VALUES ON THE VERTICAL DIAMETER($\theta = \pm\pi/2$) OF THE POLOIDAL PLANE, AND THE DASHED LINE ON THE HORIZONTAL DIAMETER.

annular. Since the ZT-S machine has only vertical diganostic ports, the experiment, at this instant, would measure only the flat vertical profile, and may give wrong conclusion that the whole current profile is already flat. The resistivity so deduced would be erroneously high. This shows an example which indicates that a horizontal diagnostic port would be necessary due to the toroidal curvature effect, for accurate diagnostics.

The large difference between the vertical and horizontal profiles shown in Figure 25 is, of course, directly related to the toroidal shift shown in Figure 24. This shift of $\sim$1cm is about twice larger than the toroidal shift predicted from an equilibrium calculation of the Los Alamos group.[33] This difference is likely due to a strong toroidal plasma flow which is seen in our calculation but not included in the equilibrium calculation. Figure 26(a) shows the time traces of the three computed velocity components, i.e., the radial (U_r), azimuthal (U_θ), and toroidal (U_ϕ) velocities, at a point depicted in Figure 26(b). The toroidal velocity is antisymmetric against the midplane as depicted in Figure 26(b). Therefore, the angular momentum is conserved. The oscillations of the radial and azimuthal velocities are largely damped away at 5μs, but the toroidal velocity persists and increases until it reaches a steady magnitude at $\sim$10μs. Therefore, the final plasma state is a steady quasi-equilibrium state rather than a static one, as in the SP-1 case. The steady equilibrium is a very complex problem which is largely remained to be investigated,

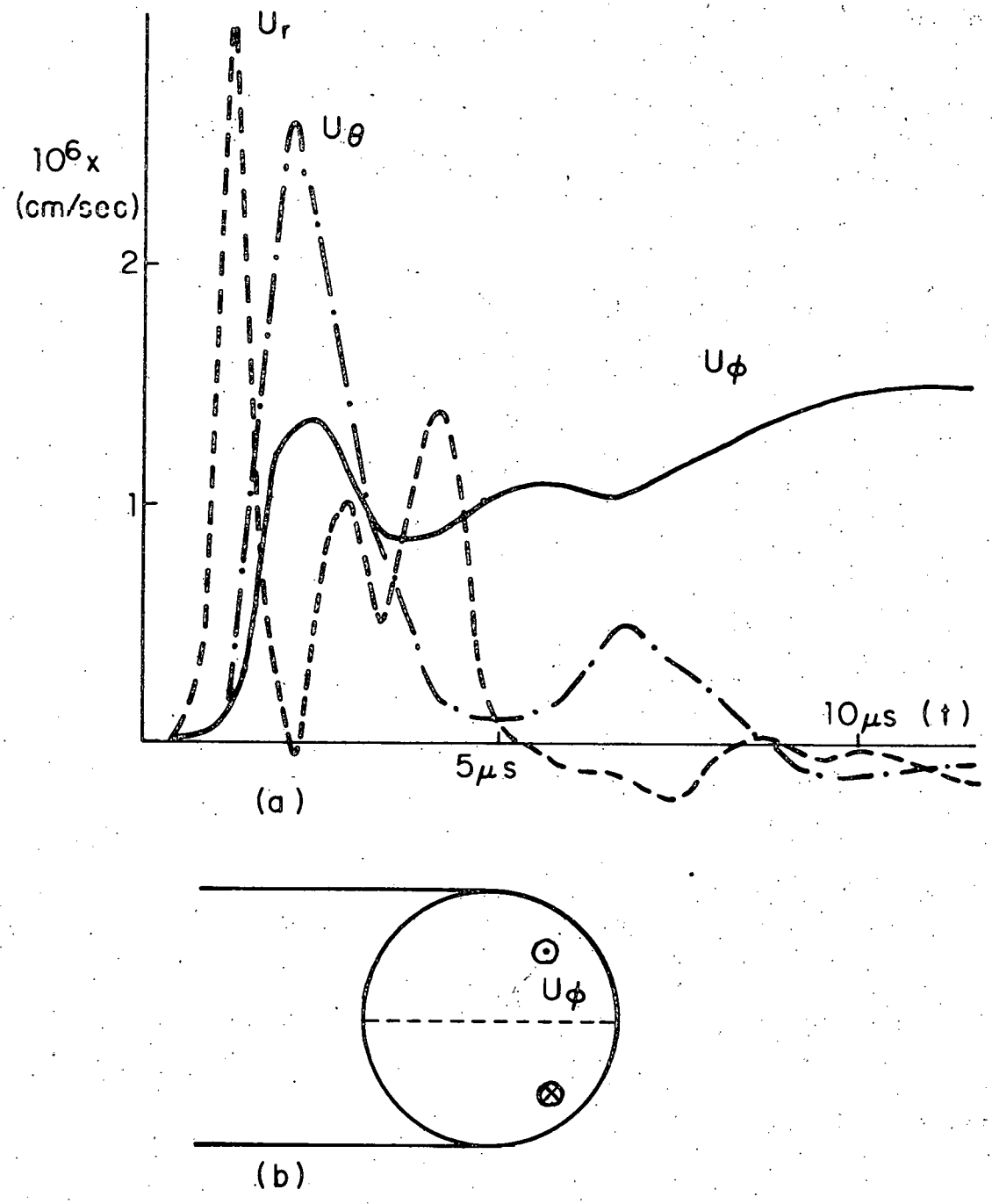

FIG.26. TIME TRACES OF THE RADIAL (U_r), AZIMUTHAL (U_θ) AND TOROIDAL (U_ϕ) VELOCITIES AT THE POINT DEPICED IN FIGURE (b).

especially in a finte beta case. (For a review, see for example, Green (34)). Here we just estimate the effect of the toroidal plasma flow on the toroidal shift. For a steady equilibrium, the convection term should be added to the usual pressure balance equation of the static equilibrium, so that

$$\rho \underline{u} \cdot \nabla \underline{u} + \nabla p = \frac{\underline{j} \times \underline{B}}{c}$$

For the present case, $\rho \underline{u} \cdot \nabla \underline{u} = -\rho \frac{u_\phi^2}{R} \hat{R}$, with $u_\phi \sim 1.5 \times 10^6$cm/sec. This 'centrifugal pseudo pressure gradient' is an order of magnitude smaller than the average magnetic pressure gradient $(\frac{\underline{j} \times \underline{B}}{c})$. Therefore, we can expect that an additional toroidal shift of about one-tenth of the torus minor radius is necessary to balance this centrifugal force.

We are not aware of any toroidal plasma flow measurements which can be checked with the present results. Although a toroidal plasma flow of $u_\phi = \sim 10^6$cm/sec has been reported in the ORMAK experiment in Oak Ridge and also in the PLT experiment in Princeton [35], both under a neutral beam injection heating, these results were attributed to the momentum transfer from the neutral beam. The toroidal velocities, therefore, did not show antisymmetric profiles against the midplane. Nevertheless, we believe that a careful measurement will reveal a strong toroidal flow with antisymmetric profile against the midplane, especially in the reverse-field pinches. A physical reasoning for the behavior of this toroidal flow is given in the following.

In an axisymmetric pinch, the toroidal plasma flow is

generated only by $\frac{\underline{j} \times \underline{B}}{c}$ force of the poloidal plane (i.e., $\frac{\underline{j}_{pol} \times \underline{B}_{pol}}{c}$), since the ∇p term does not have a toroidal component. The behavior of the toroidal flow shown in Figure 26(a) is directly connected to the fact that the current surfaces tend to shift more outward than the magnetic field surfaces as shown in the next figure. (In the infinite aspect ratio limit, these two surfaces would coincide. Thus, $\underline{j}_{pol} \times \underline{B}_{pol} = 0$ and no toroidal flow will occur.) Figure 27 shows the magnetic field lines (the solid lines) and the current lines (the dashed lines) on the poloidal plane at 9μs. The current lines appear to be more shifted outward than the magnetic field lines, and thus, $\frac{\underline{j}_{pol} \times \underline{B}_{pol}}{c}$ force antisymmetric against the midplane results. During the initial phase of the discharge, the poloidal current lines will be shifted approximately together with the plasma density, since the pinch time (∿1μs) is much shorter than the field diffusion time (∿10μs) and thus the toroidal magnetic field will be almost frozen in the plasma. On the other hand, the toroidal shift of the poloidal field lines will be slower, since the toroidal currents are continuously created at the wall and then carried in by convection and diffusion. These would be the reasons for the steep increase of the toroidal velocity at ∿2μs (Figure 26(a)) when the first pinching reaches its maximum.

At a later time, the toroidal velocity reaches a steady magnitude, indicating that the field and current lines on the poloidal plane approximately coincide (i.e., $\underline{j}_p \times \underline{B}_p \simeq 0$). The field convection due to the velocity is

$$\nabla \times (\underline{u} \times \underline{B}) = (B \cdot \nabla)\underline{u} - (\underline{u} \cdot \nabla)\underline{B} - \underline{B}(\nabla \cdot \underline{u}).$$

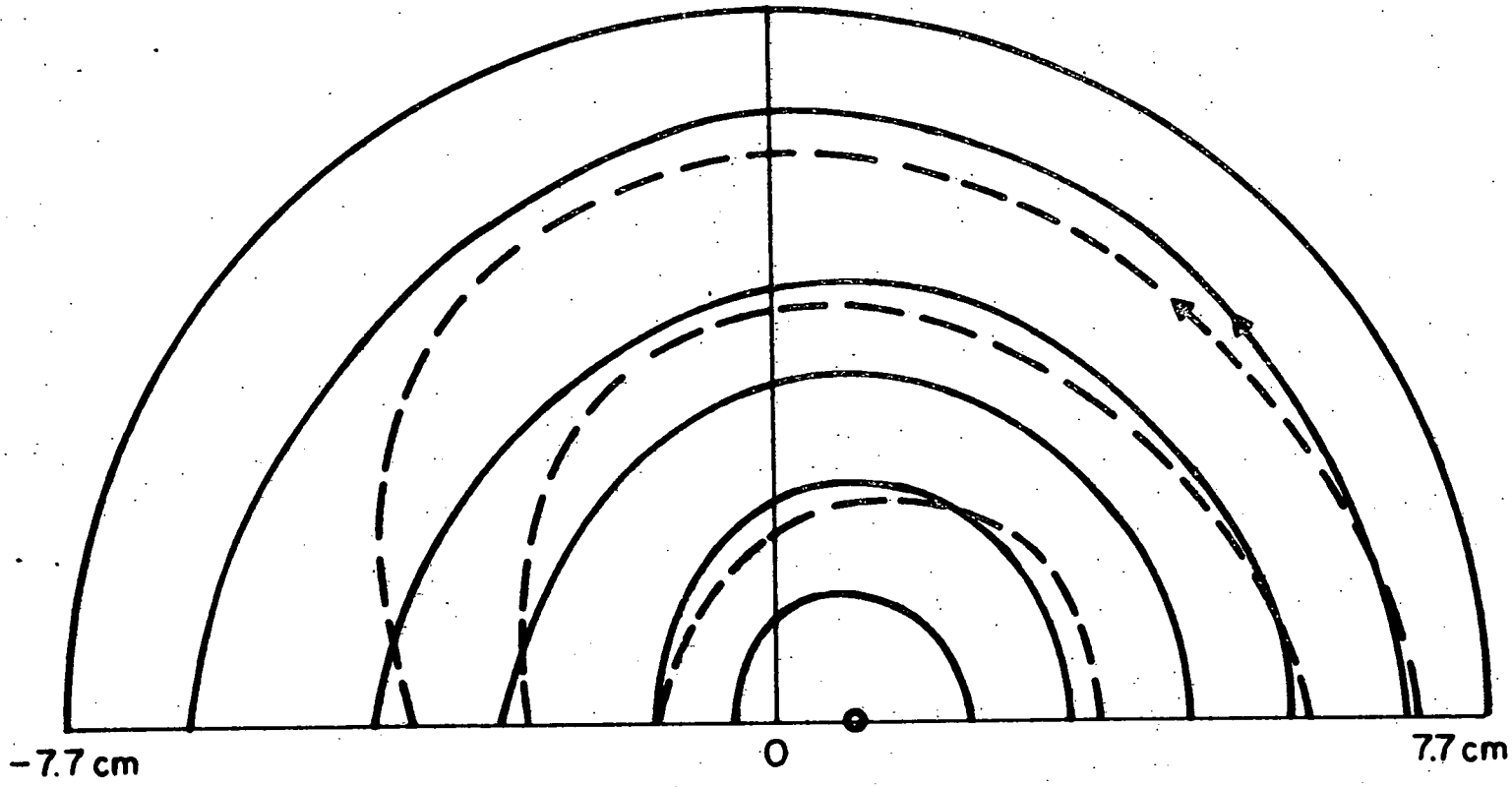

FIG. 27. MAGNETIC FIELD LINES(_____) AND THE CURRENT LINES(---------) ON THE POLOIDAL PLANE AT 9 μs.

With $\underline{u} = u_\phi \hat{\phi}$, this is $(B_p \cdot \nabla u_\phi - u_\phi B_R/R)\hat{\phi}$. Thus, the convection due to the toroidal flow will tend to shift the current surfaces more inward then the field surfaces. This effect must be balanced by some opposing effects to keep the field and current lines on the poloidal plane coincide. One of these opposing effects comes from the fact that much more toroidal currents are generated at the inside wall ($r = r_o$, $\theta = \pi$) than at the outside wall ($r = r_o$, $\theta = 0$). This is because the electric field at the inside wall is $\sim$50% stronger than at the outside wall due to $\sim$50% shorter loop length (aspect ratio = $\sim$5) and the same loop voltage. The generation of the toroidal current at the wall will occur throughout the discharge to offset the dissipation loss of total current, if the discharge is power-crowbarred. For a simply-crowbarred discharge, this effect will be also present in a lesser extent. The other opposing effect would come from the fact that the toroidal field reversal is $\sim$50% larger at the inside wall than at the outside wall. Thus, more dissipation of the toroidal field will occur at the inner part of the poloidal plane. Above two effects together will act to shift the current surfaces more outward than the magnetic field surfaces, thereby, balancing the field convection effect of the toroidal velocity.

A simpler explanation which is parallel to the previous one can be made as follows. The two effects described above, i.e., more toroidal currents generated at the inside wall, and more toroidal field dissipation at the inner part of the poloidal

plane, give a tendency to steepen the pitch of the magnetic field in the inner part of the poloidal plane while making the pitch less steep in the outer part. This tendency will be balanced by the field convection of the toroidal flow, as explained in the following figure. Figure 28 shows a helical magnetic field line and the directions of the toroidal plasma flow (by → or ←) as seen in the simulation. It is readily seen that the field convection of this toroidal flow would steepen the pitch of the magnetic field at the outside (drawn in dashed lines) while making the pitch less steep at the inside. This convection effect will balance the opposite effects previously described, so that the pitch angle remains nearly stationary.

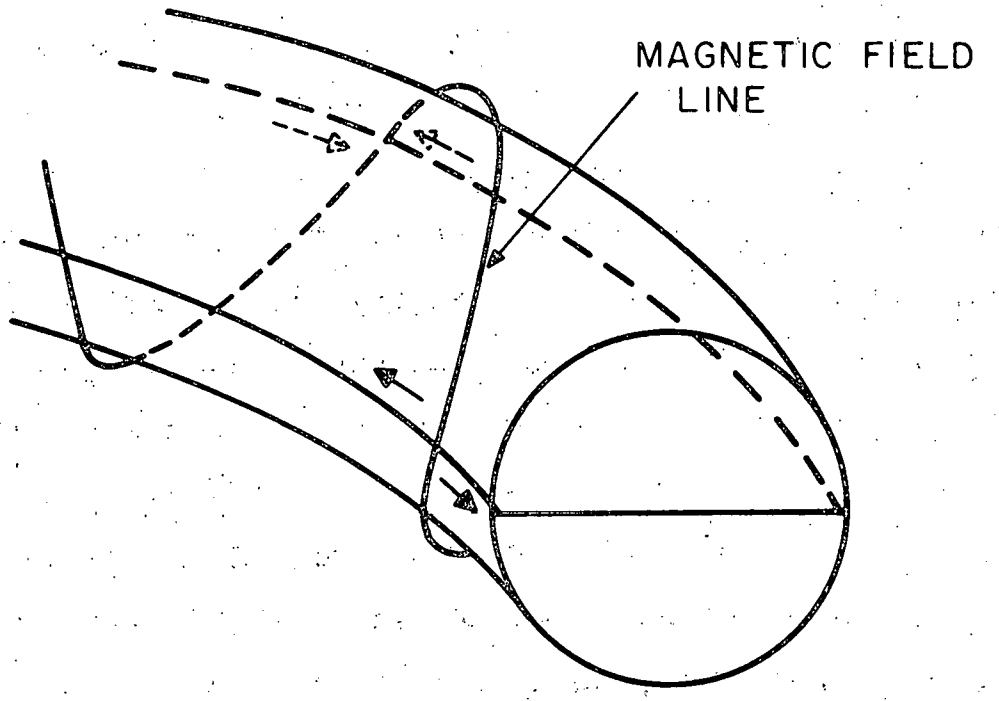

FIG. 28. A HELICAL MAGNETIC FIELD LINE AND THE DIRECTIONS OF THE VELOCITY (→ or ←) are depicted. THE VELOCITY IS ANTISYMMETRIC AGAINST THE MIDPLANE. FIELD CONVECTION DUE TO THE VELOCITY WILL STEEPEN THE FIELD PITCH AT THE OUTSIDE(DRAWN IN DASHED LINES), WHILE MAKE IT LESS STEEP AT THE INSIDE.

4.4 ZT-40 Reverse-Field Pinch

The ZT-40 experiment is a next generation reverse-field pinch, now being constructed in Los Alamos. The size will be about three times larger than ZT-S, with a 20cm minor radius and a 114cm major radius. Previous ZT-I and ZT-S experiments showed that nonideal effects due to plasma resistivity limit the stable time of the discharge. Thus, it is expected that the confinement time will be extended at least an order of magnitude since diffusion time scales as $\propto a^2/D$ (a = plasma radius; D = diffusion coefficient). This, and other scaling behaviors, will be studied with ZT-40 experiment in a size range unexplored by previous reverse-field pinches. This experiment will also yield information for design of a larger ZT-II experiment which will be projected to take the reverse-field pinch concept to $n\tau = 10^{13} - 10^{14}$ sec·cm^{-3} range.

Before studying the ZT-40, we will first examine the scaling of the mathematical model used (i.e., the dissipative magnetohydrodynamic equations (Eqs. 1)). This would give more insight to the scaling behavior of the experiments and also the three time scales, Alfven, field diffusion, and heat diffusion times, will be clearly defined in the course.

4.4.A. Scaling of the Equations

From the resistive magnetohydrodynamic equation (Eqs. 1), we obtain the following equations by neglecting the Hall term (which is a first-order effect in the inverse aspect ratio), eliminating the variables $\underline{E}$ and $\underline{j}$ and denoting $C_v T$ as $\tilde{T}$.

($\frac{D}{Dt}$ denotes $\frac{\partial}{\partial t} + (u\cdot\nabla)$ in the following.)

$$\partial\rho/\partial t + \operatorname{div}(\rho\underline{u}) = 0,$$

$$\rho\frac{D\underline{u}}{Dt} = -(\gamma - 1)\nabla(\rho\tilde{T}) + \frac{1}{4\pi}\operatorname{curl}\underline{B}\times\underline{B},$$

$$\rho\frac{D\tilde{T}}{Dt} = -(\gamma - 1)\rho\tilde{T}\operatorname{div}\underline{u} + \frac{1}{4\pi}(\operatorname{curl}\underline{B})^2\frac{c^2}{4\pi\sigma} + \operatorname{div}\frac{K}{C_v}\nabla\tilde{T},$$

$$\frac{\partial\underline{B}}{\partial t} = -\operatorname{curl}\left(\frac{c^2}{4\pi\sigma}\operatorname{curl}\underline{B} - \underline{u}\times\underline{B}\right). \tag{37}$$

The solution of these equations will be determined by the two coefficients $\frac{c^2}{4\pi\sigma}$ and $\frac{K}{C_v}$ in addition to the appropriate initial and boundary conditions. Thus, if the values of these two coefficients and the initial and boundary conditions are numerically identical in two different sets of length, mass and time units, the solutions will also be identical in the respective units. In other words, the problems so posed are mathematically equivalent.

The initial and boundary conditions of the present pinch experiments are easily scaled if we use the following length, mass and time units $[\ell_o, m_o, t_o]$, i.e., the torus minor radius r_o as a length unit ℓ_o, $\rho_o \times r_o^3$ (ρ_o: initial density) as a mass unit m_o and the Alfven time $\frac{r_o}{u_A} = \frac{r_o}{B_o/\sqrt{4\pi\rho_o}}$ (B_o: bias field) as a time unit t_o (which is equivalent to adopting $\frac{B_o}{\sqrt{4\pi}}$ as a magnetic field unit). For example, the wall is at $r = 1$, initial density 1 and bias field $\sqrt{4\pi}$ in these units. By inspecting the dimensionalities of the two coefficients $\frac{c^2}{4\pi\sigma}$ and $\frac{K}{C_v}$, we readily find the numeral values of these coefficients in

the given units, to be $\frac{c^2}{4\pi\sigma} \times \frac{t_o}{\ell_o^2} = \frac{t_o}{\tau_B}$ (the field diffusion time $\tau_B = \frac{4\pi\sigma r_o^2}{c^2}$) and $\frac{K}{C_v} \times \frac{\ell_o t_o}{m_o} = \frac{t_o}{\tau_H}$ (the heat diffusion time $\tau_H = \frac{C_v \rho_o r_o^2}{K}$).

As an example, the following table shows parameters for ZT-40 and ZT-S discharges which are mathematically equivalent assuming the dissipative MHD model with classical resistivity and constant thermal conductivity.

TABLE 2

	ZT-40	ZT-S	Typical ZT-S Operating Parameters
Filling gas	Deuterium	Deuterium	Deuterium
r_o	20cm	7.7	7.7
ρ_o	5×10^{-9} gm/cm^3	10×10^{-9}	5×10^{-9}
B_o	3kG	6	1
Izp max.	500kA	400	50
Rise time	10μs	2.5	2
T_o	10ev	15	2

The ZT-40 values are the expected typical operating parameters, while the ZT-S values are found from the equivalence condition discussed above. A typical operating parameter of ZT-S is also shown for comparison. The values ρ_o and B_o of ZT-S are found from the condition that $\frac{t_o}{\tau_B}$ and $\frac{t_o}{\tau_H}$ be the same as in the ZT-40 case. The values, r_o, ρ_o and B_o, then, define the units $[\ell_o, m_o, t_o]$ as described before. From these units, all other

parameters are found such that their numeral values in these units are the same as in the ZT-40 case. The two solutions for ZT-40 and ZT-S, thus, will be identical in the respective sets of units $[\ell_o, m_o, t_o]$. Further, we can expect that the experimental results of these two discharges would also be approximately equivalent, assuming the mathematical model is roughly valid for both ZT-40 and ZT-S. The information thus gained in the ZT-S experiment would be helpful to anticipate the behavior of a bigger experiment and be valuable for the design of the ZT-40. But, the ZT-S discharge with the above shown parameters would probably become unstable, due to the high total plasma current (thus, high drift velocity). It is reported that in the high current regime, Eta-Beta discharges became unstable.[22] In any case, by increasing the total current and the preionization temperature as much as possible and also appropriately adjusting the other parameters, one could study experimentally, the transition to a bigger size experiment.

4.4.B. Simulation Results

In this section, we present simulation results of a ZT-40 discharge with the parameters shown in table 2 of the previous section. The most important difference of the ZT-40 simulation from the previous smaller experiments (SP-1, ZT-I, and ZT-S) is the fact that the two ratios τ_A/τ_B and τ_A/τ_H (τ_A: Alfven time = t_o in the previous notation. τ_B, τ_H: field and heat diffusion time, respectively) are much smaller, due to the larger machine size and higher temperature. For this ZT-40 discharge, τ_A, τ_B, and τ_H are $\sim$1μs, $\sim$1000μs and $\sim$1000μs respectively, compared to $\tau_A = \sim$1μs, $\tau_B = \sim$10μs and $\tau_H = \sim$10μs in the previous experiments.

Since the allowable time steps in the simulation with a fixed number of grids are roughly proportional to the Alfven time ($\Delta t \sim \frac{1}{500}\tau_A$ for the present code with 17 × 12 grids in r and θ directions), it is almost prohibitive to simulate this ZT-40 discharge to $t = \sim\tau_B$, although it was acceptable for the previous cases. Thus, the present code should be used to simulate the discharge until the plasma reaches a quasi-equilibrium diffusion state (the damping time will be found later to be $\sim$10μs due to viscosity), and then a diffusion code[36,37] (where the inertia is neglected so that the allowable time steps are determined by the diffusion time) can take over and study the diffusion phase of the discharge. However, diffusion codes generally use a static equilibrium state as the initial condition, and may not be able to incorporate the convection effects due to the large toroidal flow present in the steady equilibrium

state obtained from the present code (cf. Section 4.3.B). One possible solution in this case would be to use a difference scheme which heavily damps the fast time oscillations but gives small dissipation to the slow time oscillations.

As discussed in Section (4.1), the time needed to reach a quasi-equilibrium state (the damping time) is $\sim\tau_B$, when the viscosity is small. Although in the previous smaller experiments, the viscous dissipation time $\tau_\nu = \frac{r_o^2}{\nu}$ was much longer than other time scales, τ_ν in the present case is much shorter than τ_B with $\tau_\nu = \sim 10\mu s$, due to higher temperature assuming classical viscosity (cf. Section 2.3). Thus, in the experiment, the damping time would be $\sim\tau_\nu$ ($\sim 10\mu s$). Therefore, the viscosity effect should be incorporated into the simulation for more accurate results. However, the error resulted from the neglection of the viscosity in the present code should be quite small, since the kinetic energy remains several orders of magnitude smaller than both the field energy and the thermal energy. (This is generally true in a reverse-field pinch where a strong bias field is present.) Thus, a small oscillation is still present at $t = 30\mu s$ in the following simulation, but the plasma state at this instant would be quite close to the actual quasi-equilibrium state.

Figure 29 shows the two field boundary conditions for the calculation. The toroidal plasma current rises to 500kA in $10\mu s$ and a bias field of 3kG is reversed at $10\mu s$. The filling gas is $\rho_o = 5 \times 10^{-9} gm/cm^3$ deuterium and the initial temperature 10ev. In Figure 30, the density profiles at 10, 20 and $30\mu s$

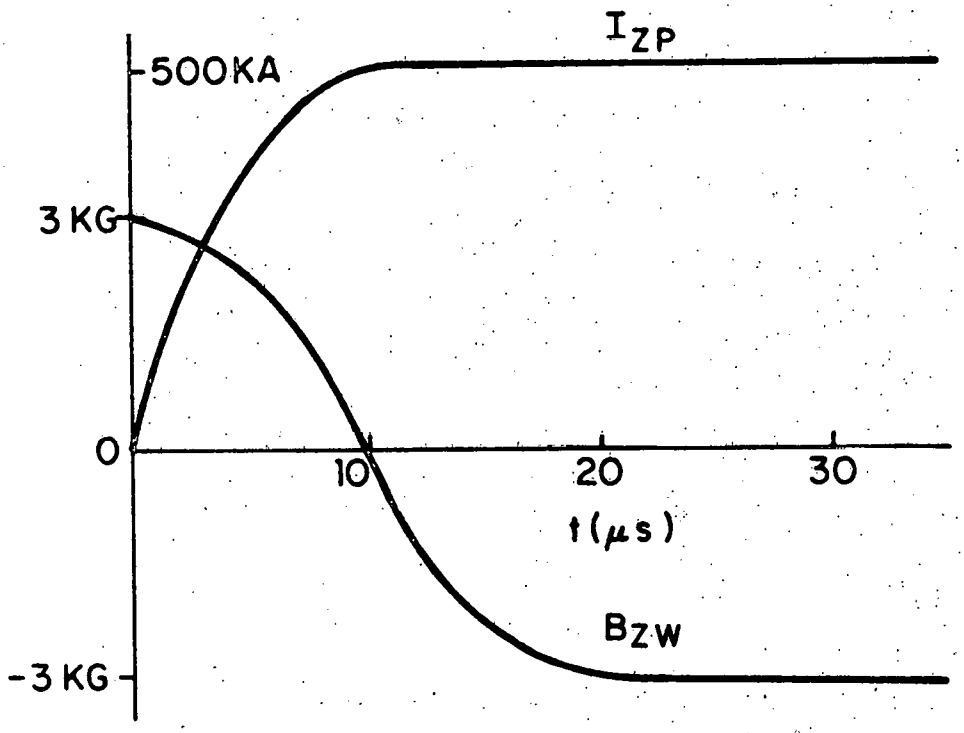

FIG. 29. TIME TRACES OF THE TOROIDAL MAGNETIC FIELD AT THE WALL AND THE TOROIDAL PLASMA CURRENT.

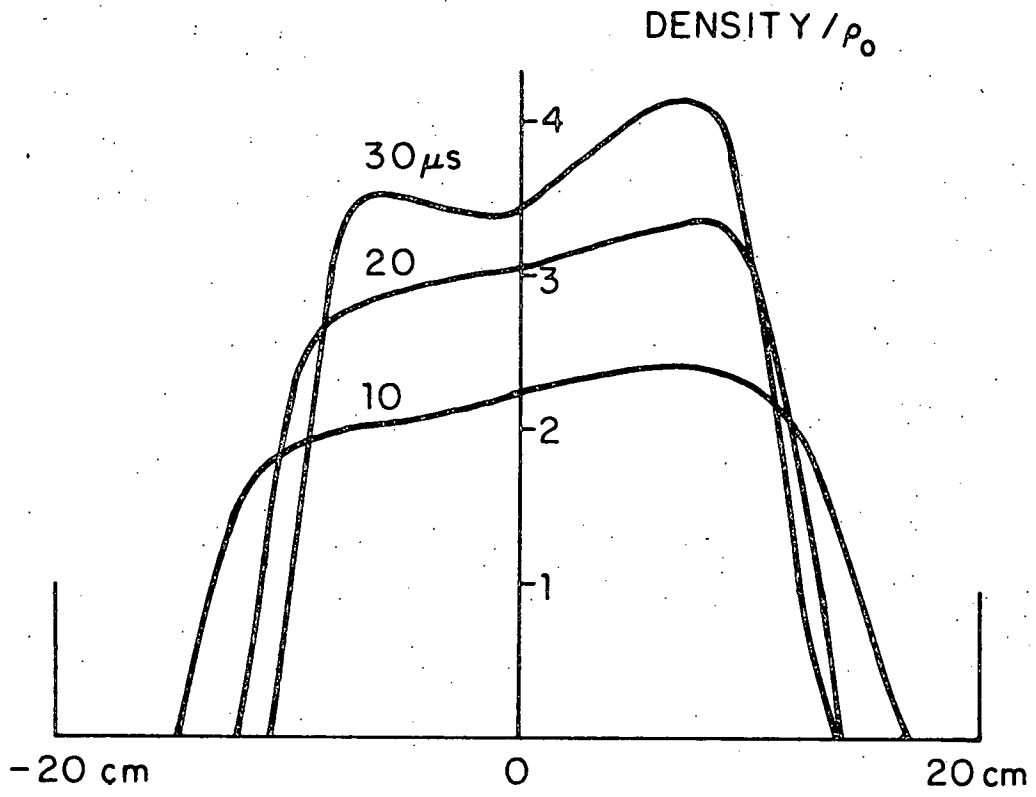

FIG. 30. DENSITY PROFILES (NORMALIZED TO THE INITIAL VALUE) AT 10, 20 and 30 μs.

are shown. As discussed previously, a small oscillation still remains at 30μs, but we will regard the plasma state at this instant as a close approximation of the actual quasi-equilibrium state. The density profile at 30μs shows a compression ratio of ∿2 as in the previously studied ZT-S discharge, but the present profile shows a much steeper transition between low density region to main plasma column compared to a corresponding profile of ZT-S (e.g., t = 4.6μs profile in Figure 19). This is because the current sheath is very thin compared to the machine radius in the present case as will be shown later.

Figure 31 shows the toroidal and poloidal field profiles at 10, 20, and 30μs. Most of the main plasma region remains essentially current-free, and a slow penetration of thin current sheath is seen. This is more obvious in Figure 32 where the toroidal and poloidal current density profiles are plotted. Considerable amount of current is present outside the main plasma region until the respective crowbar times (for the toroidal circuit at 10μs and for the poloidal circuit at 20μs), due to the applied loop voltage. After the circuits are crowbarred, the current sheath becomes very thin. This result is expected because the field diffusion time is ∿1ms in this discharge, and thus, the current penetration would be still very shallow at t = 30μs. (Small poloidal currents deep inside the main plasma region are visible at times, due to the toroidal field in this region perturbed by a compressional wave.)

One important question then, is how this thin current profile will change at a much later time when $t \rightarrow \tau_B$. The current profile may broaden subsequently and eventually become

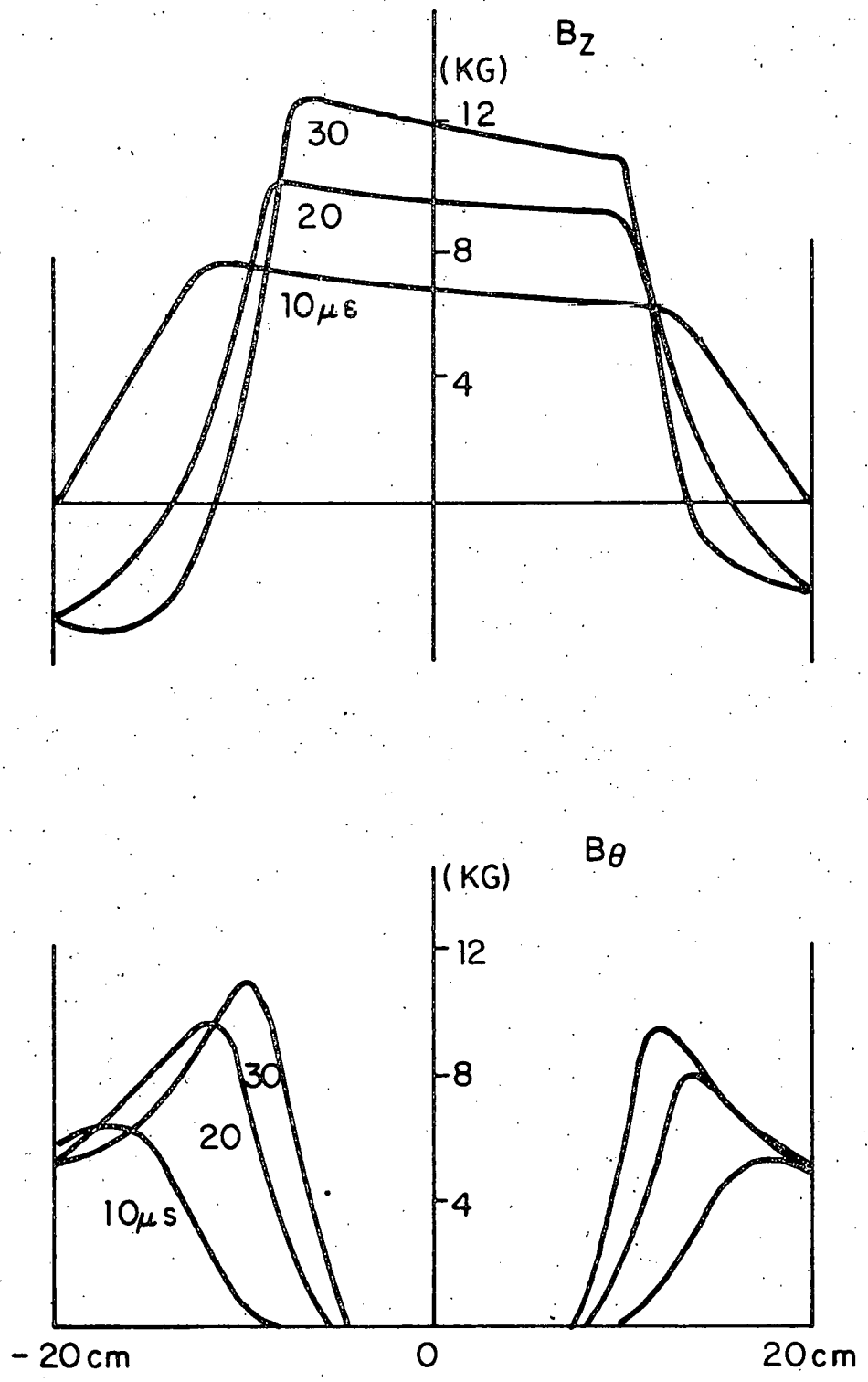

FIG. 31. TOROIDAL AND POLOIDAL FIELD PROFILES AT 10, 20 AND 30 μs.

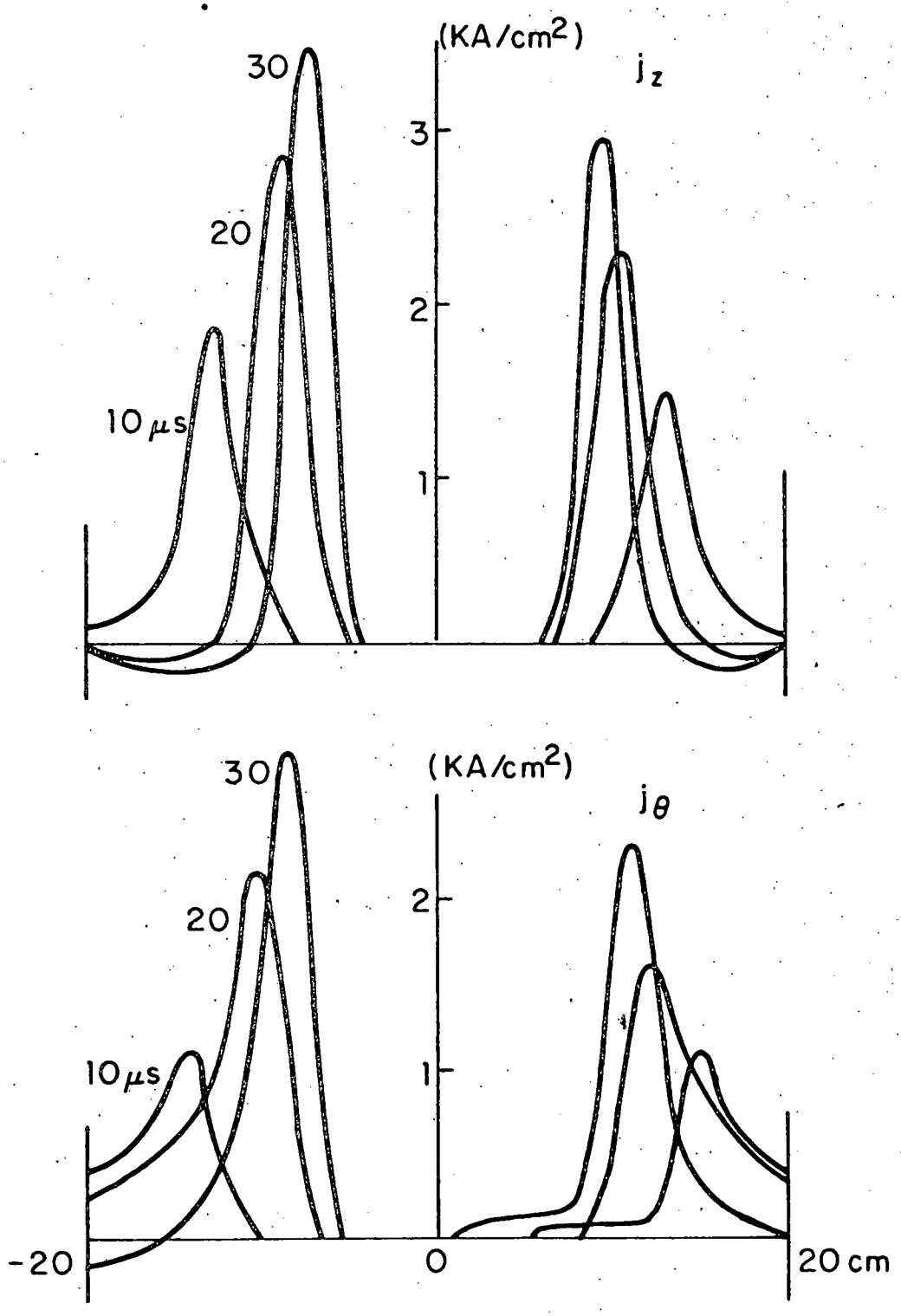

FIG. 32. TOROIDAL(j_z) AND POLOIDAL(j_θ) CURRENT DENSITY PROFILES AT 10, 20 and 30 μs.

a flat profile as seen in the ZT-S case (Figure 25). Or, the current profile may remain rather thin while it penetrates into the plasma. This question can be studied using a diffusion code. In any case, since the stability of a reverse-field pinch sensitively depends on the field profile, it would be highly valuable to be able to program desired field profiles by controlling the boundary conditions in the experiment. For a substantial programming of the field, it would be necessary to control the boundary conditions at least $\sim\frac{1}{10}\tau_B$. This is $\sim$100μs in the present case, and some difficulties may arise due to this long time scale. If we assume a simple field programming where the rise time of the current and the reversal time of the toroidal field are extended to $\sim$100μs, helical instabilities might develop and may result in a self-reversal of the toroidal field before the intended reversal time. Thus, the study of the self-reversal mode of operation might be more important than otherwise expected.

It is noted that a full dynamic code such as the present one would be necessary to study the field programming, even though this would require quite long computing time. This is because the convection effects will be substantial during the field programming, and thus, usual diffusion codes would not be suitable.

4.4.C. Confinement Characteristics

In this final section, we discuss some confinement characteristics of pinch experiments in general, when the size of the machine becomes large and the temperature high. (We mean by this, at least ZT-40 parameter range or higher.) The simulation results previously shown will be used for comparison.

As discussed in the previous section, one of the basic differences of the ZT-40 experiment from other smaller experiments is that the field diffusion time τ_B becomes much larger than Alfven time τ_A. The condition, $\tau_B >> \tau_A$, is a general character associated with a large size and high temperature, and thus, will be more pronounced when the experiment approaches the reactor regime. Similarly, the other fact that the damping time τ_{Damp} is much smaller than τ_B will be also true in general. For the ohmic heating to have any significance, the heat loss time τ_H must be at least comparable to τ_B. This would be accomplished in a large experiment by reduction of the line radiation, as a result of high temperature, and also by an improved vacuum technique. In the following study, we additionally assume a rather obvious fact that the rise time t_{rise} is also much shorter than τ_B in a large experiment. In short, the following conditions will hold, i.e., τ_A, τ_{Damp}, $t_{rise} << \tau_B \lesssim \tau_H$.

Therefore, a quasi-equilibrium dissipation state will be reached in a much shorter time scale (τ_{QE}) than τ_B. We now examine the mechanisms of force balance and the plasma β in this

initial quasi-equilibrium state. The poloidal field generally confines, while the toroidal field can either confine or repel. The other repelling force is the plasma pressure due to adiabatic compression of the initial pressure. The pressure contribution due to ohmic dissipation, at this moment, will be negligible because $\tau_{QE} << \tau_B$. Since the wall stabilization is generally important, the compression ratio is usually limited to $\sim$2. This limits the adiabatically compressed pressure at about ten times the initial pressure, independent of the machine size. Therefore, the plasma β at the initial quasi-equilibrium state of a large experiment will be quite low, unless the preionization temperature is made very high. For example, in the ZT-40 discharge studied in the previous section with the initial temperature of 10ev, the adiabatically compressed pressure accounts for less than 10% of the magnetic pressure. Therefore, the field profiles at 30μs in Figure 31 show quite low β, compared to the ZT-S profiles in Figure 23 which shows $\sim$50% β. This tendency will become more pronounced as the size of the machine becomes larger and the temperature higher, unless the preionization temperature can be made very high, which is an exceedingly difficult task. Then, we can conclude that at the initial quasi-equilibrium state of a large pinch experiment, the confining poloidal field should be nearly balanced by the repelling toroidal field. This low β initial quasi-equilibrium state will evolve to a later higher β quasi-equilibrium state as $t \rightarrow \tau_B$, due to ohmic dissipation. The thermal energy of

this later stage will be, at most, comparable to the poloidal field energy (i.e., the poloidal plasma beta $\beta_p \lesssim 1$), since the initial quasi-equilibrium condition (i.e., $P_{\text{poloidal field}} \simeq -P_{\text{toroidal field}}$) limits the dissipatable energy of the toroidal field at about the same level as the poloidal field energy. Thus, it is found that the condition $\beta_p \lesssim 1$ which is rather obvious for the reverse-field pinch is also true for other pinch experiments in general. This condition $\beta_p \lesssim 1$ is more stringent than the usual criterion from the equilibrium consideration, i.e., $\beta_p \lesssim$ aspect ratio. If $B_t >> B_p$, the plasma beta is thus limited at $\beta \sim \frac{B_p^2}{B_t^2}$. Therefore, to achieve a high β, the toroidal field must be comparable to the poloidal field, (i.e., the safety factor $q < 1$ for a reasonable aspect ratio). One special feature of the reverse-field pinch concept is that this condition is possible due to the magnetic shear stabilization, and this character, thus, will be more important as the size of the experiment becomes large.

It is noted that the above discussion will not hold when an auxiliary heating, such as neutral injection or rf heating is used with a heating time scale much shorter than τ_B. In such a case, the plasma confinement due to the toroidal field could be made much larger than the poloidal field contribution (i.e., $\beta_p >> 1$).

REFERENCES

1. H. C. Lui and C. K. Chu, Phys. Fluids 18, 1277 (1975).
2. W. Park, H. C. Lui and C. K. Chu, Bull. Am. Phys. Soc. 21, 1092 (1976).
3. J. C. Callen et al., Proc. 6th Conf. on Plasma Phys. and Contr. Nucl. Fusion Res., Berchtesgaden (1976) Vol. II, p. 369.
4. C. Bobeldijk et al., Proc. 3rd Conf. on Plasma Phys. and Contr. Nucl. Fusion Res., Novosibirsk (1968) Vol. I, p. 287.
5. D. A. Baker et al., Proc. 6th Conf. on Plasma Phys. and Contr. Nucl. Fusion Res., Berchtesgaden (1976) Vol. I, p. 419.
6. W. Park and C. K. Chu, Nucl. Fusion 17, 1100 (1977).
7. D. C. Robinson, Plasma Phys. 13, 439 (1971).
8. R. L. Hagenson and R. A. Krakowski, ANS 3rd Meeting on the Tech. of Control. Nucl. Fusion, Santa Fe (1978).
9. C. W. Gowers et al., Proc. 6th Conf. on Plasma Phys. and Nucl. Fusion Res., Berchtesgaden (1976) Vol. I, p. 429.
10. J. B. Taylor, Phys. Rev. Letters 33, 1139 (1974).
11. N. A. Krall and A. W. Trivelpiece, Principles of Plasma Physics (McGraw Hill, New York, 1973).
12. R. D. Richtmyer and K. W. Morton, Difference Methods for Initial Value Problems (Interscience, New York, 1967), 2nd ed.
13. W. K. H. Panofsky and M. Phillps, Classical Electricity and Magnetism (Addison-Wesley, Reading, 1964).
14. S. I. Braginskii, in M. A. Leontovich(ed.), Reviews of Plasma Physics, Vol. I (Consultant Bureau, New York, 1965).

15. H. Okuda, C. Chu and J. M. Dawson, Phys. Fluids 18, 243 (1975).

16. P. C. Liewer and N. A. Krall, Phys. Fluids 16, 1953 (1973).

17. R. Chodura, Nucl. Fusion 15, 55 (1975).

18. A. G. Sgro and C. W. Nielson, Phys. Fluids 19, 126 (1976).

19. E. P. Butt et al., Proc. 5th Conf. on Plasma Phys. and Contr. Fusion Res., Tokyo (1974) Vol. III, p. 417.

20. A. Buffa et al., Proc. 5th Conf. on Plasma Phys. and Contr. Fusion Res., Tokyo (1974) Vol. III, p. 431.

21. W. Marshall, Kinetic Theory of an Ionized Gas, Part 3, AERE T/R 2419 (1960).

22. A. Buffa et al., Proc. 6th Conf. on Plasma Phys. and Contr. Fusion Res., Berchtesgaden (1976) Vol. I, p. 447.

23. E. Isaacson and H. B. Keller, Analysis of Numerical Methods (John Wiley, New York, 1966).

24. A. Lapidus, J. Compt. Phys. 2, 154 (1967).

25. R. Courant and D. Hilbert, Methods of Math. Physics. (Interscience, New York, 1962) Vol. II.

26. C. K. Chu and A. Sereny, J. Comput. Phys. 15, 476 (1974).

27. M. N. Rosenbluth and A. N. Kaufmann, Phys. Rev. 109, 1 (1958).

28. K. Hain, G. Hain, K. V. Roberts, S. J. Roberts and W. Koppendorfer, Z. Naturforsh. A15, 1039 (1960).

29. J. P. Boris, A Physically Motivated Solution of the Alfven Problem, NRL Report 2167 (1970).

30. I. R. Lindemuth, Numerical Methods in the ANIMAL code, in Proc. of 7th Conf. on Numerical Simul. of Plasma, New York (1975).

31. C. Bobeldijk et al., Proc. 3rd Conf. on Plasma Phys. and Contr. Nucl. Fusion Res., Novosibirsk (1968) Vol. I, p. 287.

32. D. A. Baker et al., Proc. 5th Conf. on Plasma Phys. and Contr. Nucl. Fusion Res., Tokyo (1974) Vol. III, p. 35.

33. D. A. Baker, Los Alamos Scientific Laboratory, Private communication.

34. B. J. Green, Nucl. Fusion 12, 475 (1972).

35. R. B. White, Princeton Plasma Physics Laboratory, Private communication.

36. R. N. Byrne and C. K. Chu, Proc. 8th Conf. on Plasma Phys. and Contr. Nucl. Fusion Res., Innsbruck (1978) To appear.

37. G. Becker and D. F. Duchs, Nucl. Fusion 16, 763 (1976).

APPENDIX : Computer Program Listing

```
      BLOCK      DATA
CC
CC----  INPUT PARAMETERS (CGS GAUSSIAN UNITS)  ----------------------
CC
CC....EXECUTION, PLOTTING AND PRINTING
CC    MS : STOP EXEC IF CYCLE#>MS
CC    MW : PLOT AND PRINT IF MOD(CYCLE#,MW)=0
CC    MST : NO PLOT OR PRINT IF CYCLE#<MST
CC    MAA,MBB : IF MAA<CYCLE#<MBB, PRINT INFORM. ON
CC              PROCESS(IZP TO PSI(ID))(CF.SECTION 3.2.B)
CC    MBB : IF MBB=ODD, REDUCED PRINTING ON VARIABLES
CC
CC....MACHINE PARAM. AND GRID AND STEP SIZE
CC    RB : MAJOR RADIUS
CC    RSMA : MINOR RADIUS
CC    ID : # OF GRIDS IN R
CC    JD : # OF GRIDS IN THETA
CC    DDDT : TIME STEP SIZE
CC    ADDT,CHTIME : IF TIME>CHTIME, TIME STEP=DDDT+ADDT
CC    ADADT,CHCHTM : IF TIME>CHCHTM, TIME STEP=DDDT+ADDT+ADADT
CC
CC....INITIAL CONDITIONS
CC    DN : INITIAL DENSITY
CC    TEMINI : INITIAL TEMP. IN KELVIN
CC
CC....B. C. ; TOROIDAL CURRENT IZP
CC****(TMTM = TIME * 1.0E6 )*******
CC    CRTIMP, PETIMP, CURRR, PEP1, FS1, TMP1, CUR1, CU1BA :
CC    IZP(IN AMP.)= CURRR*SIN(PI*TMTM/PETIMP)
CC    IF TMTM>TMP1, IZP=CU1BA+CUR1*SIN(PI*(TMTM-FS1)/PEP1)
CC    IF TMTM>CRTIMP, IZP=CONSTANT
CC
CC....B. C. ; TOROIDAL MAGNETIC FIELD AT WALL,  BZW
CC    BTOR, BMIN, CRTIMX, PETIMX, PEPEX, OTIM, FSTIMX, BIAS, TMX2, OTM2 :
CC    BZW = BIAS + BTOR*COS(PI*(TMTM+FSTIMX)/PETIMX)
CC    IF TMTM>OTIM, BZW=-BMIN*SIN(PI*(TMTM-OTIM)/PEPEX)
CC    IF TMTM>TMX2, BZW=-BMIN*EXP(-(TMTM-TMX2)*OTM2)
CC    IF TMTM>CRTIMX, BZW=CONSTANT
CC
CC....TRANSPORT COEFFICIENTS (CF. SECTION 2.3)
CC    ECONC : CLASSICAL ELECTRIC CONDUCTIVITY AT 1 EV
CC    CHOF : F*1.51E-8/SQRT(MASS OF ATOM)  (CF. EQ.9, SECTION 2.3)
CC    CHOC : C*6.7E-18/SQRT(MASS OF ATOM)  (CF. EQ.9, SECTION 2.3)
CC    CNCON : CONSTANT THERMAL CONDUCTIVITY (IN ERG.CM**2/KELVIN)
CC    BOWW,POW : IF TMTM>BOWW, ANOMAL.CONDUC.=POW*ANOMAL.CONDUC.
CC               (WITH POW>>1, ELECTRIC CONDUC. BECOME PURE CLASSICAL)
CC    BOWW,GAP : IF TMTM>BOWW, THERMAL CONDUC.=GAP
CC
CC....NUMERICAL DISSIPATION
CC    DISS : KAPPA IN EQ.(11+), SECTION 2.3
CC    PPOWW : THETA IN EQ.(10'), SECTION 3.1
CC    OPERA : IF TMTM>OPERA, DISS AND PPOWW BECOME 0.0
CC
CC....LOW DENSITY REGION
CC    HU : FLOOR DENSITY = HU*DN
CC
CC....FILLING GAS PARAM.
CC    FR : BOLTZMANN CONST./AVERAGE MASS PER PARTICLE(INCLUDING ELECTRONS)
CC    FK : GAS CONST. GAMMA
CC    DNUM : # OF ATOMS PER 1 GM
```

```
61    CC
62    CC....ALGORITHM FOR DETERMINING PSI(ID) FROM TOROIDAL PLASMA CURRENT
63    CC     (CF. SECTION 3.2.B)
64    CC     FFLUXS : INITIAL START FOR PSI(ID) (FIRST 10 TIME STEPS)
65    CC                PSI(ID) = FFLUXS*SIN(PI*TMTM/PETIMP)
66    CC     BOW, PPOW, SDMM, PPPOW, CURL, CURLL :
67    CC     (AFTER 10 TIME STEPS)
68    CC     (NOTATIONS : PSINC(INCREAMENT OF PSI(ID) AT NEW TIME STEP),
69    CC                  PSIPRE(INCREAMENT AT OLD TIME STEP),
70    CC                  TCUR(TORO CURRENT AT OLD STEP),TTCUR(CURRENT AT 2 TIME
71    CC                  STEPS BEFORE), TTTCUR(CURRENT AT 3 TIME STEPS BEFORE),
72    CC                  SURCUR((TCUR+TTCUR)/2-TARGET CURRENT), DT(NEW TIME STEP SIZE),
73    CC                  DTPRE(PREVIOUS TIME STEP SIZE),
74    CC                  PSIN10(PSINC AT 10TH TIME STEP))
75    CC     SDM = ABS(SURCUR/CURRR)**0.5*PSIN10*SDMM
76    CC     IF TMTM>1.5*CRTIMP, SDM=SDM*PPPOW
77    CC     IF SURCUR>CURL OR <CURLL, SDM=SDM*BBOW
78    CC     PSINC = SURCUR/ABS(SURCUR)*ABS(PSIPRE)*
79    CC            ABS(SURCUR/(TTTCUR-TCUR)/BOW)**PPOW*DT/DTPRE
80    CC     PSIMAX=PSIPRE*DT/DTPRE+SDM*DT
81    CC     PSIMIN=PSIPRE*DT/DTPRE-SDM*DT
82    CC     PSINC = AMIN1(PSINC,PSIMAX)
83    CC     PSINC = AMAX1(PSINC,PSIMIN)
84    CC
85    CC....NOT USED
86    CC     DIVID, GAPTM
87    CC
88    CC
89          COMMON/YY/MS,MW,MST,ID,JD,MAA,MBB,PPOW,SDMM,CNCON,CURRR,BOW
90         1,BMIN,BTOR,RB,RSMA,HU,DN,DDDT,FFLUXS,DIVID,OPERA,FR,FK
91         2,CURL,PPPOW,BBOW,CURLL,PPOWW,BOWW,POW,ECONC,DNUM,CHOF,CHOC
92         3,ADDT,ADADT,CHTIME,CHCHTM,GAP,TEMINI,GAPTM
93         4,CRTIMP,CRTIMX,PETIMP,PETIMX,PEPEX,OTIM,FSTIMX
94         5,PEP1,FS1,TMP1,CUR1,CU1BA,TMX2,OTM2,DISS,BIAS
95          DATA MS,MW,MST/0200,100,001/
96         1,ID,JD,DDDT/16,9,010.0E-9/
97         2,GAP,ADDT,ADADT,CHTIME,CHCHTM/2.0E5,-5.E-9,20.E-9,6.E-6,50.E-6/
98         2,BMIN,BTOR,RB,RSMA/0620.0,0850.0,40.0,07.7/
99         3,MAA,MBB/0001,1500/
100        4,CNCON,SDMM,CURRR,PPOW,BOW/2.0E6,0.6000,6.0E4,0.30,2.0/
101        5,CURL,PPPOW,BBOW,POW/10.0E2,0.5,2.000,100000.0/
102        5,CURLL,PPOWW,BOWW,ECONC/-10.0E2,0.1    ,6.0,1.30E13/
103        5,DIVID,DN,FFLUXS,FR,FK/1.00000,4.3E-9,11.00E4,08.310E7,1.666666/
104        5,DNUM,CHOF,CHOC/3.00E23,4.15E4,1.84E-6/
105        6,HU,OPERA/0.10    ,60.00/
106        7,CRTIMP,CRTIMX/9.0,9.0/
107        7,PETIMP,PETIMX,PEPEX/18.0,6.0,10.0/
108        7,OTIM,FSTIMX,BIAS,TEMINI,GAPTM/100.0,9.0,400.0,1.2E4,100.0/
109        7,PEP1,FS1,TMP1,CUR1/6.00,0.6,100.0,6.0E3/
110        7,CU1BA,TMX2,OTM2,DISS/5.1E4,100.0,0.073,0.125/
111         END
112   C
113   C
114   C.....MAIN PROGRAM .....................................
115   C
116         DIMENSION PSI(20,16,2),B1(20,16,2),B2(20,16,2),XI(20,16,2),
117        1C1(20,16,2),C2(20,16,2),C3(20,16,2),T(20,16,2),
118        2W(4,20,16,3),F(4,20,16,3),E!(20,16,2),B3(20,16,2),SR(20),
119        4GA(20,16),GB(20,16),GC(20,16),GD(20,16),CN(20,16,2),
120        5AA(90,12),BB(4,4),ANG(16),BATB(20),ALAM(20,16)
```

```
      6,VELD(20,16),AJOR(20,16),AJPE(20,16),VINT(20,16)
       COMMON PSI,B1,B2,B3,XI,C1,C2,C3,T,W,F,SR,ANG,BATB
      1,GA,GB,GC,GD,CN,EI,AA,BB,AJCON
       COMMON/YY/MS,MW,MST,ID,JD,MAA,MBB,PPOW,SDMM,CNCON,CURRR,BOW
      1,BMIN,BTOR,RB,RSMA,HU,DN,DDDT,FFLUXS,DIVID,OPERA,FR,FK
      2,CURL,PPPOW,BBOW,CURLL,PPOWW,BOWW,POW,ECONC,DNUM,CHOF,CHOC
      3,ADDT,ADADT,CHTIME,CHCHTM,GAP,TEMINI,GAPTM
      4,CRTIMP,CRTIMX,PETIMP,PETIMX,PEPEX,OTIM,FSTIMX
      5,PEP1,FS1,TMP1,CUR1,CU1BA,TMX2,OTM2,DISS,BIAS
        COMMON/WX/X(40),FVL(40,6)
       DIMENSION  SJA(16),THJ(16),SEQ1(16),SEQ2(16)
      1           ,SEQ5(16),SEQ6(16),SEQ7(16),SEQ8(16)
      2  ,SEQ10(16),BMS(16),URR(16),UTH(16),UFI(16),WCO(16),WSI(16)
      3 ,TVA1(100),TVA2(100),TVA3(100),XNL(100),TVA4(100),TVA5(100)
      4 ,TVA6(100)
       COMMON/XY/NUG,DX,JE,JB,PI,IE,THJ
CC
CC....VARIABLES ..............................
CC    W(1,I,J,K) : DENSITY/'DN'
CC    W(N,I,J,K) : RADIAL(N=2), THETA(N=3) AND TOROIDAL(N=4)
CC                 VELOCITIES/'UN'    (UN=BTOR/SQRT(4PI*DN))
CC    EI : TEMPERATURE /'UN**2/CV'    (CV:SPECIFIC HEAT)
CC    PSI : POLOIDAL FLUX FUNCTION /'BTOR*RSMA**2'
CC    XI : R*B3 /'RSMA*BTOR'
CC    B1,B2,B3 : RADIAL, THETA AND TOROIDAL MAG. FIELD /'BTOR'
CC    C1,C2,C3 : RADIAL, THETA AND TOROIDAL CURRENT DENSITIES /
CC                '4PI*RSMA/C/BTOR'
CC    T : ELECTRICAL CONDUCTIVITY / INITIAL VALUE
CC    CN : THERMAL CONDUCTIVITY /'DN*RSMA*UN*CV'
CC
      OPTIMIZE
      WZIN=0.
      WTFIN=0.
      WRRR=0.
 FBKP CONTINUE
      CALL KEEP80(1,2)
      CALL DD80ID(9HPLOT TES ,1)
      IS=1
      JS=1
      IB=IS+1
      JB=JS+1
      IE=ID-1
      JE=JD-1
      JP=JE-JS
      IP=IE-IS
      RRSM=RSMA
      RSMA=RSMA*2.0*IE/(2.0*IE-1.0)
      TCUR=1.0
      TTCUR=2.0
      TTTCUR=3.0
      PI=3.1415926536
      UN=BTOR/SQRT(4.*PI*DN)
      DDDDT=DDDT     *UN/RSMA
      ANORTM=           UN/RSMA
      ADDT=ADDT     *UN/RSMA
      ADADT=ADADT    *UN/RSMA
      CHTIME=CHTIME    *UN/RSMA
      CHCHTM=CHCHTM    *UN/RSMA
      FLUXS=FFLUXS  /BTOR/RSMA/RSMA
      FLNOR=        BTOR*RSMA*RSMA
```

```
      PSINC=0.0
      PSIN10=0.0
      SMALL=1.0E-16
      TMALL=SMALL**2
      CV=FR/(FK-1.)
      TNOR=UN*UN/CV
      C=2.9980E+10
      AJNOR=C*BTOR/(4.0*PI*RSMA)
      K=1
      Q=RSMA/RB
      DCA=PI        /(JD-3.0)
      AJCON=C*1.67E-24*UN/BTOR/RSMA/4.0E-10
      DDT=0.1E-10 *UN/RSMA
      M=0
      DX=1./(ID-1.0)
      DO 333  I=IS,ID
      SI=I
      SR(I)=(SI-1.)*DX
  333   CONTINUE
      SGO=ECONC    *(TEMINI/11600.)**1.5
  101 FORMAT(1H ,"I=",I4,"RADIUS=",E14.7)
      DO 4  J=JS,JD
      SJ=J
      ANG(J)=(SJ-2.)*DCA
      WRITE (6,102) J,ANG(J)
    4 CONTINUE
  102 FORMAT (1H ,"J=",I4,"ANGLE=",E14.7)
      COK=DN*RSMA*UN*CV
CC
CC....INITIAL CONDITIONS
      DO 5 K=1,2
      DO  5  I=IS,ID
      DO  5  J=JS,JD
      PSI(I,J,K)=0.0
      XI(I,J,K)=COS(PI*FSTIMX/PETIMX)/Q+BIAS/BTOR/Q
      EI(I,J,K)=TEMINI*CV/UN/UN
      CN(I,J,K)=CNCON                    /COK
      T(I,J,K)=1.
      B1(I,J,K)=0.
      B2(I,J,K)=0.
      B3(I,J,K)=XI(I,J,K)/(1./Q+SR(I)*COS(ANG(J)))
      C1(I,J,K)=0.
      C2(I,J,K)=0.
      C3(I,J,K)=0.
      W(1,I,J,K+1)=1.0
      W(2,I,J,K+1)=0.
      W(3,I,J,K+1)=0.
      W(4,I,J,K+1)=0.
      W(1,I,J,K)=1.0
      W(2,I,J,K)=0.
      W(3,I,J,K)=0.
      W(4,I,J,K)=0.
    5 CONTINUE
CC
CC
      NUG=2*(JE-JB)
      DO 901 J=JS,JD
      THJ(J)=(J-JS-1)*2.0*PI/NUG
      SJA(J)=1.0+ Q*DX *COS(THJ(J))/2.0
  901  CONTINUE
```

```
241         DO 621 I=IS,ID
242         DO 621 J=JS,JD
243         VINT(I,J)=(B1(I,J,1)**2+B2(I,J,1)**2+B3(I,J,1)**2)/8./PI
244     621 CONTINUE
245         CALL VOLIN(VINT,WBOR,RB,RSMA)
246         WTIN=WBOR*BTOR*BTOR
247         DO 630 I=IS,ID
248         DO 630 J=JS,JD
249         VINT(I,J)=1.0
250     630 CONTINUE
251         CALL VOLIN(VINT,VOLU,RB,RSMA)
252         DO 625 J=JS,JD
253         UTH(J)=1.0
254     625 CONTINUE
255         CALL SURIN(UTH,SURA  ,RB,RSMA)
256         WRITE(6,631)VOLU,SURA,AJCON
257     631 FORMAT(1P7E14.6)
258         TIME=0.
259         RMTM=0.0
260       6 M=M+1
261         IF(RMTM.GT.OPERA)DISS=0.0
262         IF(RMTM.GT.OPERA)PPOWW=0.0
263         IF(RMTM.LE.BOWW)GO TO 38
264         DO 37 I=1,ID
265         DO 37 J=1,JD
266         CN(I,J,1)=GAP/COK
267         CN(I,J,2)=GAP/COK
268      37 CONTINUE
269      38 CONTINUE
270         TIMPRE=TIME
271         K=1
272     CC
273     CC....B. C. ; TOROIDAL CURRENT (CF. SECTION 3.2.B)
274         IF(M .EQ. 10)PSINC=FLUXS*SIN(PI*RMTM/PETIMP)
275        1 -FLUXS*SIN(PI*(RMTM-DDDDT*1.0E6/ANORTM)/PETIMP)
276         PSIPR=PSINC
277         DT=DDDDT
278         DTPRE=DT
279         IF (TIME .GT. CHTIME) DT=DDDDT+ADDT
280         IF (TIME .GT. CHCHTM) DT=DDDDT+ADDT+ADADT
281         DO 3  I=IS,ID
282         SI=I
283         SR(I)=(SI-1.)*DX
284         IF (I .EQ. IS) GO TO 3
285         BATB(I)=DT/(2.*SR(I)*DCA)
286       3 CONTINUE
287         BATA=DT/(2.*DX)
288         COE= C*C*DT/(4.*PI*RSMA*UN*SGO)
289         TIME=TIME+DT
290         RMTM=TIME/ANORTM *1.0E6
291         TIMINC=(TIME-TIMPRE)/ANORTM
292         IF (RMTM .GT. CRTIMP) GO TO 990
293         SURCUR=(CURRR *SIN(PI*RMTM/PETIMP)+(TCUR+TTCUR)*0.5)
294         IF(RMTM.GT.TMP1)SURCUR=CU1BA+(CUR1*SIN(PI*(RMTM-FS1)/PEP1)+(TCU
295        1R+TTCUR)*0.5)
296         PSINC=SIGN(1.0,SURCUR)*ABS(PSINC)*ABS(SURCUR/(TTTCUR-TCUR)/BOW)
297        1 **PPOW*DT/DTPRE
298         TCURMA=TCUR
299         GO TO 809
300      990 CONTINUE
```

```
      SURCUR=-TCURMA          +(TCUR+TTCUR)*0.5
      PSINC=SIGN(1.0,SURCUR)*ABS(PSINC)*ABS(SURCUR/(TTTCUR-TCUR)/BOW)
     1 **PPOW*DT/DTPRE
  809 CONTINUE
      IF(M .EQ. 10)PSIN10=PSIPR/DDDT
      SDM=ABS(SURCUR/CURRR)**0.5*SDMM*PSIN10
      IF(RMTM.GT.1.5*CRTIMP)SDM=ABS(SURCUR/CURRR)**0.5*PPPOW*SDMM*PSIN10
      IF(SURCUR.GT.CURL   .OR. SURCUR.LT.CURLL)SDM=SDM*BBOW
      PSIMA=PSIPR*DT/DTPRE+SDM*DT/ANORTM
      PSIMI=PSIPR*DT/DTPRE-SDM*DT/ANORTM
      BZAX=B3(1,2,1)*BTOR
      IF(M.EQ. MAA+1)WRITE(6,550)
  550 FORMAT(1H0,4X,"CYCLE",2X,"PSI(ID)",7X,"EST PSINC",1X,"ACT PSINC"
     1 ,1X,"TORO CUR",2X,"CUR ERROR",1X,"PSIMAX",4X,"PSIMIN",4X,
     2 "DENS AXIS",1X,"BZ AXIS",3X,"TIME")
      IF(M.GT.MAA.AND.M .LT.MBB )WRITE(6,807)M, PSI(ID,5,K),PSINC,PSIPR
     1,TCUR,SURCUR,PSIMA,PSIMI,W(1,1,2,1),BZAX,RMTM
      PSINC=AMIN1(PSINC,PSIMA)
      PSINC=AMAX1(PSINC,PSIMI)
  807 FORMAT("PSINC",I5,1PE14.6,10E10.2)
      DO 9 J=JS,JD
      PSI(ID,J,K+1)=PSI(ID,J,K)+PSINC
      IF(M.LT.10)PSI(ID,J,K+1)=FLUXS*SIN(PI*RMTM/PETIMP)
    9 CONTINUE
  991 CONTINUE
CC
CC....B. C. ; TOROIDAL FIELD AT WALL
      IF(RMTM.GT.CRTIMX)GO TO 900
      DO 999 J=JS,JD
      XI(ID,J,K+1)=
     1 COS(PI*(RMTM       +FSTIMX)/PETIMX)/Q +BIAS/BTOR/Q
      IF (RMTM .GT. OTIM  ) XI(ID,J,K+1)=-(BMIN/BTOR)*
     1     SIN(PI*(RMTM-OTIM)/PEPEX)/Q
      IF(RMTM.GT.TMX2)XI(ID,J,K+1)=-(BMIN/BTOR)*EXP(-(RMTM-TMX2)*OTM2)/Q
  998 CONTINUE
  999 CONTINUE
CC
CC....COORDINATE ORIGIN TREATMENT (CF. SECTION 3.2.B)
  900 SUM=0.
      SUN=0.
      TUM=0.
      VELO=0.0
      CL=0.
      DO 23 J=JB,JE
      DL=2.
      IF (J .EQ. JB .OR. J .EQ. JE) DL=1.
      CL=CL+DL
      SUM=SUM+(C*C/(4.*PI*RSMA*UN*SGO)*C3(IB,J,K)/T(IB,J,K)+
     1(W(2,IB,J,K)/W(1,IB,J,K)*B2(IB,J,K)-W(3,IB,J,K)/W(1,IB,J,K)*
     2B1(IB,J,K)))*DL
      SUN=SUN+(C*C/(4.*PI*RSMA*UN*SGO)*C2(IB,J,K)/T(IB,J,K)+
     1(W(4,IB,J,K)/W(1,IB,J,K)*B1(IB,J,K)-W(2,IB,J,K)/W(1,IB,J,K)*
     2B3(IB,J,K)))*DL
      TUM=TUM+EI(IB,J,K)*DL
      VELO=VELO+(W(2,IB,J,K)*COS(ANG(J))-W(3,IB,J,K)*SIN(ANG(J)))*
     1  SJA(J)*DL
   23 CONTINUE
      SUM=SUM/CL
      TUM=TUM/CL
      VELO=VELO/CL
```

```
      DO 30 I=IS,ID
      W(1,I,JE+1,K  )= W(1,I,JE-1,K  )
      W(2,I,JE+1,K  )= W(2,I,JE-1,K  )
      W(3,I,JE+1,K  )=-W(3,I,JE-1,K  )
      W(4,I,JE+1,K  )=-W(4,I,JE-1,K  )
      W(1,I,JB-1,K  )= W(1,I,JB+1,K  )
      W(2,I,JB-1,K  )= W(2,I,JB+1,K  )
      W(3,I,JB-1,K  )=-W(3,I,JB+1,K  )
      W(4,I,JB-1,K  )=-W(4,I,JB+1,K  )
   30 CONTINUE
      DO 902 J=JS,JD
      WCO(J)=COS(THJ(J))
      WSI(J)=SIN(THJ(J))
      URR(J)=W(2,IB,J,K)/W(1,IB,J,K)
      ALF=1.0/ Q
      SEQ1(J)=-(W(2,IS,J,K)+W(2,IB,J,K))*SJA(J)
      SEQ2(J)=-((W(2,1,J,K)**2/W(1,1,J,K)+W(2,2,J,K)**2/W(1,2,J,K))*
     1 WCO(J)-(W(2,1,J,K)*W(3,1,J,K)/W(1,1,J,K)+W(2,2,J,K)*W(3,2,J,K)/
     1 W(1,2,J,K))*WSI(J))*SJA(J)
     2  -(FK-1.0)*W(1,IB,J,K)*EI(IB,J,K)*WCO(J)
      SEQ6(J)= XI(IB,J,K)*WCO(J)        /ALF
      SEQ7(J)=-B2(IB,J,K)
      SEQ8(J)=-EI(IB,J,K)*W(2,IS,J,K)/W(1,IS,J,K)
     1  -(FK-1.0)*EI(IS,J,K)*URR(J)*SJA(J)
     2  +(CN(IS,J ,K)+CN(IB,J,K))*(EI(IB,J,K)-EI(IS,J,K))*(SJA(J)+1)
     2   /(W(1,IS,J,K)*DX*2.0)
      SEQ10(J)=PSI(IB,J,K)        *WCO(J)/ALF
  902 CONTINUE
      CALL AVERA(SEQ1,AVV1)
      CALL AVERA(SEQ2,AVV2)
      CALL AVERA(SEQ6,AVV6)
      CALL AVERA(SEQ7,AVV7)
      CALL AVERA(SEQ8,AVV8)
      CALL AVERA(SEQ10,AVV10)
      DO 905 J=JS,JD
      C1(IS,J,K)=           AVV6*WSI(J)
      C2(IS,J,K)=           AVV6*WCO(J)
      C3(IS,J,K)=AVV7
      B1(IS,J,K)=              AVV10*WSI(J)
      B2(IS,J,K)=              AVV10*WCO(J)
      B3(IS,J,K)= XI(IS,J,K)*Q
  905 CONTINUE
      AVV2=AVV2+C3(1,2,K)*B2(1,2,K)-C2(1,2,K)*B3(1,2,K)
      W(2,IS,2,K+1)=W(2,1,2,K)+DT*AVV2
      DO 24 J=JS,JD
      XI(IS,J,K+1)=XI(IS,J,K)+DT*DCA*SUN/(PI*DX)/Q
      W(1,IS,J,K+1)=W(1,1,J,K)+DT*AVV1
      W(2,IS,J,K+1)=W(2,IS,2,K+1)*WCO(J)
      W(3,IS,J,K+1)=-W(2,IS,2,K+1)*WSI(J)
      EI(IS,J,K+1)=COE*(C1(IS,J,K)**2+C2(IS,J,K)**2+C3(IS,J,K)**2)
     1  /(DT*T(IS,J,K)*W(1,IS,J,K))
      EI(IS,J,K+1)=AVV8+EI(IS,J,K+1)
      EI(IS,J,K+1)=TUM
      PSI(IS,J,K+1)=W(2,IS,J,K)*B2(IS,J,K)/W(1,IS,J,K)
     1-W(3,IS,J,K)*B1(IS,J,K)/W(1,IS,J,K)
      PSI(IS,J,K+1)=-COE*C3(IS,J,K)/(DT*T(IS,J,K))*ALF-ALF*PSI(IS,J,K+1)
      PSI(IS,J,K+1)=PSI(IS,J,K  )+DT*PSI(IS,J,K+1)
   24 CONTINUE
CC
CC
```

```
421         DO 28 J=JB,JE
422         DO 29 L=1,4
423         W(L,ID,J,K  )= W(L,IE,J,K  )
424      29 CONTINUE
425         B1(ID,J,K)=0.0
426         C1(ID,J,K)=-C1(IE,J,K)
427         C2(ID,J,K)= C2(IE,J,K)
428         C3(ID,J,K)= C3(IE,J,K)
429      28 CONTINUE
430         K=1
431         K2=1
432         K3=1
433         K4=1
434   CC
435   CC....FIND (S+F)/2  (S AND F IN EQ.8, SECTION 2.1)
436         DO 433 J=JB,JE
437         DO 434 I=IB,IE
438         F(1,I,J,K2)=(-(W(1,I,J,K2)/W(1,I,J,K2)*W(2,I,J,K2)*
439        1 COS(ANG(J))-W(1,I,J,K2)/W(1,I,J,K2)*W(3,I,J,K2)*SIN(
440        1ANG(J)))/(1./Q+SR(I)*COS(ANG(J))))*DT/2.-(W(1,I,J,K2)/
441        1 W(1,I,J,K2)*W(2,I,J,K2)*0.5+0.25*(W(2,I+1,J,K2)+W(2,I-1,J,K2)))
442        1 /SR(I)*DT/2.0
443         F(2,I,J,K2)=(-(W(2,I,J,K2)**2/W(1,I,J,K2)*0.5+0.25*(W(2,I+1,J,K2)
444        1 **2/W(1,I+1,J,K2)+W(2,I-1,J,K2)**2/W(1,I-1,J,K2)))/SR(I)
445        1+W(3,I,J,K2)**2/(W(1,I,J,K2)*SR(I))-W(2,I,J,K2)*
446        2(W(2,I,J,K2)*COS(ANG(J))-W(3,I,J,K2)*SIN(ANG(J)))/(W(1,I,J,K2)
447        3*(1./Q+SR(I)*COS(ANG(J))))+(W(4,I,J,K2)**2)*COS(ANG(J))
448        4/(W(1,I,J,K2)*(1./Q+SR(I)*COS(ANG(J))))+(C3(I,J,K2)*
449        5B2(I,J,K2)-C2(I,J,K2)*B3(I,J,K2)))*DT/2.
450         F(3,I,J,K2)=(
451        1-(2.0*W(2,I,J,K2)*W(3,I,J,K2)/W(1,I,J,K2)*0.75+0.25*(W(2,I+1,J,K2)
452        1 *W(3,I+1,J,K2)/W(1,I+1,J,K2)+W(2,I-1,J,K2)*W(3,I-1,J,K2)
453        1 /W(1,I-1,J,K2)))/
454        1SR(I)-(W(4,I,J,K2)**2)*SIN(ANG(J))/(W(1,I,J,K2)*
455        2(1./Q+SR(I)*COS(ANG(J))))-W(3,I,J,K2)*(W(2,I,J,K2)*
456        3COS(ANG(J))-W(3,I,J,K2)*SIN(ANG(J)))/(W(1,I,J,K2)*(1./Q+
457        4SR(I)*COS(ANG(J))))+(C1(I,J,K2)*B3(I,J,K2)-C3(I,J,K2)*
458        5B1(I,J,K2)))*DT/2.
459         F(4,I,J,K2)=(-2.*W(4,I,J,K2)*(W(2,I,J,K2)*COS(ANG(J))
460        1-W(3,I,J,K2)*SIN(ANG(J)))/(W(1,I,J,K2)*(1./Q+SR(I)*
461        2COS(ANG(J))))+(C2(I,J,K2)*B1(I,J,K2)-C1(I,J,K2)*B2(I,J,K2))
462        3)*DT/2.-(W(2,I,J,K2)*W(4,I,J,K2)/W(1,I,J,K2)
463        1 *0.5+0.25*(W(2,I+1,J,K2)*W(4,I+1,J,K2)/W(1,I+1,J,K2)
464        1 +W(2,I-1,J,K2)*W(4,I-1,J,K2)/W(1,I-1,J,K2)))/SR(I)*DT/2.0
465   CC
466   CC....INTERMEDIATE VALUES W(M,I,J,2)  (EQ.(10'), SECTION 2.1)
467         W(1,I,J,K+1)=0.125*(W(1,I+1,J,K)+W(1,I-1,J,K)+W(1,I,J+1,K)+
468        1W(1,I,J-1,K))*2.0*PPOWW+(1.0-PPOWW)*W(1,I,J,K)
469         W(2,I,J,K+1)=0.125*(W(2,I+1,J,K)+W(2,I-1,J,K)+W(2,I,J+1,K)+
470        1W(2,I,J-1,K))*2.0*PPOWW+(1.0-PPOWW)*W(2,I,J,K)
471         W(3,I,J,K+1)=0.125*(W(3,I+1,J,K)+W(3,I-1,J,K)+W(3,I,J+1,K)+
472        1W(3,I,J-1,K))*2.0*PPOWW+(1.0-PPOWW)*W(3,I,J,K)
473         W(4,I,J,K+1)=0.125*(W(4,I+1,J,K)+W(4,I-1,J,K)+W(4,I,J+1,K)+
474        1W(4,I,J-1,K))*2.0*PPOWW+(1.0-PPOWW)*W(4,I,J,K)
475         DO 435 L=1,4
476         IF (ABS(W(L,I,J,K+1)) .LT. SMALL) W(L,I,J,K+1)=0.
477      435 CONTINUE
478      434 CONTINUE
479   CC
480   CC....B. C. ; W
```

```
481      433 CONTINUE
482          DO 280 J=JB,JE
483          DO 281 L=1,4
484          W(L,ID,J,K+1)=W(L,IE,J,K+1)
485      281 CONTINUE
486          W(2,ID,J,K+1)=-W(2,IE,J,K+1)
487          W(2,ID,J,K  )=-W(2,IE,J,K  )
488      280 CONTINUE
489     CC
490     CC....B. C. IN THETA DIRECTION ; W
491          DO 35 I=IS,ID
492          W(1,I,JE+1,K+1)= W(1,I,JE-1,K+1)
493          W(2,I,JE+1,K+1)= W(2,I,JE-1,K+1)
494          W(3,I,JE+1,K+1)=-W(3,I,JE-1,K+1)
495          W(4,I,JE+1,K+1)=-W(4,I,JE-1,K+1)
496          W(1,I,JB-1,K+1)= W(1,I,JB+1,K+1)
497          W(2,I,JB-1,K+1)= W(2,I,JB+1,K+1)
498          W(3,I,JB-1,K+1)=-W(3,I,JB+1,K+1)
499          W(4,I,JB-1,K+1)=-W(4,I,JB+1,K+1)
500          W(1,I,JE+1,K)= W(1,I,JE-1,K)
501          W(2,I,JE+1,K)= W(2,I,JE-1,K)
502          W(3,I,JE+1,K)=-W(3,I,JE-1,K)
503          W(4,I,JE+1,K)=-W(4,I,JE-1,K)
504          W(1,I,JB-1,K)= W(1,I,JB+1,K)
505          W(2,I,JB-1,K)= W(2,I,JB+1,K)
506          W(3,I,JB-1,K)=-W(3,I,JB+1,K)
507          W(4,I,JB-1,K)=-W(4,I,JB+1,K)
508       35 CONTINUE
509     CC
510     CC     CALL ADI ; FIND NEXT TIME STEP VALUES PSI, XI AND EI(I,J,2)
511            CALL       ADI(K,M,DT,DX,DCA,CV,FK,COE,RB,UN,Q,SGO,
512           1IS,IB,IE,ID,JS,JB,JE,JD,C,IP,JP)
513       118 FORMAT (1H0,3I12)
514          DO 906 J=JS,JD
515          W(2,ID,J,1)=-W(2,IE,J,1)
516          W(2,ID,J,2)=-W(2,IE,J,2)
517          B3(ID,J,K+1)=(          XI(ID,J,K+1))/(1./Q+SR(ID)*COS(ANG(J)))
518          B1(IS,J,K+1)=B1(IS,J,K)
519          B2(IS,J,K+1)=B2(IS,J,K)
520          B3(IS,J,K+1)=B3(IS,J,K)
521          C1(IS,J,K+1)=C1(IS,J,K)
522          C2(IS,J,K+1)=C2(IS,J,K)
523          C3(IS,J,K+1)=C3(IS,J,K)
524       906  CONTINUE
525     CC
526     CC....EVALUATE ELECTRIC CONDUCTIVITY, T  (CF. SECTION 2.3)
527          DO 86 J=JB,JE
528          DO 86 I=IS,IE
529          IF (EI( I,J,K+1) .LT. 0.) WRITE (6,118) I,J  ,M
530          AJPE(I,J)=(C1(I,J,K+1)*B1(I,J,K+1)+C2(I,J,K+1)*B2(I,J,K+1)+C3(I,J,
531         1K+1)*B3(I,J,K+1))/SQRT(B1(I,J,K+1)**2+B2(I,J,K+1)**2+B3(I,J,K+1)**
532         22)
533          VELD(I,J)=SQRT(C1(I,J,K+1)**2+C2(I,J,K+1)**2+C3(I,J,K+1)**2)
534          AJOR(I,J)= ABS(VELD(I,J)**2-AJPE(I,J)**2)**0.5
535          VELD(I,J)=0.5*(ABS(AJOR(I,J))+ABS(AJPE(I,J)))
536          VELD(I,J)=VELD(I,J)*AJNOR
537         1/(W(1,I,J,K+1)*DN*DNUM*4.8E-10)
538          VELD(I,J)=ABS(VELD(I,J))/CHOF/SQRT(EI(I,J,K+1)*TNOR)
539          VELD(I,J)=CHOC*(1.0-EXP(-VELD(I,J)))/SQRT((W(1,I,J,K+1)-0.00*HU)*
540         1 DN*DNUM)
```

```
      IF(VELD(I,J).LT.1.0E-55)VELD(I,J)=1.0E-55
      VELD(I,J)=1.0/VELD(I,J)/SGO
      AJPE(I,J)=CHOC                          /SQRT((W(1,I,J,K+1)-0.00*HU)*
     1 DN*DNUM)
      IF(AJPE(I,J).LT.1.0E-55)AJPE(I,J)=1.0E-55
      AJPE(I,J)=1.0/AJPE(I,J)/SGO
      T(I,J,K+1)=(ECONC*(UN*UN*EI( I,J,K+1)/CV/11600.)**1.5)/SGO
      IF(                                RMTM.GT.80WW)VELD(I,J)=POW*VELD(I,J)
      T(I,J,K+1)=AMIN1(T(I,J,K+1),VELD(I,J))
   86 CONTINUE
CC
CC
      DO 78 J=JS,JD
      C3(ID,J,2)=C3(IE,J,2)
      T(ID,J,K+1)=T(IE,J,2)
   78 CONTINUE
      DO 99 I=IS,ID
      T(I,JE+1,K+1)=T(I,JE-1,K+1)
      T(I,JB-1,K+1)=T(I,JB+1,K+1)
      C3(I,JE+1,2)=C3(I,JE-1,2)
      C3(I,1,2)=C3(I,3,2)
   99 CONTINUE
      K2=2
      DO 66 I=2,IE
      DO 66 J=2,JE
      VINT(I,J)=(1.0-PPOWW)*T(I,J,2)+0.125*(T(I+1,J,2)+T(I-1,J,2)+
     1  T(I,J+1,2)+T(I,J-1,2))*2.0*PPOWW
      ALAM(I,J)=(1.0-PPOWW)*C3(I,J,2)+PPOWW*0.25*(C3(I+1,J,2)+
     1  C3(I-1,J,2)+C3(I,J+1,2)+C3(I,J-1,2))
   66 CONTINUE
      DO 67 I=2,IE
      DO 67 J=2,JE
      T(I,J,2)=VINT(I,J)
      C3(I,J,2)=ALAM(I,J)
   67 CONTINUE
      DO 68 I=IS,ID
      T(I,JE+1,K+1)=T(I,JE-1,K+1)
      T(I,JB-1,K+1)=T(I,JB+1,K+1)
      C3(I,JE+1,2)=C3(I,JE-1,2)
      C3(I,1,2)=C3(I,3,2)
   68 CONTINUE
      DO 69 J=1,JD
      C3(ID,J,2)=0.0
      T(ID,J,2)=0.0
   69 CONTINUE
CC
CC....EVALUATE (S+F)/2 USING W(M,I,J,2)  (S AND F IN EQ.8,SECTION2.1)
      DO 33 J=JB,JE
      DO 34 I=IB,IE
      F(1,I,J,K2)=(-(W(1,I,J,K2)/W(1,I,J,K2)*W(2,I,J,K2)*
     1 COS(ANG(J))-W(1,I,J,K2)/W(1,I,J,K2)*W(3,I,J,K2)*SIN(
     1ANG(J)))/(1./Q+SR(I)*COS(ANG(J))))*DT/2.-(W(1,I,J,K2)/
     1 W(1,I,J,K2)*W(2,I,J,K2)*0.5+0.25*(W(2,I+1,J,K2)+W(2,I-1,J,K2)))
     1 /SR(I)*DT/2.0
      F(2,I,J,K2)=(-(W(2,I,J,K2)**2/W(1,I,J,K2)*0.5+0.25*(W(2,I+1,J,K2)
     1 **2/W(1,I+1,J,K2)+W(2,I-1,J,K2)**2/W(1,I-1,J,K2)))/SR(I)
     1+W(3,I,J,K2)**2/(W(1,I,J,K2)*SR(I))-W(2,I,J,K2)*
     2(W(2,I,J,K2)*COS(ANG(J))-W(3,I,J,K2)*SIN(ANG(J)))/(W(1,I,J,K2)
     3*(1./Q+SR(I)*COS(ANG(J))))+(W(4,I,J,K2)**2)*COS(ANG(J))
     4/(W(1,I,J,K2)*(1./Q+SR(I)*COS(ANG(J))))+(C3(I,J,K2)*
```

```
      5B2(I,J,K2)-C2(I,J,K2)*B3(I,J,K2)))*DT/2.
       F(3,I,J,K2)=(
      1-(2.0*W(2,I,J,K2)*W(3,I,J,K2)/W(1,I,J,K2)*0.75+0.25*(W(2,I+1,J,K2)
      1 *W(3,I+1,J,K2)/W(1,I+1,J,K2)+W(2,I-1,J,K2)*W(3,I-1,J,K2)
      1 /W(1,I-1,J,K2)))/
      1SR(I)-(W(4,I,J,K2)**2)*SIN(ANG(J))/(W(1,I,J,K2)*
      2(1./Q+SR(I)*COS(ANG(J))))-W(3,I,J,K2)*(W(2,I,J,K2)*
      3COS(ANG(J))-W(3,I,J,K2)*SIN(ANG(J)))/(W(1,I,J,K2)*(1./Q+
      4SR(I)*COS(ANG(J))))+(C1(I,J,K2)*B3(I,J,K2)-C3(I,J,K2)*
      5B1(I,J,K2)))*DT/2.
       F(4,I,J,K2)=(-2.*W(4,I,J,K2)*(W(2,I,J,K2)*COS(ANG(J))
      1-W(3,I,J,K2)*SIN(ANG(J)))/(W(1,I,J,K2)*(1./Q+SR(I)*
      2COS(ANG(J))))+(C2(I,J,K2)*B1(I,J,K2)-C1(I,J,K2)*B2(I,J,K2))
      3)*DT/2.-(W(2,I,J,K2)*W(4,I,J,K2)/W(1,I,J,K2)
      1 *0.5+0.25*(W(2,I+1,J,K2)*W(4,I+1,J,K2)/W(1,I+1,J,K2)
      1 +W(2,I-1,J,K2)*W(4,I-1,J,K2)/W(1,I-1,J,K2)))/SR(I)*DT/2.0
   34 CONTINUE
   33 CONTINUE
CC
CC....FIND NEXT TIME STEP VALUES W(M,I,J,3) ;
CC....YIMCRO(THETA IMPLICIT), XIMCRO(R DIRECTION IMPLICIT)
      IF (MOD(M,2) .EQ. 1) GO TO 55
      GO TO 52
   55 CALL       YIMCRO(K,M,DT,DX,DCA,CV,FK,COE,RB,Q,UN,BATA,SGO,
     1IS,IB,IE,ID,JS,JB,JE,JD,C,IP,JP,TMALL,DISS)
      GO TO 253
   52 CALL       XIMCRO(K,M,DT,DX,DCA,CV,FK,COE,RB,Q,UN,BATA,SGO,
     1IS,IB,IE,ID,JS,JB,JE,JD,C,IP,JP,TMALL,DISS)
  253 CONTINUE
      TTTCUR=TTCUR
      TTCUR=TCUR
      TCUR=0.0
CC    FIND TOTAL TOROIDAL PLASMA CURRENT, TCUR(IN AMP.)
      CALL ARAIN(C3(1,1,K+1),TCUR,RB,RSMA)
      TCUR=TCUR/3.0E9*C*BTOR/(4.0*PI*RSMA)
      DO 903 J=JS,JD
      DO 903 I=1,4
      W(I,IS,J,K+2)=W(I,IS,J,K+1)
  903 CONTINUE
      DO 620 J=JS,JD
      UTH(J)=(EI(ID,J,K+1)-EI(ID-1,J,K+1))/(1.*DX)
      UTH(J)= UTH(J)*UN*UN/CV/RSMA*CNCON
  620 CONTINUE
CC    TOTAL CONDUCTION LOSS WTFIN
      CALL SURIN(UTH,WTFINC,RB,RSMA)
      WTFIN=WTFIN+WTFINC*TIMINC
      WINTOT=WIN+WTFIN
      DO 607 J=JS,JD
       UTH(J)=0.5*DN*(W(2,IE,J,K+2)**2+W(3,IE,J,K+2)**2+
     1 W(4,IE,J,K+2)**2)/W(1,IE,J,K+2)*UN*UN
      UTH(J)=UTH(J)+2.5*W(1,IE,J,K+2)*DN*2.*DNUM*1.38E-16*
     1  EI(IE,J,K+1)/CV*UN*UN
      UTH(J)=UTH(J)*W(2,IE,J,K+2)*UN/W(1,IE,J,K+2)
  607 CONTINUE
      CALL SURIN(UTH,WRINC,RB,RSMA)
      WRRR=WRRR+WRINC*TIMINC
      IF (MOD(M,MW) .EQ. 0 .AND. M.GE.MST) GO TO 89
      GO TO 91
   89 CONTINUE
      SIME=TIME*RSMA/UN
```

```
661         WRITE (6,104) M,SIME,DT,UN,COE
662       104 FORMAT(1H1,"CYCLE=",I5,2X,"TIME=",1PE14.7,2X,"DT=",E14.7,
663          1"UN=",E14.7,E16.7)
664      CC
665      CC....CHANGE TO CGS GAUSSIAN UNITS FOR PRINTING
666           DO 92 I=IS,ID
667           DO 92 J=JS,JD
668           XI (I,J,K)=XI (I,J,K+1)*BTOR *RSMA
669           PSI(I,J,K)=PSI(I,J,K+1)*BTOR*RSMA**2
670           B1 (I,J,K)=B1 (I,J,K+1)*BTOR
671           B2 (I,J,K)=B2 (I,J,K+1)*BTOR
672           B3 (I,J,K)=B3 (I,J,K+1)*BTOR
673           C1 (I,J,K)=C1 (I,J,K+1)*C*BTOR/(4.*PI*RSMA)
674           C2 (I,J,K)=C2 (I,J,K+1)*C*BTOR/(4.*PI*RSMA)
675           C3 (I,J,K)=C3 (I,J,K+1)*C*BTOR/(4.*PI*RSMA)
676        92 CONTINUE
677       106 FORMAT (1H ,2I3,8E15.7)
678           ,     WRITE (6,107)
679       107 FORMAT (1H0,1X,"I",1X,"J",2X,"DENSITY", 2X,"RAD VEL",2X,
680          1 "TEMP",5X,"THET MAG",1X,"TORO MAG",1X,"THET CUR",1X,"TORO CUR"
681          2 ,1X,"ANOM RES",1X,"CLAS RES",1X,"THET VEL",1X,"TORO VEL"
682          3 ,1X,"RAD MAG")
683           DO 93 I=IS,ID
684           DO 93 J=JS,JD
685           F(2,I,J,K+1)=W(2,I,J,K+2)/W(1,I,J,K+2)*UN
686           F(3,I,J,K+1)=W(3,I,J,K+2)/W(1,I,J,K+2)*UN
687           F(4,I,J,K+1)=W(4,I,J,K+2)/W(1,I,J,K+2)*UN
688           F(1,I,J,K+1)=EI(I,J,K+1)/CV*UN*UN
689           T  (I,J,K)=T  (I,J,K+1)
690           CN(I,J,K)=CN(I,J,K+1)*DN*CV*RSMA*UN
691           ALAM(I,J)=(F(1,I,J,K+1)/TEMINI)**1.5
692           IF(MOD(MBB,2).EQ.0)WRITE (6,108) I,J,W(1,I,J,K+2),F(2,I,J,K+1),
693          1                F(1,I,J,K+1),                          B2(I,J,K),B3(I,J,K)
694          2,C2(I,J,K),C3(I,J,K),VELD(I,J),ALAM(I,J),F(3,I,J,K+1)
695          3,F(4,I,J,K+1),B1(I,J,K)
696        93 CONTINUE
697      CC
698      CC....FOR PLOTTING
699           DO 551 I=1,10
700           IF(I.GT.6) GO TO 552
701           L=I-7
702           IF(B2(-L,JE,1).LT.0.0)BAX=L-B2(-L+1,JE,1)/(B2(-L,JE,1)-B2(-L+1,JE,
703          11))
704           IF(B2(-L,JE,1).LT.0.0)GO TO 553
705       552 CONTINUE
706           L=I-5
707           IF(B2(L,JB,1).GT.0.0)BAX=L-2-B2(L-1,JB,1)/(B2(L,JB,1)-B2(L-1,JB,1)
708          1)
709           IF(B2(L,IB,1).GT.0.0)GO TO 553
710       551 CONTINUE
711       553 BAX=BAX*DX
712           IDD=ID-2
713           DO 1200 I=1,IDD
714           J=ID-I
715           X(I)=(I-IE)
716           FVL(I,1)=W(1,J,JE,3)
717           FVL(I,2)=F(1,J,JE,2)
718           FVL(I,3)=B3(J,JE,1)
719           FVL(I,4)=-B2(J,JE,1)
720           FVL(I,5)=C3(J,JE,1)
```

```
721         FVL(I,6)=(SR(J)+BAX)*Q*B3(J,JE,1)/B2(J,JE,1)
722    1200 CONTINUE
723         IDS=ID-1
724         IDN=2*ID-3
725         DO 1300 I=IDS,IDN
726         X(I)=(I-IE)
727         J=I-ID+2
728         FVL(I,1)=W(1,J,JB,3)
729         FVL(I,2)=F(1,J,JB,2)
730         FVL(I,3)=B3(J,JB,1)
731         FVL(I,4)=B2(J,JB,1)
732         FVL(I,5)=C3(J,JB,1)
733         FVL(I,6)=(SR(J)-BAX)*Q*B3(J,JB,1)/B2(J,JB,1)
734    1300 CONTINUE
735         CALL WPLOT(X,FVL(1,1),FVL(1,2),FVL(1,3),FVL(1,4),FVL(1,5),
736        1  FVL(1,6),IDN,SIME)
737   CC
738   CC
739      100 FORMAT (1H ,2I2,1P14E9.1)
740         DO 802 I=1,ID
741         DO 802 J=1,JD
742         VINT(I,J)=AMAX1(B3(I,J,K),0.0)
743      802 CONTINUE
744   CC    TRAPED POSITIVE TOROIDAL FLUX, TRFL
745         CALL ARAIN(VINT,TRFL,RB,RSMA)
746         DO 805 I=1,ID
747         DO 805 J=1,JD
748         VINT(I,J)=AMIN1(B3(I,J,K),0.0)
749         EI(I,J,1)=-XI(I,J,1)
750         T(I,J,1)=-C2(I,J,1)
751      805 CONTINUE
752   CC    TOTAL TOROIDAL FLUX, TOTFL
753         CALL ARAIN(VINT,ANFL,RB,RSMA)
754         TOTFL=TRFL+ANFL
755         WRITE(6,306)TCUR
756         WRITE(6,807)M, PSI(ID,5,K+1),PSINC,PSIPR,TCUR,SURCUR,TRFL,TOTFL
757         IF(ITURN .EQ. 1)CALL WWPLOT(XNL,TVA1,TVA2,TVA3,NLL)
758         ITURN=0
759      306 FORMAT(1H ,"** TOTAL TOROID CURR(IN AMP.)=",1PE12.3)
760         WINTOT=WINTOT+1.5*DN*DNUM*2.0*VOLU*1.38E-16*TEMINI
761         DO 602 I=IS,ID
762         DO 602 J=JS,JD
763         VINT(I,J)=(B1(I,J,K)**2+B2(I,J,K)**2+B3(I,J,K)**2)/8./PI
764   CCCC  WRITE(6,108)I,J,F(3,I,J,2),F(4,I,J,2),B1(I,J,K),C1(I,J,K)
765    602  CONTINUE
766   CC    TOTAL MAGNETIC ENERGY, WBE
767         CALL VOLIN(VINT,WBE,RB,RSMA)
768         DO 603 I=IS,ID
769         DO 603 J=JS,JD
770         VINT(I,J)=1.5*W(1,I,J,K+2)*DN*2.*DNUM*1.38E-16*F(1,I,J,K+1)
771    603  CONTINUE
772   CC    TOTAL THERMAL ENERGY, WIE
773         CALL VOLIN(VINT,WIE,RB,RSMA)
774         DO 604 I=IS,ID
775         DO 604 J=JS,JD
776         VINT(I,J)=0.5*W(1,I,J,K+2)*DN*(F(2,I,J,K+1)**2+F(3,I,J,K+1)**2+
777        1 F(4,I,J,K+1)**2)
778    604  CONTINUE
779   CC    TOTAL KINETIC ENERGY, WME
780         CALL VOLIN(VINT,WME,RB,RSMA)
```

```
781          WTOTR=WBE+WIE
782          WTOT=WTOTR+WME
783          DO 632 I=IS,ID
784          DO 632 J=JS,JD
785          VINT(I,J)=W(1,I,J,K+2)
786      632 CONTINUE
787      CC  TOTAL MASS, TOMA
788          CALL VOLIN(VINT,TOMA,RB,RSMA)
789      CC  POLOIDAL BETA(PLBT), AVERAGE TEMP.(AVT), TOTAL ENERGY INPUT(WIINT)
790          TOMA=TOMA/VOLU
791          PLBT=WIE*2.0/TCUR/TCUR/1.5
792          TNM=VOLU*DN*DNUM*2.0
793          AVT=WIE/TNM/1.4E-16/1.5/11600.0
794          WIINT=WTOT-WTFIN
795          WRITE(6,606)M,AVT,PLBT,WIINT
796          NLL=NLL+1
797          IL=ID*3/5
798          JL=JD/4+1
799          TVA1(NLL)=AVT
800          TVA2(NLL)=PLBT
801          TVA3(NLL)=WIINT
802          XNL(NLL)=NLL
803          JM=JD/2.0+0.5
804          TVA4(NLL)=Q*B3(ID,JM,1)/B2(IE,JM,1)
805          TVA5(NLL)=B3(1,2,1)
806          TVA6(NLL)=W(1,1,2,3)
807          WRITE(6,606)M,SIME,WZIN,WTIN,WBE,WIE,WME,WRRR ,WTFIN,WIN,WINTOT
808         1 ,WTOT,TOMA
809      606 FORMAT(1H0,I5,1P12E10.2)
810       91 CONTINUE
811          IF(M .GT. MBK) GO TO ABKP
812          GO TO PASS
813      ABKP CONTINUE
814          QQQQ=PI
815      PASS CONTINUE
816          IF (M .GE. MS) GO TO 94
817      CC
818      CC  INITIALIZATION FOR NEXT CYCLE
819          DO 96 I=IS,ID
820          DO 96 J=JS,JD
821          T  (I,J,K)=T  (I,J,K+1)
822          EI(I,J,K) = EI(I,J,K+1)
823          PSI(I,J,K)=PSI(I,J,K+1)
824          B3(I,J,K)= B3(I,J,K+1)
825          B1 (I,J,K)=B1 (I,J,K+1)
826          B2 (I,J,K)=B2 (I,J,K+1)
827          XI (I,J,K)=XI (I,J,K+1)
828          C1 (I,J,K)=C1 (I,J,K+1)
829          C2 (I,J,K)=C2 (I,J,K+1)
830          C3 (I,J,K)=C3 (I,J,K+1)
831          CN (I,J,K)=CN (I,J,K+1)
832          DO 97 L=1,4
833          W(L,I,J,K)= W(L,I,J,K+2)
834          IF (ABS(W(L,I,J,K)) .LT. SMALL) W(L,I,J,K)=0.
835       97 CONTINUE
836      CC
837      CC....LOW DENSITY REGION TREATMENT (CF. SECTION 3.3)
838          IF(I .EQ. 1 .OR. I.EQ.ID)GO TO 81
839          IF(W(1,I,J,K).LT.1.2*HU.AND.W(1,I-1,J,K).GT.1.8*HU.AND.
840         1 W(2,I-1,J,K).LT.0.0)W(1,I-1,J,K)=W(1,I-1,J,K)+BATA*(W(2,I-1,J,K)
```

```
     1 +W(2,I,J,K))
      IF(W(1,I,J,K).LT.1.2*HU.AND.W(1,I-1,J,K).GT.1.8*HU.AND.
     1 W(2,I-1,J,K).GT.0.0)W(1,I-1,J,K)=W(1,I-1,J,K)+BATA* W(2,I   ,J,K)
      IF(W(1,I-1,J,K).LT.1.2*HU.AND.W(1,I,J,K).GT.1.8*HU.AND. W(2,I,J,K)
     1 .GT.0.0)W(1,I,J,K)=W(1,I,J,K)-BATA*(W(2,I,J,K)+W(2,I-1,J,K))
      IF(W(1,I,J,K).LT.1.2*HU.AND.W(1,I-1,J,K).GT.1.8*HU.AND. W(2,I-1,J,
     1 K).LT.0.0)W(2,I-1,J,K)=W(2,I-1,J,K)+BATA*(W(2,I-1,J,K)**2/
     1 W(1,I-1,J,K)+W(2,I,J,K)**2/W(1,I,J,K))
      IF(W(1,I,J,K).LT.1.2*HU.AND.W(1,I-1,J,K).GT.1.8*HU.AND. W(2,I-1,J,
     1 K).GT.0.0)W(2,I-1,J,K)=W(2,I-1,J,K)+BATA* W(2,I   ,J,K)**2/
     1 W(1,I   ,J,K)
      IF(W(1,I-1,J,K).LT.1.2*HU.AND.W(1,I,J,K).GT.1.8*HU.AND. W(2,I,J,K)
     1 .GT.0.0)W(2,I,J,K)=W(2,I,J,K)-BATA*(W(2,I,J,K)**2/W(1,I,J,K)
     1 +W(2,I-1,J,K)**2/W(1,I-1,J,K))
  81  IF(W(1,I,J,K).LT.HU) W(1,I,J,K)=HU
  96 CONTINUE
     GO TO 6
  94 CONTINUE
     CALL WWPLOT(XNL,TVA1,TVA2,TVA3,NLL)
     CALL WWPLOT(XNL,TVA4,TVA5,TVA6,NLL)
     WRITE (6,109) DT
 109 FORMAT(1H ,"END OF THE SCREW PINCH",4X,"DT=",E14.7)
     STOP
     END
     SUBROUTINE WPLOT(X,A,B,C,D,E,F,IDN,SIME)
     DIMENSION X(40),A(40),B(40),C(40),D(40),E(40),F(40)
     COMMON /HEADERS/ LABEL(8),TIME(2),JOBNM,DATE,HOUR
     REWIND 63
     WRITE(63,2)SIME
   2 FORMAT(2HT=,1PE9.2,4H SEC)
     READ(63,3)TIME
   3 FORMAT(2A10)
     CALL LPLOT(-2,4,IDN,X,A,1,1,1H ,1HR,4HDENS)
     CALL LPLOT(-3,4,IDN,X,B,1,1,1H ,1HR,4HTEMP)
     CALL LPLOT(-2,5,IDN,X,C,1,1,1H ,1HR,2HBZ)
     CALL LPLOT(-2,6,IDN,X,D,1,1,1H ,1HR,3HDTH)
     CALL LPLOT(-3,5,IDN,X,E,1,1,1H ,1HR,2HJZ)
     CALL LPLOT(-3,6,IDN,X,F,1,1,1H ,1HR,1HQ)
     RETURN
     END
     SUBROUTINE WWPLOT(XNL,TVA1,TVA2,TVA3,NLL)
     DIMENSION XNL(100),TVA1(100),TVA2(100),TVA3(100)
     CALL DDERS(-1)
     CALL FRAME
     CALL MAPPARAM(2,0,15,0,1)
     AMY=AMAXAF(TVA1,1,NLL,1)
     AMIY=AMINAF(TVA1,1,NLL,1)
     CALL MAPS(XNL(1),XNL(NLL),AMIY,AMY,0.0,1.0,0.76,1.0)
     CALL SETPCH(1,0,1,0,20)
     CALL TRACEC(1H ,XNL,TVA1,NLL)
     AMY=AMAXAF(TVA2,1,NLL,1)
     AMIY=AMINAF(TVA2,1,NLL,1)
     CALL MAPS(XNL(1),XNL(NLL),AMIY,AMY,0.0,1.0,0.44,0.68)
     CALL SETPCH(1,0,1,0,20)
     CALL TRACEC(1H ,XNL,TVA2,NLL)
     AMY=AMAXAF(TVA3,1,NLL,1)
     AMIY=AMINAF(TVA3,1,NLL,1)
     CALL MAPS(XNL(1),XNL(NLL),AMIY,AMY,0.0,1.0,0.12,0.36)
     CALL SETPCH(1,0,1,0,20)
     CALL TRACEC(1H ,XNL,TVA3,NLL)
```

```
      RETURN
      END
      SUBROUTINE YIMCRO(K,M,DT,DX,DCA,CV,FK,COE,RB,Q,UN,BATA,SGO,
     1IS,IB,IE,ID,JS,JB,JE,JD,C,IP,JP,TMALL,DISS)
CC
CC---- SOLVE NEW TIME STEP VALUES W(M,I,J,3) IN THETA DIREC. IMPLICIT
CC
      DIMENSION PSI(20,16,2),B1(20,16,2),B2(20,16,2),XI(20,16,2),
     1C1(20,16,2),C2(20,16,2),C3(20,16,2),T(20,16,2),
     2W(4,20,16,3),F(4,20,16,3),EI(20,16,2),B3(20,16,2),SR(20),
     4GA(20,16),GB(20,16),GC(20,16),GD(20,16),CN(20,16,2),
     5AA(90,12),BB(4,4),ANG(16),BATB(20)
      COMMON PSI,B1,B2,B3,XI,C1,C2,C3,T,W,F,SR,ANG,BATB
     1,GA,GB,GC,GD,CN,EI,AA,BB,AICON
      K1=1
      K2=3
      K3=1
      K=1
CC
CC....FIND F IN THE MATRIX EQ. PW = F
      DO 38 J=JB,JE
      DO 39 I=IB,IE
      F(1,I,J,K2)=W(1,I,J,K1)
     1-BATA      *(        W(2,I+1,J,K3)-
     2       W(2,I-1,J,K3))+F(1,I,J,K)+F(1,I,J,K+1)
     6+DISS*0.5*DT/DX*(ABS(W(2,I+1,J,K)/W(1,I+1,J,K)-W(2,I,J,K)
     7/W(1,I,J,K))*(W(1,I+1,J,K)-W(1,I,J,K))-ABS(W(2,I,J,K)/W(1,I,J,K)
     8-W(2,I-1,J,K)/W(1,I-1,J,K))*(W(1,I,J,K)-W(1,I-1,J,K)))
     6+DISS*BATB(I)*(ABS(W(3,I,J+1,K)/W(1,I,J+1,K)-W(3,I,J,K)
     7/W(1,I,J,K))*(W(1,I,J+1,K)-W(1,I,J,K))-ABS(W(3,I,J,K)/W(1,I,J,K)
     8-W(3,I,J-1,K)/W(1,I,J-1,K))*(W(1,I,J,K)-W(1,I,J-1,K)))
      F(2,I,J,K2)=W(2,I,J,K1)
     1-BATA      *(        (W(2,I+1,J,K3)**2
     2/W(1,I+1,J,K3)+(FK-1.)*W(1,I+1,J,K3)*EI(I+1,J,K3))-
     3(W(2,I-1,J,K3)**2/W(1,I-1,J,K3) +(FK-1.)*W(1,I-1,J,K3)
     4*EI(I-1,J,K3)))+F(2,I,J,K)+F(2,I,J,K+1)
     6+DISS*0.5*DT/DX*(ABS(W(2,I+1,J,K)/W(1,I+1,J,K)-W(2,I,J,K)
     7/W(1,I,J,K))*(W(2,I+1,J,K)-W(2,I,J,K))-ABS(W(2,I,J,K)/W(1,I,J,K)
     8-W(2,I-1,J,K)/W(1,I-1,J,K))*(W(2,I,J,K)-W(2,I-1,J,K)))
     6+DISS*BATB(I)*(ABS(W(3,I,J+1,K)/W(1,I,J+1,K)-W(3,I,J,K)
     7/W(1,I,J,K))*(W(2,I,J+1,K)-W(2,I,J,K))-ABS(W(3,I,J,K)/W(1,I,J,K)
     8-W(3,I,J-1,K)/W(1,I,J-1,K))*(W(2,I,J,K)-W(2,I,J-1,K)))
      F(3,I,J,K2)=W(3,I,J,K1)
     1-BATA      *(        W(2,I+1,J,K3)*
     2W(3,I+1,J,K3)/W(1,I+1,J,K3)-        W(2,I-1,J,K3)*W(3,I-1,J,K3)
     3/W(1,I-1,J,K3))+F(3,I,J,K)+F(3,I,J,K+1)
     6+DISS*0.5*DT/DX*(ABS(W(2,I+1,J,K)/W(1,I+1,J,K)-W(2,I,J,K)
     7/W(1,I,J,K))*(W(3,I+1,J,K)-W(3,I,J,K))-ABS(W(2,I,J,K)/W(1,I,J,K)
     8-W(2,I-1,J,K)/W(1,I-1,J,K))*(W(3,I,J,K)-W(3,I-1,J,K)))
     6+DISS*BATB(I)*(ABS(W(3,I,J+1,K)/W(1,I,J+1,K)-W(3,I,J,K)
     7/W(1,I,J,K))*(W(3,I,J+1,K)-W(3,I,J,K))-ABS(W(3,I,J,K)/W(1,I,J,K)
     8-W(3,I,J-1,K)/W(1,I,J-1,K))*(W(3,I,J,K)-W(3,I,J-1,K)))
      F(4,I,J,K2)=W(4,I,J,K1)
     1-BATA      *(        W(2,I+1,J,K3)
     2*W(4,I+1,J,K3)/W(1,I+1,J,K3)-        W(2,I-1,J,K3)*W(4,I-1,J,K3)
     1/W(1,I-1,J,K3))+F(4,I,J,K)+F(4,I,J,K+1)
     6+DISS*0.5*DT/DX*(ABS(W(2,I+1,J,K)/W(1,I+1,J,K)-W(2,I,J,K)
     7/W(1,I,J,K))*(W(4,I+1,J,K)-W(4,I,J,K))-ABS(W(2,I,J,K)/W(1,I,J,K)
     8-W(2,I-1,J,K)/W(1,I-1,J,K))*(W(4,I,J,K)-W(4,I-1,J,K)))
     6+DISS*BATB(I)*(ABS(W(3,I,J+1,K)/W(1,I,J+1,K)-W(3,I,J,K)
```

```
      7/W(1,I,J,K))*(W(4,I,J+1,K)-W(4,I,J,K))-ABS(W(3,I,J,K)/W(1,I,J,K)
      8-W(3,I,J-1,K)/W(1,I,J-1,K))*(W(4,I,J,K)-W(4,I,J-1,K)))
   39 CONTINUE
      F(2,IE,J,K2)=F(2,IE,J,K2)+2.0*BATA*W(2,ID,J,K)**2/W(1,ID,J,K)
   38 CONTINUE
CC
CC....FIND ELEMENTS AA OF MATRIX P IN THE MATRIX EQ. PW=F.
      DO 113 I=IB,IE
      DO 114 J=JS,JP
      IF (J .EQ. JS) GO TO 115
      AA(4*J-3,1)=0.
      AA(4*J-3,2)=0.
      AA(4*J-3,3)=-BATB(I)
      AA(4*J-3,4)=0.
      AA(4*J-2,1)= 0.0
      AA(4*J-2,2)=-BATB(I)*(W(3,I,J,K+1)/W(1,I,J,K+1))
      AA(4*J-2,3)=0.0
      AA(4*J-2,4)=0.
      AA(4*J-1,1)=-BATB(I)* (FK-1.)*EI(I,J,K+1)
      AA(4*J-1,2)=0.
      AA(4*J-1,3)=-BATB(I)*(   W(3,I,J,K+1)/W(1,I,J,K+1))
      AA(4*J-1,4)=0.
      AA(4*J  ,1)=0.0
      AA(4*J  ,2)=0.
      AA(4*J  ,3)=0.0
      AA(4*J  ,4)=-BATB(I)*(W(3,I,J,K+1)/W(1,I,J,K+1))
  115 CONTINUE
      IF (J .EQ. JP) GO TO 116
      AA(4*J-3,9)=0.
      AA(4*J-3,10)=0.
      AA(4*J-3,11)=+BATB(I)
      AA(4*J-3,12)=0.
      AA(4*J-2,9)= 0.0
      AA(4*J-2,10)=+BATB(I)*(W(3,I,J,K+1)/W(1,I,J,K+1))
      AA(4*J-2,11)=0.0
      AA(4*J-2,12)=0.
      AA(4*J-1,9)=+BATB(I)* (FK-1.)*EI(I,J,K+1)
      AA(4*J-1,10)=0.
      AA(4*J-1,11)=+BATB(I)*(   W(3,I,J,K+1)/W(1,I,J,K+1))
      AA(4*J-1,12)=0.
      AA(4*J  ,9)=0.0
      AA(4*J  ,10)=0.
      AA(4*J  ,11)=0.0
      AA(4*J  ,12)=+BATB(I)*(W(3,I,J,K+1)/W(1,I,J,K+1))
  116 CONTINUE
      AA(4*J-3,5)=1.
      AA(4*J-3,6)=0.
      AA(4*J-3,7)=0.
      AA(4*J-3,8)=0.
      AA(4*J-2,5)=0.
      AA(4*J-2,6)=1.
      AA(4*J-2,7)=0.
      AA(4*J-2,8)=0.
      AA(4*J-1,5)=0.
      AA(4*J-1,6)=0.
      AA(4*J-1,7)=1.
      AA(4*J-1,8)=0.
      AA(4*J  ,5)=0.
      AA(4*J  ,6)=0.
      AA(4*J  ,7)=0.
```

```
1021          AA(4*J   ,8)=1.
1022        114 CONTINUE
1023          DO 207 L=1,2
1024          DO 208 LL=9,12
1025          AA(L   ,LL)= 2.*AA(L   ,LL)
1026          AA(L+2,LL)=0.
1027        208 CONTINUE
1028        207 CONTINUE
1029          JP1=4*(JP-1)+1
1030          JP2=JP1+1
1031          DO 307 L=JP1,JP2
1032          DO 308 LL=1,4
1033          AA(L   ,LL)= 2.*AA(L   ,LL)
1034          AA(L+2,LL)=0.
1035        308 CONTINUE
1036        307 CONTINUE
1037      CC
1038      CC....CROUT REDUCTION
1039          JPP=4*JP
1040          DO 117 J=5,JPP,4
1041          DO 188 L=1,4
1042          DO 189 LL=1,4
1043          BB(L,LL)=0.
1044          DO 121 LLL=1,4
1045          IF (ABS(AA(J+L-1,LLL)) .LT. TMALL) AA(J+L-1,LLL)=0.
1046          IF (ABS(AA(J+LLL-5,8+LL)) .LT. TMALL) AA(J+LLL-5,8+LL)=0.
1047        121 BB(L,LL)=BB(L,LL) + AA(J+L-1,LLL)*AA(J+LLL-5,8+LL)
1048        189 CONTINUE
1049        188 CONTINUE
1050          DO 122 L=1,4
1051        122 AA(J-1+L,5)=AA(J-1+L,5)-BB(L,1)
1052          DO 123 L=1,3
1053        123 AA(J,5+L)=(AA(J,5+L)-BB(1,L+1))/AA(J,5)
1054          IF (J .EQ. (JPP-3)) GO TO 924
1055          DO 124 L=1,4
1056        124 AA(J,8+L)=AA(J,8+L)/AA(J,5)
1057        924 CONTINUE
1058          DO 125 L=1,3
1059        125 AA(J+L,6)=AA(J+L,6)-BB(L+1,2)-AA(J+L,5)*AA(J,6)
1060          DO 126 L=1,2
1061        126 AA(J+1,6+L)=(AA(J+1,6+L)-BB(2,2+L)-AA(J+1,5)*AA(J,6+L))/AA(J+1,6)
1062          IF (J .EQ. (JPP-3)) GO TO 127
1063          DO 128 L=1,4
1064          AA(J+L+3,2)=AA(J+L+3,2)-AA(J+L+3,1)*AA(J,6)
1065          AA(J+1,8+L)=(AA(J+1,8+L)-AA(J+1,5)*AA(J,8+L))/AA(J+1,6)
1066        128 CONTINUE
1067        127 CONTINUE
1068          DO 129 L=1,2
1069        129 AA(J+L+1,7)=AA(J+L+1,7)-BB(2+L,3)-AA(J+L+1,5)*AA(J,7)-
1070           1AA(J+L+1,6)*AA(J+1,7)
1071          AA(J+2,8)=(AA(J+2,8)-BB(3,4)-AA(J+2,5)*AA(J,8)-AA(J+2,6)*AA(J+1,8)
1072           2)/AA(J+2,7)
1073          IF (J .EQ. (JPP-3)) GO TO 130
1074          DO 131 L=1,4
1075          DO 132 LL=1,2
1076          AA(J+L+3,3)=AA(J+L+3,3)-AA(J+L+3,LL)*AA(J+LL-1,7)
1077          AA(J+2,8+L)=AA(J+2,8+L)-AA(J+2,4+LL)*AA(J+LL-1,8+L)
1078        132 CONTINUE
1079          AA(J+2,8+L)=AA(J+2,8+L)/AA(J+2,7)
1080        131 CONTINUE
```

```
1081      130 CONTINUE
1082          AA(J+3,8)=AA(J+3,8)-BB(4,4)-AA(J+3,5)*AA(J,8)-AA(J+3,6)*AA(J+1,8)
1083         1-AA(J+3,7)*AA(J+2,8)
1084          IF (J .EQ. (JPP-3)) GO TO 133
1085          DO 134 L=1,4
1086          DO 135 LL=1,3
1087          AA(J+L+3,4)= AA(J+L+3,4)-AA(J+L+3,LL)*AA(J+LL-1,8)
1088          AA(J+3,8+L)= AA(J+3,8+L)-AA(J+3,4+LL)*AA(J+LL-1,8+L)
1089      135 CONTINUE
1090          AA(J+3,8+L)= AA(J+3,8+L)/AA(J+3,8)
1091      134 CONTINUE
1092      133 CONTINUE
1093          DO 136 L=1,4
1094          DO 137 LL=1,4
1095      137 F(L,I,(J+7)/4,K+2)=F(L,I,(J+7)/4,K+2)-AA(J+L-1,LL)*F(LL,I,(J+7)/4
1096         1-1,K+2)
1097          LE=L-1
1098          IF (L .EQ. 1) GO TO 148
1099          DO 147 LL=1,LE
1100          F(L,I,(J+7)/4,K+2)=F(L,I,(J+7)/4,K+2)-AA(J+L-1,4+LL)*F(LL,I,(J+7)
1101         1/4,K+2)
1102      147 CONTINUE
1103      148 CONTINUE
1104          F(L,I,(J+7)/4,K+2)=F(L,I,(J+7)/4,K+2)/AA(J+L-1,5+L-1)
1105      136 CONTINUE
1106      117 CONTINUE
1107          W(4,I,JE,K+2)=F(4,I,JE,K+2)
1108          W(3,I,JE,K+2)=F(3,I,JE,K+2)-AA(JPP-1,8)*W(4,I,JE,K+2)
1109          W(2,I,JE,K+2)=F(2,I,JE,K+2)-AA(JPP-2,8)*W(4,I,JE,K+2)
1110         1-AA(JPP-2,7)*W(3,I,JE,K+2)
1111          W(1,I,JE,K+2)=F(1,I,JE,K+2)-AA(JPP-3,8)*W(4,I,JE,K+2)
1112         1-AA(JPP-3,7)*W(3,I,JE,K+2)-AA(JPP-3,6)*W(2,I,JE,K+2)
1113          DO 138 J=5,JPP,4
1114          JJ=JPP+5-J-4
1115          DO 139 L=1,4
1116          BB(1,L)=0.
1117          DO 941 LL=1,4
1118      941 BB(1,L)=BB(1,L)+AA(JJ+1-L,8+LL)*W(LL,I,(JJ+4)/4+1,K+2)
1119      139 CONTINUE
1120          W(4,I,(JJ+4)/4,K+2)=F(4,I,(JJ+4)/4,K+2)-BB(1,1)
1121          W(3,I,(JJ+4)/4,K+2)=F(3,I,(JJ+4)/4,K+2)-BB(1,2)
1122         1-AA(JJ-1,8)*W(4,I,(JJ+4)/4,K+2)
1123          W(2,I,(JJ+4)/4,K+2)=F(2,I,(JJ+4)/4,K+2)-BB(1,3)
1124         1-AA(JJ-2,8)*W(4,I,(JJ+4)/4,K+2)-AA(JJ-2,7)*W(3,I,(JJ+4)/4,K+2)
1125          W(1,I,(JJ+4)/4,K+2)=F(1,I,(JJ+4)/4,K+2)-BB(1,4)
1126         1-AA(JJ-3,8)*W(4,I,(JJ+4)/4,K+2)-AA(JJ-3,7)*W(3,I,(JJ+4)/4,K+2)
1127        2-AA(JJ-3,6)*W(2,I,(JJ+4)/4,K+2)
1128      138 CONTINUE
1129      113 CONTINUE
1130          RETURN
1131          END
1132          SUBROUTINE XIMCRO(K,M,DT,DX,DCA,CV,FK,COE,RB,Q,UN,BATA,SGO,
1133         1IS,IB,IE,ID,JS,JB,JE,JD,C,IP,JP,TMALL,DISS)
1134    CC
1135    CC---- SOLVE NEW TIME STEP VALUES W(M,I,J,3) IN R DIRECTION IMPLICIT
1136    CC
1137          DIMENSION PSI(20,16,2),B1(20,16,2),B2(20,16,2),XI(20,16,2),
1138         1C1(20,16,2),C2(20,16,2),C3(20,16,2),T(20,16,2),
1139         2W(4,20,16,3),F(4,20,16,3),EI(20,16,2),B3(20,16,2),SR(20),
1140         4GA(20,16),GB(20,16),GC(20,16),GD(20,16),CN(20,16,2),
```

```
      5AA(90,12),BB(4,4),ANG(16),BATB(20)
       COMMON PSI,B1,B2,B3,XI,C1,C2,C3,T,W,F,SR,ANG,BATB
      1,GA,GB,GC,GD,CN,EI,AA,BB,AJCON
       K=1
       K1=1
       K2=3
       K3=1
CC
CC....FIND F IN THE MATRIX EQ. PW=F
       DO 41 J=JB,JE
       DO 42 I=IB,IE
       F(1,I,J,K2)=W(1,I,J,K1)
      2-BATD(I)*(W(3,I,J+1,K3)-W(3,I,J-1,K3))
      3+(F(1,I,J,K)+F(1,I,J,K+1))
      6+DISS*0.5*DT/DX*(ABS(W(2,I+1,J,K)/W(1,I+1,J,K)-W(2,I,J,K)
      7/W(1,I,J,K))*(W(1,I+1,J,K)-W(1,I,J,K))-ABS(W(2,I,J,K)/W(1,I,J,K)
      8-W(2,I-1,J,K)/W(1,I-1,J,K))*(W(1,I,J,K)-W(1,I-1,J,K)))
      6+DISS*BATB(I)*(ABS(W(3,I,J+1,K)/W(1,I,J+1,K)-W(3,I,J,K)
      7/W(1,I,J,K))*(W(1,I,J+1,K)-W(1,I,J,K))-ABS(W(3,I,J,K)/W(1,I,J,K)
      8-W(3,I,J-1,K)/W(1,I,J-1,K))*(W(1,I,J,K)-W(1,I,J-1,K)))
       F(2,I,J,K2)=W(2,I,J,K1)
      4-BATB(I)*(W(2,I,J+1,K3)*W(3,I,J+1,K3)
      5/W(1,I,J+1,K3)-W(2,I,J-1,K3)*W(3,I,J-1,K3)/W(1,I,J-1,K3))
      6+(F(2,I,J,K)+F(2,I,J,K+1))
      6+DISS*0.5*DT/DX*(ABS(W(2,I+1,J,K)/W(1,I+1,J,K)-W(2,I,J,K)
      7/W(1,I,J,K))*(W(2,I+1,J,K)-W(2,I,J,K))-ABS(W(2,I,J,K)/W(1,I,J,K)
      8-W(2,I-1,J,K)/W(1,I-1,J,K))*(W(2,I,J,K)-W(2,I-1,J,K)))
      6+DISS*BATB(I)*(ABS(W(3,I,J+1,K)/W(1,I,J+1,K)-W(3,I,J,K)
      7/W(1,I,J,K))*(W(2,I,J+1,K)-W(2,I,J,K))-ABS(W(3,I,J,K)/W(1,I,J,K)
      8-W(3,I,J-1,K)/W(1,I,J-1,K))*(W(2,I,J,K)-W(2,I,J-1,K)))
       F(3,I,J,K2)=W(3,I,J,K1)
      3-BATB(I)*((W(3,I,J+1,K3)**2/W(1,I,J+1,K3)+
      4(FK-1.)*W(1,I,J+1,K3)*EI(I,J+1,K ))-(W(3,I,J-1,K3)**K2/
      5W(1,I,J-1,K3)+(FK-1.)*W(1,I,J-1,K3)*EI(I,J-1,K )))
      6+(F(3,I,J,K)+F(3,I,J,K+1))
      6+DISS*0.5*DT/DX*(ABS(W(2,I+1,J,K)/W(1,I+1,J,K)-W(2,I,J,K)
      7/W(1,I,J,K))*(W(3,I+1,J,K)-W(3,I,J,K))-ABS(W(2,I,J,K)/W(1,I,J,K)
      8-W(2,I-1,J,K)/W(1,I-1,J,K))*(W(3,I,J,K)-W(3,I-1,J,K)))
      6+DISS*BATB(I)*(ABS(W(3,I,J+1,K)/W(1,I,J+1,K)-W(3,I,J,K)
      7/W(1,I,J,K))*(W(3,I,J+1,K)-W(3,I,J,K))-ABS(W(3,I,J,K)/W(1,I,J,K)
      8-W(3,I,J-1,K)/W(1,I,J-1,K))*(W(3,I,J,K)-W(3,I,J-1,K)))
       F(4,I,J,K2)=W(4,I,J,K1)
      3-BATB(I)*(W(3,I,J+1,K3)*W(4,I,J+1,K3)
      4/W(1,I,J+1,K3)-W(3,I,J-1,K3)*W(4,I,J-1,K3)/W(1,I,J-1,K3))
      5+(F(4,I,J,K)+F(4,I,J,K+1))
      6+DISS*0.5*DT/DX*(ABS(W(2,I+1,J,K)/W(1,I+1,J,K)-W(2,I,J,K)
      7/W(1,I,J,K))*(W(4,I+1,J,K)-W(4,I,J,K))-ABS(W(2,I,J,K)/W(1,I,J,K)
      8-W(2,I-1,J,K)/W(1,I-1,J,K))*(W(4,I,J,K)-W(4,I-1,J,K)))
      6+DISS*BATB(I)*(ABS(W(3,I,J+1,K)/W(1,I,J+1,K)-W(3,I,J,K)
      7/W(1,I,J,K))*(W(4,I,J+1,K)-W(4,I,J,K))-ABS(W(3,I,J,K)/W(1,I,J,K)
      8-W(3,I,J-1,K)/W(1,I,J-1,K))*(W(4,I,J,K)-W(4,I,J-1,K)))
   42 CONTINUE
   41 CONTINUE
      DO 153 J=JB,JE
      F(2,IE,J,K+2)=F(2,IE,J,K+2)-(FK-1.)*W(1,ID,J,K+1)*EI(ID,J,K+1)
     1*BATA+BATA*W(2,ID,J,2)**K2/W(1,ID,J,2)
      F(1,IE,J,3)=F(1,IE,J,3)-BATA*W(2,ID,J,2)
      F(3,IE,J,3)=F(3,IE,J,3)-BATA*W(2,ID,J,2)*W(3,ID,J,2)/W(1,ID,J,2)
      F(4,IE,J,3)=F(4,IE,J,3)-BATA*W(2,ID,J,2)*W(4,ID,J,2)/W(1,ID,J,2)
      F(1,IB,J,K+2)=F(1,IB,J,K+2)+BATA*W(2,IS,J,K+1)
```

```
1201          F(2,IB,J,K+2)=F(2,IB,J,K+2)+BATA*W(2,IS,J,K+1)**2/W(1,IS,J,K+1)
1202         1+BATA*(FK-1.0)*W(1,IS,J,K+1)*EI(IS,J,K+1)
1203          F(3,IB,J,K+2)=F(3,IB,J,K+2)+BATA*W(2,IS,J,K+1)*W(3,IS,J,K+1)
1204         1  /W(1,IS,J,K+1)
1205          F(4,IB,J,K+2)=F(4,IB,J,K+2)+BATA*W(2,IS,J,K+1)*W(4,IS,J,K+1)
1206         1  /W(1,IS,J,K+1)
1207    CC
1208    CC....FIND ELEMENTS AA OF MATRIX P IN THE MATRIX EQ. PW=F
1209          DO 154 I=IS,IP
1210          IF (I .EQ. IS) GO TO 155
1211          AA(4*I-3,1)=0.
1212          AA(4*I-3,2)=-BATA
1213          AA(4*I-3,3)=0.
1214          AA(4*I-3,4)=0.
1215          AA(4*I-2,1)=-BATA                 * (FK-1.)*EI(I,J,K+1)
1216          AA(4*I-2,2)=-BATA                 *(   W(2,I,J,K+1)/
1217         1W(1,I,J,K+1))
1218          AA(4*I-2,3)=0.
1219          AA(4*I-2,4)=0.
1220          AA(4*I-1,1)=0.0
1221          AA(4*I-1,2 )=0.0
1222          AA(4*I-1,3 )=-BATA                 *(W(2,I,J,K+1)/W(1,I,J,K+1))
1223          AA(4*I-1,4 )=0.
1224          AA(4*I   ,1)=0.0
1225          AA(4*I   ,2)=0.0
1226          AA(4*I   ,3)= 0.
1227          AA(4*I   ,4)=-BATA                *(W(2,I,J,K+1)/W(1,I,J,K+1))
1228      155 CONTINUE
1229          IF (I .EQ. IP) GO TO 156
1230          AA(4*I-3,9)=0.
1231          AA(4*I-3,10)=+BATA
1232          AA(4*I-3,11)=0.
1233          AA(4*I-3,12)=0.
1234          AA(4*I-2,9)=+BATA                 * (FK-1.)*EI(I,J,K+1)
1235          AA(4*I-2,10)=+BATA                 *(   W(2,I,J,K+1)/
1236         1W(1,I,J,K+1))
1237          AA(4*I-2,11)=0.
1238          AA(4*I-2,12)=0.
1239          AA(4*I-1,9)=0.0
1240          AA(4*I-1,10)=0.0
1241          AA(4*I-1,11)=+BATA                 *(W(2,I,J,K+1)/W(1,I,J,K+1))
1242          AA(4*I-1,12)=0.
1243          AA(4*I   ,9)=0.0
1244          AA(4*I   ,10)=0.0
1245          AA(4*I   ,11)= 0.
1246          AA(4*I   ,12)=+BATA                *(W(2,I,J,K+1)/W(1,I,J,K+1))
1247      156 CONTINUE
1248          AA(4*I-3,5)=1.
1249          AA(4*I-3,6)=0.
1250          AA(4*I-3,7)=0.
1251          AA(4*I-3,8)=0.
1252          AA(4*I-2,5)=0.
1253          AA(4*I-2,6)=1.
1254          AA(4*I-2,7)=0.
1255          AA(4*I-2,8)=0.
1256          AA(4*I-1,5)=0.
1257          AA(4*I-1,6)=0.
1258          AA(4*I-1,7)=1.
1259          AA(4*I-1,8)=0.
1260          AA(4*I   ,5)=0.
```

```
1261          AA(4*I   ,6)=0.
1262          AA(4*I   ,7)=0.
1263          AA(4*I   ,8)=1.
1264        154 CONTINUE
1265      CC
1266      CC....CROUT REDUCTION
1267          IPP=4*IP
1268          DO 165 I=5,IPP,4
1269          DO 166 L=1,4
1270          DO 167 LL=1,4
1271          BB(L,LL)=0.
1272          DO 168 LLL=1,4
1273          IF (ABS(AA(I+L-1,LLL)) .LT. TMALL) AA(I+L-1,LLL)=0.
1274          IF (ABS(AA(I+LLL-5,8+LL)) .LT. TMALL) AA(I+LLL-5,8+LL)=0.
1275        168 BB(L,LL)=BB(L,LL) + AA(I+L-1,LLL)*AA(I+LLL-5,8+LL)
1276        167 CONTINUE
1277        166 CONTINUE
1278          DO 169 L=1,4
1279        169 AA(I-1+L,5)=AA(I-1+L,5)-BB(L,1)
1280          DO 170 L=1,3
1281        170 AA(I,5+L)=(AA(I,5+L)-BB(1,L+1))/AA(I,5)
1282          IF (I .EQ. (IPP-3)) GO TO 971
1283          DO 171 L=1,4
1284        171 AA(I,8+L)=AA(I,8+L)/AA(I,5)
1285        971 CONTINUE
1286          DO 172 L=1,3
1287        172 AA(I+L,6)=AA(I+L,6)-BB(L+1,2)-AA(I+L,5)*AA(I,6)
1288          DO 173 L=1,2
1289        173 AA(I+1,6+L)=(AA(I+1,6+L)-BB(2,2+L)-AA(I+1,5)*AA(I,6+L))/AA(I+1,6)
1290          IF (I .EQ. (IPP-3)) GO TO 191
1291          DO 174 L=1,4
1292          AA(I+L+3,2)=AA(I+L+3,2)-AA(I+L+3,1)*AA(I,6)
1293          AA(I+1,8+L)=(AA(I+1,8+L)-AA(I+1,5)*AA(I,8+L))/AA(I+1,6)
1294        174 CONTINUE
1295        191 CONTINUE
1296          DO 175 L=1,2
1297        175 AA(I+L+1,7)=AA(I+L+1,7)-BB(2+L,3)-AA(I+L+1,5)*AA(I,7)-
1298           1AA(I+L+1,6)*AA(I+1,7)
1299            AA(I+2,8)=(AA(I+2,8)-BB(3,4)-AA(I+2,5)*AA(I,8)-AA(I+2,6)*AA(I+1,8)
1300           2)/AA(I+2,7)
1301            IF (I .EQ. (IPP-3)) GO TO 190
1302            DO 176 L=1,4
1303            DO 177 LL=1,2
1304            AA(I+L+3,3)=AA(I+L+3,3)-AA(I+L+3,LL)*AA(I+LL-1,7)
1305            AA(I+2,8+L)=AA(I+2,8+L)-AA(I+2,4+LL)*AA(I+LL-1,8+L)
1306        177 CONTINUE
1307            AA(I+2,8+L)=AA(I+2,8+L)/AA(I+2,7)
1308        176 CONTINUE
1309        190 CONTINUE
1310            AA(I+3,8)=AA(I+3,8)-BB(4,4)-AA(I+3,5)*AA(I,8)-AA(I+3,6)*AA(I+1,8)
1311           1-AA(I+3,7)*AA(I+2,8)
1312            IF (I .EQ. (IPP-3)) GO TO 180
1313            DO 178 L=1,4
1314            DO 179 LL=1,3
1315            AA(I+L+3,4)= AA(I+L+3,4)-AA(I+L+3,LL)*AA(I+LL-1,8)
1316            AA(I+3,8+L)= AA(I+3,8+L)-AA(I+3,4+LL)*AA(I+LL-1,8+L)
1317        179 CONTINUE
1318            AA(I+3,8+L)= AA(I+3,8+L)/AA(I+3,8)
1319        178 CONTINUE
1320        180 CONTINUE
```

```
1321          DO 181 L=1,4
1322          DO 182 LL=1,4
1323          IF (ABS(AA(I+L-1,LL)).LT.TMALL) AA(I+L-1,LL)=0.
1324          IF (ABS(F(LL,(I+7)/4-1,J,K+2)) .LT. TMALL)
1325         1F(LL,(I+7)/4-1,J,K+2)=0.
1326       182 F(L,(I+7)/4,J,K+2)=F(L,(I+7)/4,J,K+2)-AA(I+L-1,LL)*F(LL,(I+7)/4-1
1327         1,J,K+2)
1328          LE=L-1
1329          IF (L .EQ. 1) GO TO 184
1330          DO 183 LL=1,LE
1331          F(L,(I+7)/4,J,K+2)=F(L,(I+7)/4,J,K+2)-AA(I+L-1,4+LL)*F(LL,(I+7)/4
1332         1,J,K+2)
1333       183 CONTINUE
1334       184 CONTINUE
1335          F(L,(I+7)/4,J,K+2)=F(L,(I+7)/4,J,K+2)/AA(I+L-1,5+L-1)
1336       181 CONTINUE
1337       165 CONTINUE
1338          W(4,IE,J,K+2)=F(4,IE,J,K+2)
1339          W(3,IE,J,K+2)=F(3,IE,J,K+2)-AA(IPP-1,8)*W(4,IE,J,K+2)
1340          W(2,IE,J,K+2)=F(2,IE,J,K+2)-AA(IPP-2,8)*W(4,IE,J,K+2)
1341         1-AA(IPP-2,7)*W(3,IE,J,K+2)
1342          W(1,IE,J,K+2)=F(1,IE,J,K+2)-AA(IPP-3,8)*W(4,IE,J,K+2)
1343         1-AA(IPP-3,7)*W(3,IE,J,K+2)-AA(IPP-3,6)*W(2,IE,J,K+2)
1344          DO 192 I=5,IPP,4
1345          II=IPP+5-I-4
1346          DO 193 L=1,4
1347          BB(1,L)=0.
1348          DO 194 LL=1,4
1349          IF (ABS(AA(II+1-L,8+LL)) .LT. TMALL) AA(II+1-L,8+LL)=0.
1350          IF (ABS(W(LL,(II+4)/4+1,J,K+2)) .LT. TMALL)
1351         1W(LL,(II+4)/4+1,J,K+2)=0.
1352       194 BB(1,L)=BB(1,L)+AA(II+1-L,8+LL)*W(LL,(II+4)/4+1,J,K+2)
1353       193 CONTINUE
1354          W(4,(II+4)/4,J,K+2)=F(4,(II+4)/4,J,K+2)-BB(1,1)
1355          W(3,(II+4)/4,J,K+2)=F(3,(II+4)/4,J,K+2)-BB(1,2)
1356         1-AA(II-1,8)*W(4,(II+4)/4,J,K+2)
1357          W(2,(II+4)/4,J,K+2)=F(2,(II+4)/4,J,K+2)-BB(1,3)
1358         1-AA(II-2,8)*W(4,(II+4)/4,J,K+2)-AA(II-2,7)*W(3,(II+4)/4,J,K+2)
1359          W(1,(II+4)/4,J,K+2)=F(1,(II+4)/4,J,K+2)-BB(1,4)
1360         1-AA(II-3,8)*W(4,(II+4)/4,J,K+2)-AA(II-3,7)*W(3,(II+4)/4,J,K+2)
1361         2-AA(II-3,6)*W(2,(II+4)/4,J,K+2)
1362       192 CONTINUE
1363       153 CONTINUE
1364          RETURN
1365          END
1366          SUBROUTINE ADI(K,M,DT,DX,DCA,CV,FK,COE,RB,UN,Q,SGO,
1367         1IS,IB,IE,ID,JS,JB,JE,JD,C,IP,JP)
1368          DIMENSION PSI(20,16,2),B1(20,16,2),B2(20,16,2),XI(20,16,2),
1369         1C1(20,16,2),C2(20,16,2),C3(20,16,2),T(20,16,2),
1370         2W(4,20,16,3),F(4,20,16,3),EI(20,16,2),B3(20,16,2),SR(20),
1371         4GA(20,16),GB(20,16),GC(20,16),GD(20,16),CN(20,16,2),
1372         5AA(90,12),BB(4,4),ANG(16),BATB(20)
1373          COMMON PSI,B1,B2,B3,XI,C1,C2,C3,T,W,F,SR,ANG,BATB
1374         1,GA,GB,GC,GD,CN,EI,AA,BB,AJCON
1375    CC
1376    CC---- USING ADI METHOD, SOLVE NEW TIME STEP VALUES PSI, XI, EI(I,J,2)
1377    CC
1378    CC....SOLVE PSI
1379          K=1
1380          DO 770 I=IS,ID
```

```
1381          DO 770 J=JS,JD
1382          F(2,I,J,3)=W(2,I,J,2)
1383          F(3,I,J,3)=W(3,I,J,2)
1384          F(4,I,J,3)=W(4,I,J,2)
1385          W(2,I,J,K+1)=W(2,I,J,K+1)-AJCON*C1(I,J,K)
1386          W(3,I,J,K+1)=W(3,I,J,K+1)-AJCON*C2(I,J,K)
1387          W(4,I,J,K+1)=W(4,I,J,K+1)-AJCON*C3(I,J,K)
1388          W(2,I,J,K)=W(2,I,J,K)-AJCON*C1(I,J,K)
1389          W(3,I,J,K)=W(3,I,J,K)-AJCON*C2(I,J,K)
1390          W(4,I,J,K)=W(4,I,J,K)-AJCON*C3(I,J,K)
1391      770 CONTINUE
1392          DO 772 J=1,JD
1393          W(2,ID,J,2)=-W(2,ID,J,2)-2.0*AJCON*C1(ID,J,1)
1394          W(2,ID,J,1)=W(2,ID,J,2)
1395      772 CONTINUE
1396          IF (MOD(M,2) .EQ. 1) GO TO 11
1397          GO TO 12
1398       11 CONTINUE
1399          DO 14 J=JB,JE
1400          DO 13 I=IB,IE
1401          GC(I,J)=COE*(1./Q+SR(I)*COS(ANG(J)))/(T(I,J,K+1)*((SR(I)*DCA)**2)*
1402         1(1./Q+SR(I)*COS(ANG(J)-DCA/2.)))+DT*W(3,I,J,K+1)/W(1,I,J,K+1)
1403         2/(2.*SR(I)*DCA)
1404          GA(I,J)=COE*(1./Q+SR(I)*COS(ANG(J)))/(T(I,J,K+1)*((SR(I)*DCA)**2)*
1405         1(1./Q+SR(I)*COS(ANG(J)+DCA/2.)))-DT*W(3,I,J,K+1)/W(1,I,J,K+1)
1406         2/(2.*SR(I)*DCA)
1407          GB(I,J)=1.+COE*(1./Q+SR(I)*COS(ANG(J)))/(T(I,J,K+1)*SR(I)*SR(I)
1408         1*DCA*DCA)*(1./(1./Q+SR(I)*COS(ANG(J)+DCA/2.))+1./(1./Q+SR(I)*
1409         2COS(ANG(J)-DCA/2.)))
1410          GD(I,J)=PSI(I,J,K)+COE*(1./Q+SR(I)*COS(ANG(J)))/(T(I,J,K)*SR(I)*
1411         1DX*DX)*((SR(I+1)+SR(I))/2.*(PSI(I+1,J,K)-PSI(I,J,K))/(1./Q+
1412         2(SR(I+1)+SR(I))/2.*COS(ANG(J)))-(SR(I-1)+SR(I))/2.*(PSI(I,J,K)-
1413         3PSI(I-1,J,K))/(1./Q+(SR(I-1)+SR(I))/2.*COS(ANG(J))))
1414         4-DT*W(2,I,J,K)/W(1,I,J,K)*(PSI(I+1,J,K)-PSI(I-1,J,K))/(2.*DX)
1415       13 CONTINUE
1416       14 CONTINUE
1417   CC     USE CROUT REDUCTION
1418          CALL        CROUT(M,K,IB,IE,JB,JE,IP,JP,GA,GB,GC,GD,PSI,JD,ID)
1419          GO TO 17
1420       12 CONTINUE
1421          DO 19 J=JB,JE
1422          DO 18 I=IB,IE
1423          GC(I,J)=COE*(1./Q+SR(I)*COS(ANG(J)))*(SR(I-1)+SR(I))/2.
1424         1/(T(I,J,K+1)*SR(I)*DX*DX*(1./Q+(SR(I-1)+SR(I))/2.*COS(ANG(J))))
1425         2+DT*W(2,I,J,K+1)/W(1,I,J,K+1)/(2.*DX)
1426          GA(I,J)=COE*(1./Q+SR(I)*COS(ANG(J)))*(SR(I+1)+SR(I))/2.
1427         1/(T(I,J,K+1)*SR(I)*DX*DX*(1./Q+(SR(I+1)+SR(I))/2.*COS(ANG(J))))
1428         2-DT*W(2,I,J,K+1)/W(1,I,J,K+1)/(2.*DX)
1429          GB(I,J)=1.+COE*(1./Q+SR(I)*COS(ANG(J)))/(T(I,J,K+1)*SR(I)*DX*DX)
1430         1*((SR(I+1)+SR(I))/2./(1./Q+(SR(I+1)+SR(I))/2.*COS(ANG(J)))
1431         2+(SR(I-1)+SR(I))/2./(1./Q+(SR(I-1)+SR(I))/2.*COS(ANG(J))))
1432          GD(I,J)=PSI(I,J,K)+COE*(1./Q+SR(I)*COS(ANG(J)))/(T(I,J,K)*SR(I)*
1433         1SR(I)*DCA*DCA)*((PSI(I,J+1,K)-PSI(I,J,K))/(1./Q+SR(I)*COS(ANG(J)+
1434         2DCA/2.))-(PSI(I,J,K)-PSI(I,J-1,K))/(1./Q+SR(I)*COS(ANG(J)-DCA/2.))
1435         3)-DT*W(3,I,J,K)/W(1,I,J,K)/(SR(I)*2.*DCA)*(PSI(I,J+1,K)-
1436         4PSI(I,J-1,K))
1437       18 CONTINUE
1438       19 CONTINUE
1439          CALL        CROUT(M,K,IB,IE,JB,JE,IP,JP,GA,GB,GC,GD,PSI,JD,ID)
1440       17 CONTINUE
```

```
      DO 25 I=IS,ID
      PSI(I,JE+1,K+1)=PSI(I,JE-1,K+1)
      PSI(I,JB-1,K+1)=PSI(I,JB+1,K+1)
   25 CONTINUE
      DO 27 J=JB,JE
      DO 26 I=IB,IE
      C3(I,J,K+1)=-(((SR(I+1)+SR(I))/2.*(PSI(I+1,J,K+1)
     1-PSI(I,J,K+1))/(1./Q+(SR(I+1)+SR(I))/2.*COS(ANG(J)))-(SR(I-1)
     2+SR(I))/2.*(PSI(I,J,K+1)-PSI(I-1,J,K+1))/(1./Q+(SR(I-1)+SR(I))/2.
     3*COS(ANG(J))))/(SR(I)*DX*DX)+ ((PSI(I,J+1,K+1)-PSI(I,J,K+1))
     4/(1./Q+SR(I)*COS(ANG(J) + DCA/2.     ))-(PSI(I,J,K+1)-
     5PSI(I,J-1,K+1))/(1./Q+SR(I)*COS(ANG(J) - DCA/2.     )))
     6/((SR(I)*DCA)**2))
   26 CONTINUE
   27 CONTINUE
      DO 32 J=JB,JE
      DO 31 I=IB,IE
      B1(I,J,K+1)=-(PSI(I,J+1,K+1)-PSI(I,J-1,K+1))/(SR(I)*2.*DCA*
     1(1./Q+SR(I)*COS(ANG(J))))
      B2(I,J,K+1)= (PSI(I+1,J,K+1)-PSI(I-1,J,K+1))/(2.*DX*
     1(1./Q+SR(I)*COS(ANG(J))))
   31 CONTINUE
   32 CONTINUE
CC
CC....SOLVE XI
      IF (MOD(M,2) .EQ. 1) GO TO 311
      GO TO 312
  311 CONTINUE
      DO 16 J=JB,JE
      DO 15 I=IB,IE
      GC(I,J)=(COE/(SR(I)*SR(I)*DCA*DCA*(T(I,J-1,K+1)+T(I,J,K+1))/2.*(
     11./Q+SR(I)*COS(ANG(J) - DCA/2.     )))+DT*W(3,I,J-1,K+1)/
     2W(1,I,J-1,K+1)/(2.*SR(I)*DCA*(1./Q+SR(I)*COS(ANG(J-1)))))
     3*(1./Q+SR(I)*COS(ANG(J)))
      GA(I,J)=(COE/(SR(I)*SR(I)*DCA*DCA*(T(I,J+1,K+1)+T(I,J,K+1))/2.*(
     11./Q+SR(I)*COS(ANG(J) + DCA/2.     )))-DT*W(3,I,J+1,K+1)/
     2W(1,I,J+1,K+1)/(2.*SR(I)*DCA*(1./Q+SR(I)*COS(ANG(J+1)))))
     3*(1./Q+SR(I)*COS(ANG(J)))
      GB(I,J)=1.+COE*(1./Q+SR(I)*COS(ANG(J)))/((SR(I)*DCA)**2)*
     1(2./((T(I,J+1,K+1)+T(I,J,K+1))*(1./Q+SR(I)*COS(ANG(J) + DCA/2.)))
     2+2./((T(I,J-1,K+1)+T(I,J,K+1))*(1./Q+SR(I)*COS(ANG(J) - DCA/2.))))
      GD(I,J)=XI(I,J,K)+(COE/(SR(I)*DX*DX)*((SR(I+1)+SR(I))/2.*
     1(XI(I+1,J,K)-XI(I,J,K))/((T(I+1,J,K)+T(I,J,K))/2.*(1./Q+(SR(I+1)
     2+SR(I))/2.*COS(ANG(J)))) -(SR(I-1)+SR(I))/2.*(XI(I,J,K)-
     3XI(I-1,J,K))/((T(I-1,J,K)+T(I,J,K))/2.*(1./Q+(SR(I-1)+SR(I))/2.
     4*COS(ANG(J)))) -DT*(SR(I+1)*W(2,I+1,J,K)/W(1,I+1,J,K)*
     5XI(I+1,J,K)/(1./Q+SR(I+1)*COS(ANG(J)))-SR(I-1)*W(2,I-1,J,K)/
     6W(1,I-1,J,K)*XI(I-1,J,K)/(1./Q+SR(I-1)*COS(ANG(J))))/(2.*SR(I)
     7*DX))*(1./Q+SR(I)*COS(ANG(J))) +
     7((SR(I+1)*B1(I+1,J,K)*W(4,I+1,J,K)/W(1,I+1,J,K)
     8 -SR(I-1)*B1(I-1,J,K)*W(4,I-1,J,K)/W(1,I-1,J,K))/(2.*SR(I)*DX)
     9+(B2(I,J+1,K+1)*W(4,I,J+1,K+1)/W(1,I,J+1,K+1)
     1 -B2(I,J-1,K+1)*W(4,I,J-1,K+1)/W(1,I,J-1,K+1))/(2.*SR(I)*DCA))
     2*DT*(1./Q+SR(I)*COS(ANG(J)))
   15 CONTINUE
   16 CONTINUE
      CALL       CROUT(M,K,IB,IE,JB,JE,IP,JP,GA,GB,GC,GD, XI,JD,ID)
      GO TO 317
  312 CONTINUE
      DO 22 J=JB,JE
```

```
      DO 21 I=IB,IE
      GC(I,J)=(COE*(SR(I-1)+SR(I))/2./(SR(I)*DX*DX*(T(I-1,J,K+1)+
     1T(I,J,K+1))/2.*(1./Q+(SR(I-1)+SR(I))/2.*COS(ANG(J)))) +DT*SR(I-1)
     2*W(2,I-1,J,K+1)/W(1,I-1,J,K+1)/(2.*SR(I)*DX*(1./Q+SR(I-1)
     3*COS(ANG(J)))))*(1./Q+SR(I)*COS(ANG(J)))
      GA(I,J)=(COE*(SR(I+1)+SR(I))/2./(SR(I)*DX*DX*(T(I+1,J,K+1)+
     1T(I,J,K+1))/2.*(1./Q+(SR(I+1)+SR(I))/2.*COS(ANG(J)))) -DT*SR(I+1)
     2*W(2,I+1,J,K+1)/W(1,I+1,J,K+1)/(2.*SR(I)*DX*(1./Q+SR(I+1)
     3*COS(ANG(J)))))*(1./Q+SR(I)*COS(ANG(J)))
      GB(I,J)=1.+COE/(SR(I)*DX*DX)*((SR(I+1)+SR(I))/2./((T(I+1,J,K+1)
     1+T(I,J,K+1))/2.*(1./Q+(SR(I+1)+SR(I))/2.*COS(ANG(J))))+(SR(I-1)+
     2SR(I))/2./((T(I-1,J,K+1)+T(I,J,K+1))/2.*(1./Q+(SR(I-1)+SR(I))/2.*
     3COS(ANG(J)))))*(1./Q+SR(I)*COS(ANG(J)))
      GD(I,J)=XI(I,J,K)+(COE/((SR(I)*DCA)**2)*((XI(I,J+1,K)-XI(I,J,K))/
     1((T(I,J+1,K)+T(I,J,K))/2.*(1./Q+SR(I)*COS(ANG(J) + DCA/2.      )))
     2-(XI(I,J,K)-XI(I,J-1,K))/((T(I,J-1,K)+T(I,J,K))/2.*(1./Q+SR(I)*
     3COS(ANG(J) - DCA/2.      )))) -DT/(2.*SR(I)*DCA)*(W(3,I,J+1,K)
     4/W(1,I,J+1,K)*XI(I,J+1,K)/(1./Q+SR(I)*COS(ANG(J+1)))-
     5W(3,I,J-1,K)/W(1,I,J-1,K)*XI(I,J-1,K)/(1./Q+SR(I)*COS(ANG(J-1))))
     6)*(1./Q+SR(I)*COS(ANG(J))) +
     7((SR(I+1)*B1(I+1,J,K+1)*W(4,I+1,J,K+1)/W(1,I+1,J,K+1)
     8 -SR(I-1)*B1(I-1,J,K+1)*W(4,I-1,J,K+1)/W(1,I-1,J,K+1))/(2.*SR(I)
     9*DX)+(B2(I,J+1,K)*W(4,I,J+1,K)/W(1,I,J+1,K)
     1 -B2(I,J-1,K)*W(4,I,J-1,K)/W(1,I,J-1,K))/(2.*SR(I)*DCA))
     2*DT*(1./Q+SR(I)*COS(ANG(J)))
   21 CONTINUE
   22 CONTINUE
      CALL       CROUT(M,K,IB,IE,JB,JE,IP,JP,GA,GB,GC,GD, XI,JD,ID)
  317 CONTINUE
      DO 325 I=IS,ID
       XI(I,JE+1,K+1)= XI(I,JE-1,K+1)
       XI(I,JB-1,K+1)= XI(I,JB+1,K+1)
  325 CONTINUE
      DO 332 J=JB,JE
      DO 331 I=IB,IE
      B3(I,J,K+1)=(          XI(I,J,K+1))/(1./Q+SR(I)*COS(ANG(J)))
      C1(I,J,K+1)=-(XI(I,J+1,K+1)-XI(I,J-1,K+1))/(
     1(1./Q+SR(I)*COS(ANG(J)))*SR(I)*2.*DCA)
      C2(I,J,K+1)= (XI(I+1,J,K+1)-XI(I-1,J,K+1))/(
     1(1./Q+SR(I)*COS(ANG(J)))*2.*DX)
  331 CONTINUE
  332 CONTINUE
      DO 771 I=IS,ID
      DO 771 J=JS,JD
      W(2,I,J,K+1)=F(2,I,J,3)
      W(3,I,J,K+1)=F(3,I,J,3)
      W(4,I,J,K+1)=F(4,I,J,3)
      W(2,I,J,K)=F(2,I,J,3)
      W(3,I,J,K)=F(3,I,J,3)
      W(4,I,J,K)=F(4,I,J,3)
  771 CONTINUE
CC
CC....SOLVE TEMPERATURE EI
      IF (MOD(M,2) .EQ. 1) GO TO 211
      GO TO 212
  211 CONTINUE
      DO 214 J=JB,JE
      DO 213 I=IB,IE
      GC(I,J)=DT*(1./Q+SR(I)*COS(ANG(J)-DCA/2.))*(CN(I,J,K+1)+
     1CN(I,J-1,K+1))/(2.*W(1,I,J,K+1)     *(1./Q+SR(I)*
```

```
     2COS(ANG(J)))*SR(I)*SR(I)*DCA*DCA) +DT*W(3,I,J,K+1)/
     3W(1,I,J,K+1)/(2.*SR(I)*DCA)
      GA(I,J)=DT*(1./Q+SR(I)*COS(ANG(J)+DCA/2.))*(CN(I,J,K+1)+
     1CN(I,J+1,K+1))/(2.*W(1,I,J,K+1)      *(1./Q+SR(I)*
     2COS(ANG(J)))*SR(I)*SR(I)*DCA*DCA) -DT*W(3,I,J,K+1)/
     3W(1,I,J,K+1)/(2.*SR(I)*DCA)
      GB(I,J)=1.+DT/(W(1,I,J,K+1)    )*(((1./Q+SR(I)*
     1COS(ANG(J)+DCA/2.))*(CN(I,J,K+1)+CN(I,J+1,K+1))/2.+(1./Q+SR(I)*
     2COS(ANG(J)-DCA/2.))*(CN(I,J,K+1)+CN(I,J-1,K+1))/2.)/( (1./Q+SR(I)*
     3COS(ANG(J)))*SR(I)*SR(I)*DCA*DCA)) +DT*(FK-1.)/2.*
     4(((1./Q+SR(I+1)*COS(ANG(J)))*SR(I+1)*W(2,I+1,J,K+1)/
     5W(1,I+1,J,K+1)-(1./Q+SR(I-1)*COS(ANG(J)))*SR(I-1)*W(2,I-1,J,
     6K+1)/W(1,I-1,J,K+1))/((1./Q+SR(I)*COS(ANG(J)))*SR(I)*2.*DX) +
     7((1./Q+SR(I)*COS(ANG(J+1)))*W(3,I,J+1,K+1)/W(1,I,J+1,K+1)-
     8(1./Q+SR(I)*COS(ANG(J-1)))*W(3,I,J-1,K+1)/W(1,I,J-1,K+1))/
     9((1./Q+SR(I)*COS(ANG(J)))*SR(I)*2.*DCA))
      PASS=
     6+0.5/4.*0.5*DT/DX*(ABS(W(2,I+1,J,K)/W(1,I+1,J,K)-W(2,I,J,K)
     7/W(1,I,J,K))*( EI(I+1,J,K)- EI(I,J,K))-ABS(W(2,I,J,K)/W(1,I,J,K)
     8-W(2,I-1,J,K)/W(1,I-1,J,K))*( EI(I,J,K)- EI(I-1,J,K)))
     6+0.5/4.*BATB(I)*(ABS(W(3,I,J+1,K)/W(1,I,J+1,K)-W(3,I,J,K)
     7/W(1,I,J,K))*( EI(I,J+1,K)- EI(I,J,K))-ABS(W(3,I,J,K)/W(1,I,J,K)
     8-W(3,I,J-1,K)/W(1,I,J-1,K))*( EI(I,J,K)- EI(I,J-1,K)))
      GD(I,J)=EI(I,J,K)     +DT/(W(1,I,J,K))*
     1((1./Q+(SR(I+1)+SR(I))/2.*COS(ANG(J)))*0.5*(SR(I)+SR(I+1))*0.5*
     2(CN(I,J,K)+CN(I+1,J,K))*(EI(I+1,J,K)-EI(I,J,K))-
     3(1./Q+(SR(I-1)+SR(I))/2.*COS(ANG(J)))*0.5*(SR(I)+SR(I-1))*0.5*
     4(CN(I,J,K)+CN(I-1,J,K))*(EI(I,J,K)-EI(I-1,J,K)))/((1./Q+
     5SR(I)*COS(ANG(J)))*SR(I)*DX*DX)-DT*W(2,I,J,K)/W(1,I,J,K)
     6*(EI(I+1,J,K)-EI(I-1,J,K))/(2.*DX)-0.5*DT*(FK-1.)*EI(I,J,K)*
     4(((1./Q+SR(I+1)*COS(ANG(J)))*SR(I+1)*W(2,I+1,J,K)/W(1,I+1,J,K)
     5 -(1./Q+SR(I-1)*COS(ANG(J)))*SR(I-1)*W(2,I-1,J,K)/W(1,I-1,J,K)
     6)/((1./Q+SR(I)*COS(ANG(J)))*SR(I)*2.*DX) +((1./Q+SR(I)*
     7COS(ANG(J+1)))*W(3,I,J+1,K)/W(1,I,J+1,K)-(1./Q+SR(I)*
     8COS(ANG(J-1)))*W(3,I,J-1,K)/W(1,I,J-1,K))/((1./Q+
     9SR(I)*COS(ANG(J)))*SR(I)*2.*DCA))
     8+COE*(C1(I,J,K+1)**2+C2(I,J,K+1)**2+C3(I,J,K+1)**2)/
     9(T(I,J,K+1)*W(1,I,J,K+1)) +PASS
  213 CONTINUE
  214 CONTINUE
      CALL       CROUT(M,K,IB,IE,JB,JE,IP,JP,GA,GB,GC,GD, EI,JD,ID)
      GO TO 217
  212 CONTINUE
      DO 235 J=JB,JE
      DO 234 I=IB,IE
      GC(I,J)=DT*(1./Q+(SR(I)+SR(I-1))/2.*COS(ANG(J)))*0.5*(SR(I)+
     1SR(I-1))*0.5*(CN(I,J,K+1)+CN(I-1,J,K+1))/(W(1,I,J,K+1) *
     2(1./Q+SR(I)*COS(ANG(J)))*SR(I)*DX*DX) +DT*W(2,I,J,K+1)/
     3W(1,I,J,K+1)/(2.*DX)
      GA(I,J)=DT*(1./Q+(SR(I)+SR(I+1))/2.*COS(ANG(J)))*0.5*(SR(I)+
     1SR(I+1))*0.5*(CN(I,J,K+1)+CN(I+1,J,K+1))/(W(1,I,J,K+1) *
     2(1./Q+SR(I)*COS(ANG(J)))*SR(I)*DX*DX) -DT*W(2,I,J,K+1)/
     3W(1,I,J,K+1)/(2.*DX)
      GB(I,J)=DT/(W(1,I,J,K+1)    )*(((1./Q+(SR(I)+SR(I+1))/2.*
     1COS(ANG(J)))*0.5*(SR(I)+SR(I+1))*0.5*(CN(I,J,K+1)+CN(I+1,J,K+1))
     2+(1./Q+(SR(I)+SR(I-1))/2.*COS(ANG(J)))*0.5*(SR(I)+SR(I-1))*
     30.5*(CN(I,J,K+1)+CN(I-1,J,K+1)))/((1./Q+SR(I)*COS(ANG(J)))*SR(I)
     1*DX*DX)) +1. + DT*(FK-1.)/2. *
     4(((1./Q+SR(I+1)*COS(ANG(J)))*SR(I+1)*W(2,I+1,J,K+1)/
     5W(1,I+1,J,K+1)-(1./Q+SR(I-1)*COS(ANG(J)))*SR(I-1)*W(2,I-1,J,
```

```
      6K+1)/W(1,I-1,J,K+1))/((1./Q+SR(I)*COS(ANG(J)))*SR(I)*2.*DX) +
      7((1./Q+SR(I)*COS(ANG(J+1)))*W(3,I,J+1,K+1)/W(1,I,J+1,K+1)-
      8(1./Q+SR(I)*COS(ANG(J-1)))*W(3,I,J-1,K+1)/W(1,I,J-1,K+1))/
      9((1./Q+SR(I)*COS(ANG(J)))*SR(I)*2.*DCA))
       PASS=
      6+0.5/4.*0.5*DT/DX*(ABS(W(2,I+1,J,K)/W(1,I+1,J,K)-W(2,I,J,K)
      7/W(1,I,J,K))*( EI(I+1,J,K)- EI(I,J,K))-ABS(W(2,I,J,K)/W(1,I,J,K)
      8-W(2,I-1,J,K)/W(1,I-1,J,K))*( EI(I,J,K)- EI(I-1,J,K)))
      6+0.5/4.*BATB(I)*(ABS(W(3,I,J+1,K)/W(1,I,J+1,K)-W(3,I,J,K)
      7/W(1,I,J,K))*( EI(I,J+1,K)- EI(I,J,K))-ABS(W(3,I,J,K)/W(1,I,J,K)
      8-W(3,I,J-1,K)/W(1,I,J-1,K))*( EI(I,J,K)- EI(I,J-1,K)))
       GD(I,J)=EI(I,J,K)    +DT/(W(1,I,J,K))*(((1./Q+SR(I)*
      1COS(ANG(J)+DCA/2.))*0.5*(CN(I,J,K)+CN(I,J+1,K))*(EI(I,J+1,K)-
      2EI(I,J,K))-(1./Q+SR(I)*COS(ANG(J)-DCA/2.))*0.5*(CN(I,J,K)+
      3CN(I,J-1,K))*(EI(I,J,K)-EI(I,J-1,K)))/((1./Q+SR(I)*COS(ANG(J)))*
      4SR(I)*SR(I)*DCA*DCA))-DT*W(3,I,J,K)/W(1,I,J,K)*(EI(I,J+1,K)-
      5EI(I,J-1,K))/(2.*SR(I)*DCA)-DT*(FK-1.)*EI(I,J,K)*0.5*
      4(((1./Q+SR(I+1)*COS(ANG(J)))*SR(I+1)*W(2,I+1,J,K)/W(1,I+1,J,K)
      5 -(1./Q+SR(I-1)*COS(ANG(J)))*SR(I-1)*W(2,I-1,J,K)/W(1,I-1,J,K)
      6)/((1./Q+SR(I)*COS(ANG(J)))*SR(I)*2.*DX) +((1./Q+SR(I)*
      7COS(ANG(J+1)))*W(3,I,J+1,K)/W(1,I,J+1,K)-(1./Q+SR(I)*
      8COS(ANG(J-1)))*W(3,I,J-1,K)/W(1,I,J-1,K))/((1./Q+
      9SR(I)*COS(ANG(J)))*SR(I)*2.*DCA))
      8+COE*(C1(I,J,K+1)**2+C2(I,J,K+1)**2+C3(I,J,K+1)**2)/
      9(T(I,J,K+1)*W(1,I,J,K+1)) +PASS
  234 CONTINUE
  235 CONTINUE
      CALL       CROUT(M,K,IB,IE,JB,JE,IP,JP,GA,GB,GC,GD, EI,JD,ID)
  217 CONTINUE
      DO 225 I=IS,ID
      EI(I,JE+1,K+1)= EI(I,JE-1,K+1)
      EI(I,JB-1,K+1)= EI(I,JB+1,K+1)
  225 CONTINUE
      RETURN
      END
      SUBROUTINE CROUT(M,K,IB,IE,JB,JE,IP,JP,GA,GB,GC,GD,PSI,JD,ID)
CC
CC----CROUT REDUCTION METHOD ----------
      DIMENSION AA(90, 3),E(90),X(90),GA(20,16),GB(20,16),GC(20,16),
     1GD(20,16),PSI(20,16,2)
      SMALL=1.0E-70
      IF (MOD(M,2) .EQ. 1) GO TO 3
      GO TO 2
    3 CONTINUE
      JS=1
      DO 123 I=IB,IE
      DO 122 J=JS,JP
      AA(J,2)=GB(I,J+1)
      IF (J .EQ. JP) GO TO 124
      IF (J .EQ. JS) GO TO 125
      AA(J,3  )=-GA(I,J+1)
      GO TO 125
  124 AA(JP,1   )=-(GC(I,JP+1)+GA(I,JP+1))
  125 CONTINUE
      IF (J .EQ. JS) GO TO 126
      IF (J .EQ. JP) GO TO 127
      AA(J,1  )=-GC(I,J+1)
      GO TO 127
  126 AA(JS,3   )=-(GA(I,JS+1)+GC(I,JS+1))
  127 CONTINUE
```

```
1681          E(J)=GD(I,J+1)
1682        122 CONTINUE
1683          AA(JS,3   )=AA(JS,3   )/AA(JS,2 )
1684          E(JS)=E(JS)/AA(JS,2 )
1685          DO 130 J=JB,JP
1686          IF (ABS(AA(J,  1)) .LE. SMALL) AA(J,  1)=0.
1687          IF (ABS(AA(J-1,3)) .LE. SMALL ) AA(J-1,3)=0.
1688          AA(J,2)=AA(J,2)-AA(J,1  )*AA(J-1,3)
1689          IF (ABS(E(J-1)) .LE. SMALL) E(J-1)=0.
1690          E(J)=(E(J)-AA(J,  1)*E(J-1))/AA(J,2)
1691          IF (J .EQ. JP) GO TO 131
1692          AA(J,3  )=AA(J,3  )/AA(J,2)
1693        131 CONTINUE
1694        130 CONTINUE
1695          X(JP)=E(JP)
1696          JQ=JP-1
1697          DO 133 J=JS,JQ
1698          K=JQ+JS-J
1699          IF (ABS(AA(K,3  )) .LE. SMALL) AA(K,3  )=0.
1700          X(K)=E(K)-AA(K,3  )*X(K+1)
1701        133 CONTINUE
1702          DO 128 J=JS,JP
1703          PSI(I,J+1,2)=X(J)
1704          IF (ABS(PSI(I,J+1,2)) .LT. SMALL) PSI(I,J+1,2)=0.
1705        128 CONTINUE
1706        123 CONTINUE
1707          GO TO 4
1708          2 CONTINUE
1709          IS=1
1710          DO 23 J=JB,JE
1711          DO 22 I=IS,IP
1712          E(I)=GD(I+1,J)
1713          AA(I,2)=GB(I+1,J)
1714          IF (I .EQ. IP) GO TO 24
1715          AA(I,3  )=-GA(I+1,J)
1716          GO TO 25
1717         24 E(IP)=GD(IP+1,J)+GA(IP+1,J)*PSI(IP+2,J,2)
1718         25 CONTINUE
1719          IF (I .EQ. IS) GO TO 26
1720          AA(I,  1)=-GC(I+1,J)
1721          GO TO 27
1722         26 CONTINUE
1723          E(IS)=GD(IS+1,J)+GC(IS+1,J)*PSI(IS,J,2)
1724         27 CONTINUE
1725         22 CONTINUE
1726          AA(IS,3   )=AA(IS,3   )/AA(IS,2 )
1727          E(IS)=E(IS)/AA(IS,2 )
1728          DO 30 I=IB,IP
1729          IF (ABS(AA(I,  1)) .LE. SMALL) AA(I,  1)=0.
1730          IF (ABS(AA(I-1,3)) .LE. SMALL) AA(I-1,3)=0.
1731          AA(I,2)=AA(I,2)-AA(I,  1)*AA(I-1,3)
1732          IF (ABS(E(I-1)) .LE. SMALL) E(I-1)=0.
1733          E(I)=(E(I)-AA(I,  1)*E(I-1))/AA(I,2)
1734          IF (I .EQ. IP) GO TO 30
1735          AA(I,3  )=AA(I,3  )/AA(I,2)
1736         30 CONTINUE
1737          X(IP)=E(IP)
1738          IQ=IP-1
1739          DO 33 I=IS,IQ
1740          K=IQ+IS-I
```

```
      IF (ABS(AA(K,3  )) .LE. SMALL) AA(K,3  )=0.
      X(K)=E(K)-AA(K,3  )*X(K+1)
   33 CONTINUE
      DO 28 I=IS,IP
      PSI(I+1,J,2)=X(I)
      IF (ABS(PSI(I+1,J,2)) .LT. SMALL) PSI(I+1,J,2)=0.
   28 CONTINUE
   23 CONTINUE
    4 CONTINUE
      K=1
      RETURN
      END
      SUBROUTINE AVERA(SEQ,AVV)
CC
CC....AVERAGING IN THETA DIRECTION
      DIMENSION SEQ(16)
      COMMON/XY/NUG,DX,JE,JB,PI        ,IE,THJ
      AVV=0.0
      JBB=JB+1
      JEE=JE-1
      DO 1 J=JBB ,JEE
      AVV=AVV+SEQ(J)
    1 CONTINUE
      AVV=2.0*AVV+SEQ(JB)+SEQ(JE)
      AVV=2.0*  AVV/(NUG*DX)
      RETURN
      END
      SUBROUTINE SURIN(A,B,RB,RSMA)
CC
CC....SURFACE INTEGRATION (ON THE WALL)
      DIMENSION A(16),THJ(16)
      COMMON /XY/NUG,DX,JE,JB,PI,IE,THJ
      A(JE)=A(JE)/2.
      A(JB)=A(JB)/2.
      B=0.0
      DO 1 J=JB,JE
      WUG=2.*PI*RSMA*(IE-0.5)/IE /NUG
      B=B+A(J)*2.*PI*(RB+RSMA*(IE-0.5)/IE*COS(THJ(J)))*WUG
    1 CONTINUE
      B=2.*B/2.0/PI/RB*100.0
      RETURN
      END
      SUBROUTINE VOLIN(A,B,RB,RSMA)
CC
CC....VOLUME INTEGRATION
      DIMENSION A(20,16),THJ(16)
      COMMON /XY/NUG,DX,JE,JB,PI,IE,THJ
      B=0.0
      IDD=IE
      DO 1 I=1,IDD
      ARA=PI*RSMA*RSMA*DX*DX*((I-0.5)**2-(I-1.5)**2)/NUG
      IF(I.EQ.1)ARA=PI*RSMA*RSMA*DX*DX*(I-0.5)**2/NUG
      A(I,JE)=A(I,JE)/2.
      A(I,JB)=A(I,JB)/2.
      DO 1 J=JB,JE
      B=B+A(I,J)*2.*PI*(RB+RSMA*DX*(I-1)*COS(THJ(J)))*ARA
    1 CONTINUE
      B=2.*B/2.0/PI/RB*100.0
      RETURN
      END
```

```
      SUBROUTINE ARAIN(A,B,RB,RSMA)
CC
CC....AREA INTEGRATION (ON POLOIDAL PLANE)
      DIMENSION A(20,16),THJ(16)
      COMMON /XY/NUG,DX,JE,JB,PI,IE,THJ
      B=0.0
      IDD=IE
      DO 1 I=1,IDD
      ARA=PI*RSMA*RSMA*DX*DX*((I-0.5)**2-(I-1.5)**2)/NUG
      IF(I.EQ.1)ARA=PI*RSMA*RSMA*DX*DX*(I-0.5)**2/NUG
      A(I,JE)=A(I,JE)/2.
      A(I,JB)=A(I,JB)/2.
      DO 1 J=JB,JE
      B=B+A(I,J)*ARA
    1 CONTINUE
      DO 2 I=1,IDD
      A(I,JE)=A(I,JE)*2.
      A(I,JB)=A(I,JB)*2.
    2 CONTINUE
      B=2.0*B
      RETURN
      END
```